

Carnegie Mellon University
MELLON COLLEGE OF SCIENCE

THESIS

SUBMITTED IN PARTIAL FULFILLMENT OF THE REQUIREMENTS
FOR THE DEGREE OF

DOCTOR OF PHILOSOPHY IN THE FIELD OF PHYSICS

TITLE: "Elasticity of lipid membrane leaflets: determining pivotal plane and tilt modulus in computer simulations"

PRESENTED BY: Xin Wang

ACCEPTED BY THE DEPARTMENT OF PHYSICS

MARKUS DESERNO	5/24/17
MARKUS DESERNO, CHAIR PROFESSOR	DATE

STEPHEN GAROFF	5/24/17
STEPHEN GAROFF, DEPT HEAD	DATE

APPROVED BY THE COLLEGE COUNCIL

REBECCA DOERGE	5/24/17
REBECCA DOERGE, DEAN	DATE

Elasticity of lipid membrane leaflets

Determining pivotal plane and tilt modulus in computer simulations

Xin Wang

Advised by: Prof. Markus Deserno

*Submitted in partial fulfillment of the requirements
for the degree of Doctor of Philosophy*



Physics Department
Carnegie Mellon University
May, 2017

Dedicated to the Memory of My Beloved Grandma

Abstract

This thesis introduces a novel protocol to measure two elastic quantities of lipid membranes, the pivotal plane of a single leaflet and the lipid tilt modulus. The key setup relies on the simulation of a buckled membrane, a configuration that had been previously proposed to measure a membrane's bending rigidity. Since this method solely depends on the geometrical analysis of the membrane shape, and can hence even be applied to existing simulation trajectories of buckled membranes, it can provide two additional physical quantities at no extra simulation cost. Due to the high precision of its result, many technical subtleties are considered throughout the derivation, pertaining for instance to higher order corrections due to Poisson ratio effects. This calculation, as shown in this thesis, can be used to provide both a reference for other study as well as deeper insight into the nature of lipid models, especially the limitation of the coarse-grained ones.

After introducing the subject in the first chapter, the second chapter is mainly intended as a concise review of some key technical details for readers not familiar with the basic concepts in membrane and lipid structure, membrane elasticity theory and molecular dynamics simulations of membranes.

Once the reader is prepared with the basic background knowledge, the third chapter dives into the first major topic of determining the pivotal plane position. This is a foundational step in the construction of well-known energy functionals for membranes (such as the Helfrich Hamiltonian), which describe the membrane as a continuous surface with no thickness. Among all the possible choices of a dividing surface, the pivotal plane, which is the location where the area strain vanishes, is one of the most common ones. We provide two measurement methods, both of which are based on monitoring the number imbalance across two opposing lipid layers. The first method is based on simple geometric configurations: cylinders and spheres. However, the process of lipid number equilibration needs a high flip-flop rate of the lipids between the two layers, which is difficult to achieve in simulation for many lipid models. The second method relies on a buckled membrane. This solves the equilibration problem, but requires more sophisticated lipid counting. The generic Cooke three bead model is amenable for both methods, and so it can serve as an excellent test case for the more complicated buckling approach. Agreement between the two methods hence shows that the latter one is indeed reliable. Following this proof of principle, two membrane models of higher resolution, MARTINI DMPC and Berger DMPC are investigated, and the positions of their pivotal planes are determined. The value obtained for MARTINI, $z_0 = 0.850(11)\text{nm}$ lies about 0.4 nm below the glycerol backbone, which is unexpectedly small. In contrast, the united atom Berger model's value, $z_0 = 1.3225(44)\text{nm}$,

is much closer to the glycerol backbone, where most people believe the pivotal plane is. We attribute this discrepancy to a limitation of the coarse graining description, which makes the tail part of MARTINI DMPC less responsive to curvature changes.

The last chapter illustrates that an extension of the analysis process for the buckle, with which the pivotal plane was determined, can be used to measure the tilt modulus, which describes the energetic cost for tilting a lipid's orientation away from the local normal vector. The same three lipid models are investigated. For the Cooke model, a bilayer tilt modulus of 29 ± 9 pN/nm is found, while for MARTINI DMPC, 115 ± 6 pN/nm and for Berger DMPC, 39 ± 2 pN/nm are measured. The value found for the Berger model agrees extremely well with both previous simulation results and the most recent experimental measurement.

Acknowledgement

It seems like it was only yesterday that I stepped into CMU's campus. Time flies and I would never have been able to finish my dissertation without the guidance of my committee members, help from friends, and support from my family.

First and foremost, I would love to express my deepest gratitude to my advisor, Dr. Markus Deserno, for his excellent guidance, caring, and patience. His rigorous scientific attitude shows me what it takes to be a good scientist, the way he treats others teaches me how to be a sincere person and care about others. Everything I learnt from Markus will be with me in the future and I want to thank him for that.

I would love to thank Prof. Robert Tilton, Prof. John Nagle, and Prof. Manfred Paulini for being my committee members, and their insightful questions and suggestions really help me.

I have met so many wonderful colleagues and friends here, and they make my life in Pittsburgh memorable. I would like to thank Patrick Diggins IV, Zach McDargh, Nicholas Jin, Mert Terzi for those interesting biophysics discussions. Especial thanks go to Mingyang Hu, who taught me important knowledge of simulation when I started and helped me in many things. I would love to thank Zhou Ye, Lawrence Wang, Siyuan Liu, Xinye Liu, Siheng Chen, Zhengkun Dai, Pengyun Wang, Mingyu Tang, Fei Yu, Miaolei Yan, Tianyu Gu, Fuyi Li, Rulin Chen, Peijun Han, Xianglin Liu and many many others. They were always there cheering me up and stood by me through the good times and bad.

Finally, I would love to thank my parents, and my younger brother. Their support and encouragement were worth more than I can express on paper.

Contents

1	Introduction	10
1.1	Biological Membranes	10
1.1.1	Membranes, Most Important Hallmarks of Life	10
1.1.2	Membranes and Shape	11
1.2	Biophysical Study of Membranes	12
1.2.1	The elasticity of membranes	13
1.2.2	Two important parameters in elasticity study	14
1.2.3	Thesis Overview	16
2	Theoretical Preliminaries	17
2.1	Lipids and Self-assembly	17
2.1.1	Lipid Structure	17
2.1.2	Aggregation of Lipids	18
2.1.3	Vesicles and Beyond	20
2.2	Theory of Membranes: Elasticity	20
2.2.1	Membrane Deformations	20
2.2.2	Change of Membrane Thickness	20
2.2.3	Stretching Energy and Shearing	21
2.2.4	Bending Energy	22
2.2.5	Poisson's Ratio	23
2.3	Theory of Membrane Surface Curvature	24
2.3.1	Directional Curvature and Principal Curvature	25
2.3.2	Mathematical Description of a Curved Surface	26
2.3.3	Monge Parametrization	28
2.4	Theory of Membranes: Helfrich Hamiltonian	29
2.4.1	Physical Guidelines for the Hamiltonian	29
2.4.2	Curvature Models and Helfrich Hamiltonian	31
2.4.3	Applications of the Helfrich Hamiltonian	33
2.5	Molecular Dynamics (MD) Simulation	35
2.5.1	MD Simulation and Coarse-grained Model	35
2.5.2	Coarse-grained Model Examples	36
2.5.3	United Atom Model	38

3	Determination of the Pivotal Plane Position of Fluid Lipid Membranes in Simulation	40
3.1	Introduction	40
3.1.1	The Bridge Between the Monolayer and the Bilayer	40
3.1.2	Previous work on pivotal plane identification	42
3.2	Theoretical Preliminaries for the Pivotal Plane	43
3.2.1	The choice of the Gibbs dividing surface	43
3.2.2	The parallel surface equations	45
3.2.3	Curvature dependence of the pivotal plane	45
3.3	Two Simulation Strategies	50
3.3.1	Simple Configurations Strategy	50
3.3.2	Buckle Strategy	53
3.4	Analysis & Results for Simple Configuration	62
3.4.1	Simulation Model Specifications	63
3.4.2	The Analysis Process for Cylinders and Spheres	64
3.4.3	Simple Configuration Results for Cooke Model	68
3.5	Analysis & Results for Buckles	71
3.5.1	Shape Analysis for Buckles	72
3.5.2	Buckle Results for Cooke Model	81
3.5.3	Compare across all configuration	82
3.5.4	Results for MARTINI Model	83
3.5.5	Results for Berger Model	87
3.6	Discussion of the Results	89
3.6.1	Bare numbers and a comparison with experiment	89
3.6.2	Calculating moments of the lateral stress profile	94
3.6.3	Pivotal plane and features in the stress profile	99
3.6.4	Dependence of the pivotal plane on lipid spontaneous curvature	99
3.7	Summary	101
4	Determining the lipid tilt modulus	103
4.1	Introduction	103
4.1.1	Tilt plays an important role in biological processes	103
4.2	Theoretical Framework	104
4.2.1	Hamiltonian with a lipid tilt field: the theory of Hamm and Kozlov	104
4.2.2	Hamm and Kozlov model for the buckle	106
4.2.3	Fourier expansion of the buckle	107
4.2.4	Determining the tilt field	108
4.2.5	From Pivotal Plane to Tilt modulus	112
4.3	Results for tilt modulus determination	114
4.3.1	Direct Measurement Method	114
4.3.2	Geometrical Analysis Method	117

4.4 Discussion 120
 4.4.1 Comparison with previous work 120
 4.4.2 Physical meaning behind the non-linearity of the Berger model 122
4.5 Summary 123

Glossary

A	Membrane area at bilayer midplane. 21
A_0	Membrane area for the flat membrane. 21
G	Genus of the surface. 31
H_{II}	Inverse hexagonal phase. 15
K	Total curvature. 26
K_0	Spontaneous curvature. 31
K_G	Gaussian curvature. 26
K_{stretch}	Area-stretch modulus. 21
L	The length of the buckled membrane contour along the buckling direction for a whole period. 54
L_x	The length in x direction of the box containing a buckle. 54
L_y	The length in y direction of the box containing a buckle. 54
M_{\pm}	$M_{\pm} = N_{+} \pm N_{-}$. 58
N	Number of lipids in a micelle or membrane. 19
S	Shape factor. 19
Y	Young modulus. 22
Σ	Isotropic tension. 68
\mathbf{N}	Direction of the membrane's local normal vector. 104
\mathbf{T}	Tilt field. 104
\mathbf{n}	Direction of a lipid. 104
ℓ	Characteristic length describing the range over which a tilt excitation decays. $\ell = \sqrt{\kappa_m/\kappa_{t,m}}$. 106
γ	Dimensionless buckling strain, defined as $\gamma = (L - L_x)/L$. 55
κ	Bending modulus of a lipid bilayer. 13
$\bar{\kappa}$	Gaussian curvature modulus. 31
λ	Characteristic length with the definition of $\lambda = \sqrt{\kappa/f_x}$. 55

ν	Poisson's ratio. 23
ψ_i	Angle ψ at the inflection point of a buckle, where it has the largest slope. 55
ρ	Lipid number ratio between inner and outer layer. 51
σ	Surface tension. 32
θ	Tilt angle between \mathbf{n} and \mathbf{N} . 104
a_0	Headgroup area. 19
a_{\pm}	Area per lipid in the upper(+) or lower(-) leaflet. 58
f_x	Lateral compressive stress in x direction for the buckled membrane. 54
$h(x, y)$	Height function of a membrane. 28
k_1, k_2	Principal curvatures. 31
l_{hc}	Hydrocarbon chain length. 19
m	Elliptic parameter, defined as $m = \sin^2(\psi_i/2)$. 56
q_{\pm}	$q_{\pm} = 1/a_{+} \pm 1/a_{-}$. 58
s	Arc length measured along the buckle. 54
v_{hc}	Hydrocarbon chain volume. 19
x_p	$x_p = \Delta\psi M_+^{(p)}$. 59
y_p	$y_p = LM_- - \Delta s M_-^{(p)}$. 59
A'	Area of a membrane monolayer, measured at its dividing surface. 41
K'	Total curvature of a membrane monolayer, measured at its dividing surface. 41
K'_G	Gaussian curvature of a membrane monolayer, measured at its dividing surface. 41
$K_{\text{m}0}$	Monolayer spontaneous curvature. 41
$K_{\text{p},\pm}$	Total curvature at each monolayer measured at the pivotal plane. 112
N_+	Lipid number in the outer layer for cylinder and sphere configuration, or upper layer for buckle configuration. 51
N_-	Lipid number in the inner layer for cylinder and sphere configuration, or lower layer for buckle configuration. 51

P	Smoothing parameter for spline fitting the buckle shape. 76
R	Radius for a sphere or a cylinder. 45
$\Sigma_0(\xi)$	Lateral stress profile. 42
κ_m	Monolayer bending modulus. 41
$\kappa_{t,m}$	Monolayer tilt modulus. 105
κ_t	Bilayer tilt modulus. 121
$\langle K^2 \rangle$	Average squared curvature. 68
$\langle \xi_i \rangle$	Average distance between reference bead i and a flat bilayer's midplane. 85
$\bar{\kappa}_m$	Monolayer Gaussian curvature modulus. 41
$\psi(s)$	Angle measuring the local slope of the buckled membrane's midplane with respect to the horizontal. 54
σ_h	Size of a lipid head bead. 100
σ_m	Monolayer tension. 41
$\varepsilon(\gamma)$	$\varepsilon(\gamma) = \left(\frac{2\pi\ell}{L}\right)^2 \left(1 + \frac{1}{2}\gamma + \frac{9}{32}\gamma^2 + \dots\right)$. 110
z	Distance from pivotal plane to the bilayer midplane. 45
z_0	Distance from pivotal plane to the bilayer midplane for flat membrane. 46
L_α	Lamellar phase of a membrane. 93

Chapter 1

Introduction

This chapter provides an introduction to the basics of biological membranes. We mostly focus on mechanical properties. Section 1.1 discusses the structure and functionality of membranes, while Section 1.2 revisits membrane elasticity from a biophysics perspective.

1.1 Biological Membranes

1.1.1 Membranes, Most Important Hallmarks of Life

Living creatures are the most complicated yet beautiful things in the world. Biological cells are acting as their “building blocks”. A typical human body comprises as many as 30 trillion cells [7]! Cell membranes play an essential role to make this happen.

First of all, the membrane provides a flexible mechanical structure for the cell. It maintains the physical integrity of the cell, and protects it from the outside environment. What is more, many cell organelles, such as the nucleus, or the Golgi apparatus, are essentially built from membranes. This compartmentalization is crucial. Since in order to carry multiple metabolic activities at the same time, cells need to maintain different biochemical environments, which differ for instance in their pH or protein composition [76, 94].

Besides that, cells have similar metabolic needs as higher organisms: they must take in nutrients and dispose of wastes, while other functional transport events are needed as well. A number of transport mechanisms are employed, and membranes play important roles in all of them, including passive osmosis and diffusion specifically for small molecules or ions [110], and active transmembrane protein channels and transporters, allowing bigger molecules, like sugars or amino acids, to enter the cells [119]. There are also totally different ways, such as endocytosis: absorbing

molecules by engulfing, and the opposite process, exocytosis [85].

Last but not least, membranes are the key to cell-to-cell communication and identifying cellular identity. Cells send and receive signals, from either other cells or the environment. These signals sometimes could go through the membranes directly, and sometimes they will be detected and processed by receptor sites within the membrane [133]. Hormones, neurotransmitters and immune proteins are all working in this way [77].

1.1.2 Membranes and Shape

The primary functions of membranes at the early stage of cellular life were nothing more than separating inside from outside and documenting an identity from outside. As life evolved, cells began to both compete and cooperate with one another and further specialize, which later reflected in membrane functionality as well [147]. Among all the specializations, size, shape and motion would provide a selective advantage, thus both static shape and dynamic deformation of membranes hold significant biological meanings for life.

Looking at the shapes of present day cells, from the simple spherical bacteria to complicated ramified neurons in a mammal's central nervous system (as shown in Figure 1.1), we find a startling variety of diversity and complexity. And not only the overall cell acquired specialization; in the domain of Eukarya a variety of intracellular organelles also appeared, which further diversified cellular metabolism. Golgi apparatus, mitochondria, and other organelles consisting of membranes show no less complexity than the cells, in terms of number of shape types, and some of them even show even more complicated layer structures (Figure 1.2).

All of this uniqueness in shapes has evolved to fulfill some specific function of cells or organelles. Take one simple, common cell as an illustrative example: the erythrocyte, or red blood cell, or simply RBC. It is one of the most common cells in our body (RBCs account for about 70% of all human cells [7, 127]) and responsible for transporting oxygen and carbon dioxide in the blood. Its biconcave shape increases surface area-to-volume ratio for the diffusion of oxygen and carbon dioxide into and out of the cell [25].

Not only static shape matters, but also dynamic deformations. Continuing with our RBC example, the flexible membrane of RBCs allows them to squeeze their $7\mu\text{m}$ width [129] to a smaller value to fit through the capillaries (characteristic radius of capillary for mammals is about $5\mu\text{m}$ [118]) they encounter during microcirculation (Figure 1.3) [25]. Aside from this example, we also have other critical cell processes

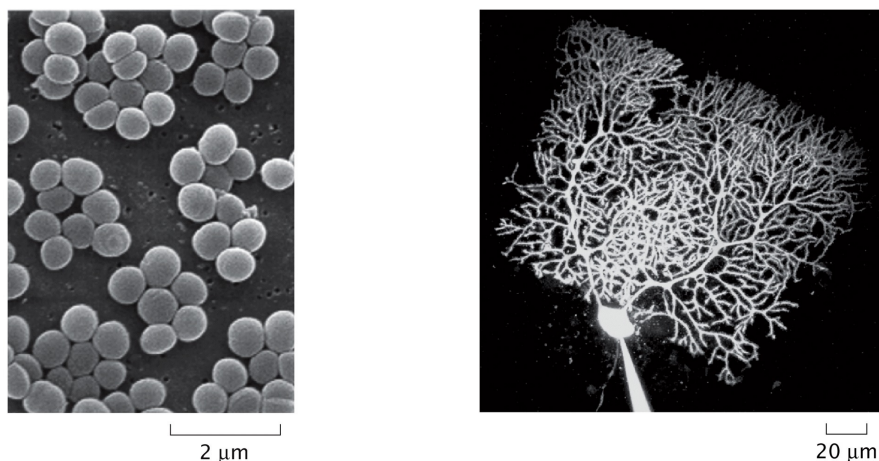


Figure 1.1: Structural variation in the complexity of shapes of cells and organelles. (Left) *Staphylococcus aureus* is a nearly spherical bacterium, one of the simplest imaginable cell shapes. (Right) A Purkinje cell in a mammalian cerebellum forms an elaborate branched tree-like structure as revealed here by injecting the cell body with a fluorescent molecule. (Images taken from Ref. [111])

involving deformation. Endocytosis, as mentioned above, requires that cells change shape to engulf cargo. And for cell growth, cell division, including binary fission, meiosis and mitosis, is the most essential step: cleavage starts to show and two new cells are formed [31]. There are many other biological process requiring shape changes, and all of them demonstrate the significance of the membrane deformation in biological activities.

Only being aware of these phenomena clearly is not enough. The shape of cells, unlike human made objects, is not the result of a higher level intelligence, but is a combined result of internal properties of the membrane, structure and processes in the cell, and the outside environment. The combined effect of all these factors leads to the various shapes as well as similar shape transformations under similar environmental conditions. And fully understanding these phenomena becomes a challenging yet essential task.

1.2 Biophysical Study of Membranes

To learn how cells form a specific shape, or how the shape changes in response to certain environmental triggers, such as temperature increase, requires knowing the energy of the system, specifically how the energy depends on shape changes. Many of these questions are in the field of physics, where biophysicists come to play.

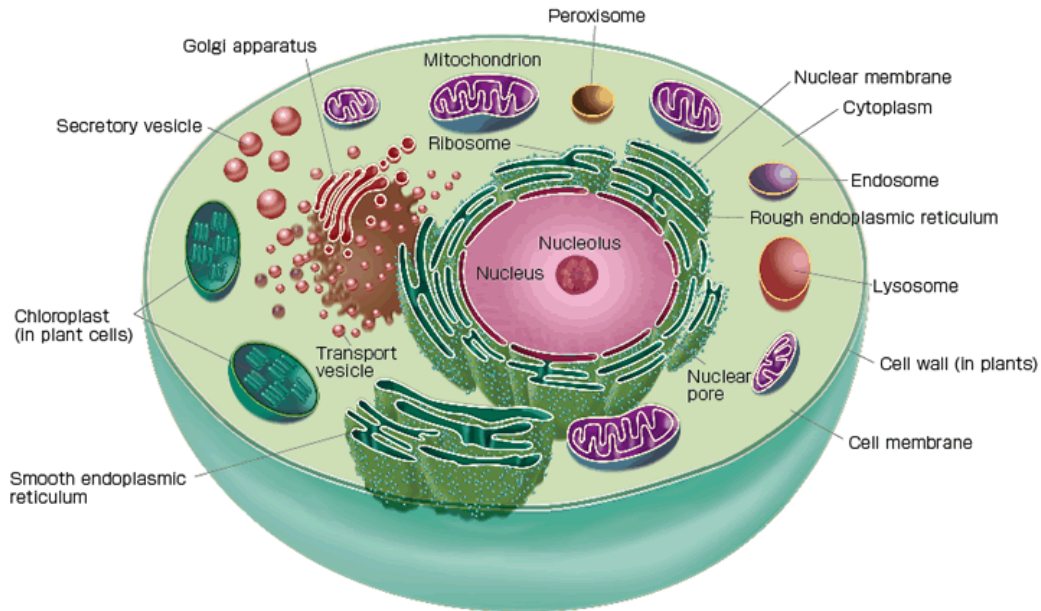


Figure 1.2: The illustration of organelles within a cell. A lot of them, including Golgi apparatus, smooth endoplasmic reticulum, nucleus and so on, have a unique shape and complicated layer structures. (Picture taken from a web textbook of University of Tokyo [2].)

1.2.1 The elasticity of membranes

A systematic analysis of this problem, as with any other physics problem, starts from a simpler yet illustrative theoretical model, breaking down the complex real-world problem into easier cases. And any theories from the simple scenarios could be tested by calculating their consequences and comparing them with experiments or simulations. For the membrane shape case, we need to study the membrane's elasticity properties.

Elasticity of thin plates has a long history. As early as 1892, Poisson wrote down the energy for a solid membrane [112]: $H = \int dA(1/2)\kappa K^2$, where κ is the bending modulus, and K is the curvature, and dA is the area element. We will cover all these terms, together with the equations mentioned in the rest of this chapter, in more detail in Chapter 2.

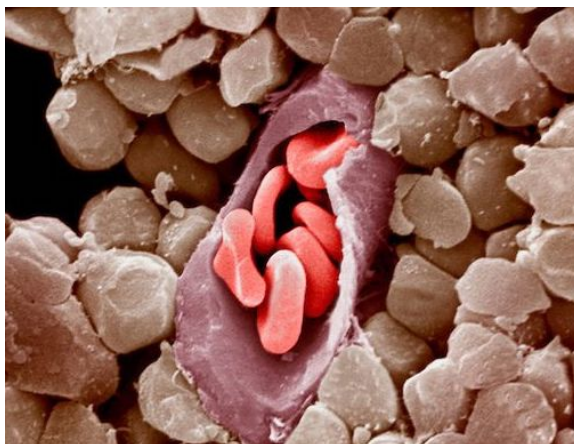


Figure 1.3: This is a colored SEM figure showing erythrocytes, or red blood cells, inside a capillary cross-section. We can see the deformation of these cells that make it possible for them to be squeezed into these tiny blood vessels [61]. To get a sense of scale, recall that a RBC has a diameter of $7\mu\text{m}$.

In the second half of the last century, physicists started to turn their interests to cell membranes. As electron microscopy developed, people gained more knowledge about the membrane architecture, and finally found that the basic structure of a biomembrane is the lipid bilayer [134], which is made up of two layers of lipids: an amphiphilic molecule with a hydrophilic head group and a hydrophobic tail group. With both layers' head pointing outwards along the local normal direction, protecting the tail part from water contact, the membrane can maintain a stable structure inside aqueous solution [137].

Many theories and models come with this finding [30], and the most famous one is the *Fluid Mosaic Model* proposed in 1972 [130]. In this model, proteins are inserted into the lipid bilayer, while the lipids can move freely in the membrane surface. In 1973, Helfrich presented a model describing the bending energy for fluid membranes [48], and since then people have been studying the membrane's shape intensively [74, 124, 149].

1.2.2 Two important parameters in elasticity study

A membrane's shape, interesting in its own right, has attracted many researchers' attention. Hence, parameters describing the elastic response of a membrane to macroscopic deformations have generally been studied with great intensity, such as the bending or stretching moduli, or the spontaneous curvature. In contrast, there are

two more microscopic parameters, equally important from a basic elastic stand point, which have received considerably less attention.

The first parameter is the position of the pivotal plane. The pivotal plane, sometimes confused with the “neutral surface”, is the location inside the membrane where the area remains invariant after the membrane is bent. In Helfrich’s theory (see next section), as well as many others, people treat the membrane as a “thin” plate, in other words, the thickness of the membrane is ignored. But the location of each layer, or the so-called “reference surface”, is still needed, and its choice influences the value of other material parameters [62, 63, 12]. The pivotal plane is one of the most common reference choice for a single membrane leaflet.

In particular, a monolayer’s reference surface (such as the pivotal plane) will lie somewhere in the middle of the lipid leaflet. However, when it comes to the case of bilayers, people invariably use the *midplane* as the reference for the membrane position and its curvature. This change in reference requires a transformation of area elements and curvatures and will hence leave a trace in the transition from a monolayer to a bilayer Hamiltonian.

The classical experimental measurement of this parameter has been done in the 1990s by Leikin *et al.* [70] by studying the inverse hexagonal phase, or H_{II} phase. We will talk more about what this phase is and how it has been used in later chapters. For now, the important point is that the H_{II} phase is not actually a lamellar phase consisting of lipid bilayers; instead, it consists of highly curved monolayer leaflets.

The other parameter is the tilt modulus. Again, many models or theories are designed for large scales, and neglect membrane thickness. This is proper in the micrometer range, but when we look down to small scales, some other factors start to play a role, including the tilt of lipids, which is the deviation of a lipid’s orientation away from the local bilayer normal.

A suitable modification of the classical curvature-only theory has been proposed by Hamm and Kozlov [44, 45] and improved by others later [86, 87, 144, 140, 72, 145, 143]. A tilt term is added to Helfrich’s original Hamiltonian, based on quadratic elastic theory, that describes thin in-plane fluid sheets subject to internal lateral prestresses. The experimental work is mostly done in a passive method: deducing the tilt modulus from the fluctuation spectra, just like the bending rigidity, which we will see in more detail in the next chapter.

Both of these parameters are important, but the current means of determining them in a simulation have their shortcomings. Hence, in this thesis we propose a simple yet precise alternative method to get these two values. This method is based

on a purely geometric analysis on an actively-bent buckle simulation. It is not only based on a more natural lamellar phase for membranes, but also avoids some of the disadvantages associated with thermal fluctuation methods. More details will be covered in later chapters.

1.2.3 Thesis Overview

This thesis comprises four chapters. The present first chapter has provided a very brief introduction to biological membrane importance and a short history of membrane elasticity studies. The second chapter presents theoretical preliminaries, and is mainly designed for people not familiar with this field. It contains basic knowledge of lipids, self-assembly mechanics, classic continuum elasticity, differential geometry and theories for membrane curvature-energy. The third chapter deals with the first parameter, the pivotal plane position and its identification, and the last chapter focusses on the second parameter, the tilt modulus.

Chapter 2

Theoretical Preliminaries

Compared to biologists, biophysicists are more focused on the physical properties of biological subjects. One thing unique about physics is that it always strives for a quantitative mathematical description of nature, and aims to explain complex situations based on the insights learned from simpler cases.

This is also the case for membrane biophysics. But in order to do that, we first need to familiarize ourselves a little bit with how physicists describe and approach this problem. In this chapter, we will review the most basic physics and mathematics knowledge in membrane elasticity, as well as a brief overview of molecular dynamics simulation, to prepare our reader for the subsequent chapters.

2.1 Lipids and Self-assembly

2.1.1 Lipid Structure

As mentioned in Chapter 1, a membrane needs to meet numerous design requirements. For example, isolating what is inside a cell from its outside environment, or compartmentalization. One promising candidate material for achieving these purposes would be “surfactants”, a name that derives from the contraction of “surface active agents”. And one particular class of surfactants, lipids, turn out to be nature’s building blocks for all cell membranes.

More than 1000 types of lipids have been identified in living cells [114]. We don’t want to study the consequences of this variety, but instead we will use one much studied lipid, DMPC (1,2-dimyristoyl-sn-glycero-3-phosphatidylcholine, or (14:0)-PC), to illustrate the molecular architecture shared by a large class of cell membrane lipids, namely, all phospholipids. DMPC, like every other lipid, is amphiphilic. That is to say, it has both a hydrophilic and a hydrophobic part. As shown in Figure 2.1, the hydrophilic head part is a positively charged choline group, linked to the phosphate

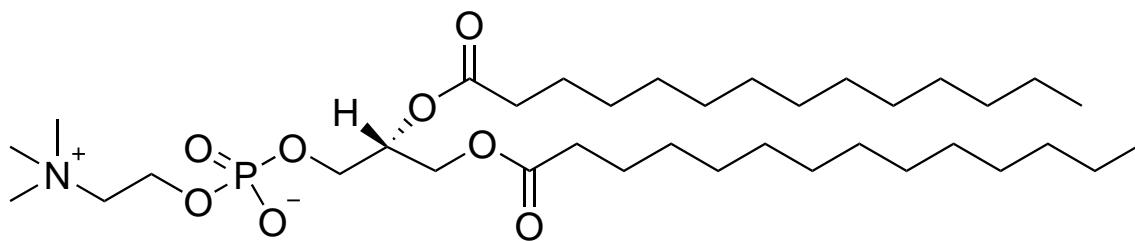


Figure 2.1: Chemical structure of DMPC [1]

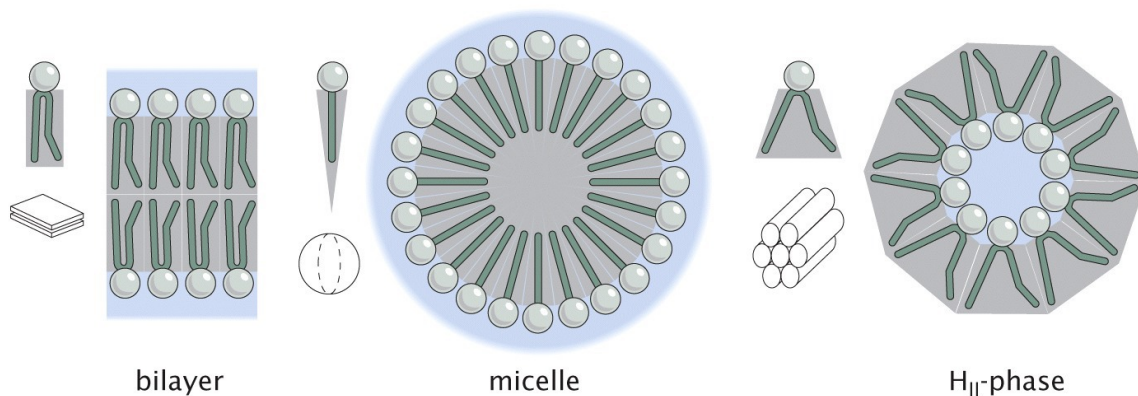


Figure 2.2: Schematic representation of lipids shape and its influence on large-scale arrangement of lipids [111].

group carrying one negative charge, making the whole lipid neutral. This terminal headgroup is hydrophilic and solvates well in water. The phosphate group connects via an ester linkage to the glycerol “backbone” of the lipid, whose remaining two hydroxyl groups are esterified to two fatty acids. Their chain length and degree of saturation determine many properties of the lipid membrane, for instance bilayer thickness and fluidity.

2.1.2 Aggregation of Lipids

Lipids in aqueous solution tend to aggregate to avoid exposing their hydrophobic tails to water, thus lowering the total free energy. As we mentioned in Chapter 1, the structure of a lipid bilayer is one possible configuration to achieve this goal, but not the only large-scale arrangement one can imagine. We can address this problem by a molecular packing argument. A more detailed discussion can be found in Ref. [58].

Figure 2.2 shows three possible arrangements for lipids; actually, there is also

another common case not shown, a cylindrical aggregate. Suppose the lipid has a headgroup area a_0 , hydrocarbon chain length l_{hc} and hydrocarbon chain volume v_{hc} . If we want to form a spherical micelle from N such lipids, then we have the total surface area and volume as below,

$$\begin{cases} Na_0 = 4\pi R^2 \\ Nv_{\text{hc}} = \frac{4}{3}\pi R^3 \end{cases} \quad (2.1)$$

Here R is the radius of the micelle. Notice that we only look at the gray part in Figure 2.2. Requiring that the center of the micelle does not have a “hole” leads to

$$R \leq l_{\text{hc}} . \quad (2.2)$$

Let us define a parameter called the shape factor S as

$$S := \frac{v_{\text{hc}}}{a_0 l_{\text{hc}}} . \quad (2.3)$$

This parameter is a dimensionless quantity, and it gives us information about single lipid shape. Smaller S means bigger head (middle case in Figure 2.2) while larger S indicates the angle between two tails is large (right case in Figure 2.2).

From Equation (2.1) and Equation (2.2), we find $S \leq 1/3$. That is to say, if the shape of surfactants meets $S \leq 1/3$, they will self-assemble into a spherical micelle. Following a similar strategy, we find the condition for cylindrical aggregates to be

$$\frac{1}{3} \leq S < \frac{1}{2} . \quad (2.4)$$

If we keep increasing S beyond $1/2$, no objects with a curvature of $1/l_{\text{hc}}$ can be assembled, and lipids tend to form a large-scale two dimensional bilayer structure. For the extreme case, a flat membrane, lipids will have the same head and tail area along the lipid, or in a more quantitative way, $S = 1$. Thus, for

$$\frac{1}{2} < S \leq 1 , \quad (2.5)$$

the bilayer structure is most favorable for lipids.

For $S > 1$, the angle between two tails gets larger, and lipids are expected to form the “inside-out” version of a micelle. In the case of hexagonally inverse packed micelles, this is called the “inverse hexagonal phase”, or H_{II} phase (rightmost case in Figure 2.2.).

One thing worth mentioning is that the discussion in this chapter is based on one assumption, namely, all lipids are of the same type. But in nature, as we mentioned before, the situation is much more complex, because membranes consist of different lipids with different tail length, existence of double C-C bonds, head group types and so on. Not to mention the fact that a lot of proteins will be inserted into a membrane as well. All these factors will contribute to the final physical properties of the membrane and in turn affect its biological functionality.

2.1.3 Vesicles and Beyond

We discussed how lipids self-assemble into different aggregates. But what happens at even larger scales? If lipids have formed a bilayer structure, how do these bilayer membranes interact with each other and their environment? This question is equivalent to the problems we mentioned in Chapter 1: How do we study the membrane shape, both static configurations and dynamic changes. One way for doing this efficiently is to apply elastic theory to membranes, and this will be covered in the following three sections

2.2 Theory of Membranes: Elasticity

Elasticity theory mainly studies one question: what is the energy change of a system if we change its shape? For a physicist, the most common approach is to break this complicated problem down into a combination of several simple yet fundamental cases. Thus, in this section, we will choose four fundamental deformations of a simplified lipid bilayer model and analyze them using proper mathematical language.

2.2.1 Membrane Deformations

As mentioned before, looking at the most relevant (from a physical perspective) basic deformation will not only provide us with better theoretical intuition, but also protect us from those minor irregular deformation's distractions.

Ref. [111] discusses four basic classes of membrane deformations (Figure 2.3): changing membrane thickness, stretching, shearing and bending.

2.2.2 Change of Membrane Thickness

Membranes in nature usually have proteins inserted into them. In most of the cases, the component lipids and proteins are not naturally matched inside the membrane, they must strain (expend energy) to match each other's hydrophobic thickness (Figure 2.4). The energy cost for this is similar to Hooke's Law, $E_{\text{width}} \propto (\Delta w)^2$, where Δw is the change of width from the membranes equilibrium state.

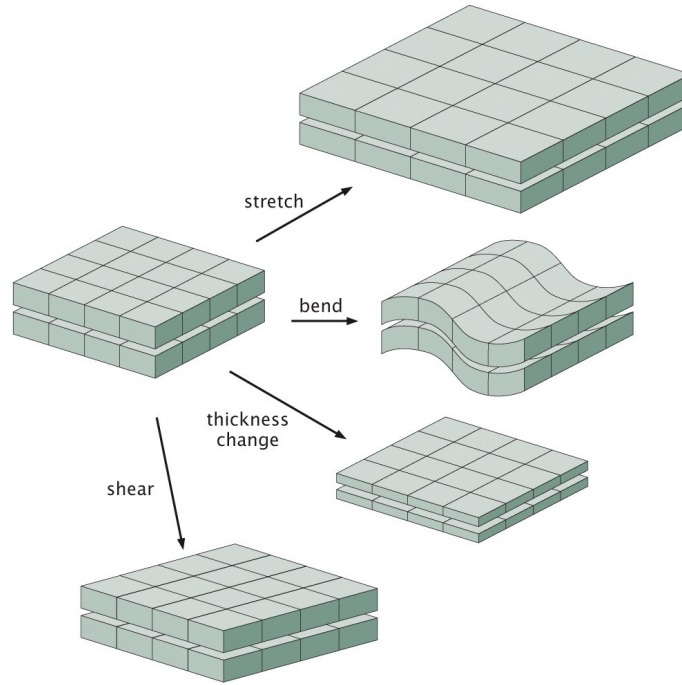


Figure 2.3: Illustration of four basic classes of membrane deformation[111]

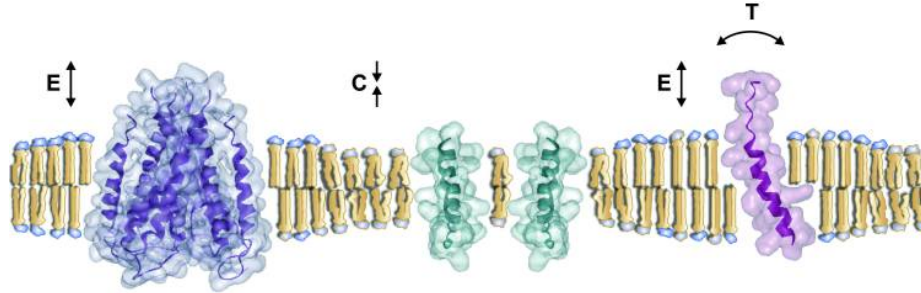


Figure 2.4: An illustration showing that a membrane may have to change its thickness to match the hydrophobic width of a protein's transmembrane region [92].

2.2.3 Stretching Energy and Shearing

Similar to a thickness change, but not in the same direction, we can consider the stretching energy in analogy to Hooke's Law as

$$E_{\text{stretch}} = \frac{1}{2} K_{\text{stretch}} \frac{(A - A_0)^2}{A_0}, \quad (2.6)$$

where K_{stretch} is the area-stretch modulus with units of energy per unit area, and A_0 and A are the membrane area before and after stretching (compressing) a relaxed

equilibrium state. Here we assume this area change is homogeneous across the whole membrane.

From this we can also get the expression for the tension Σ_{stretch} ,

$$\Sigma_{\text{stretch}} = \frac{\partial E_{\text{stretch}}}{\partial A} = K_{\text{stretch}} \frac{A - A_0}{A_0} . \quad (2.7)$$

This equation can be used to measure K_{stretch} in micropipette experiments [32, 117].

As for the lateral shear, a membrane won't resist such a deformation, unless the relative positions of lipids are fixed in some lattice structure. In other words, for membranes in the *fluid* phase, there is no proper definition for a shearing deformation, and hence no corresponding energy.

2.2.4 Bending Energy

Bending is the most interesting and dominant deformation for membranes, because it turns out to be the softest mode. Other deformations are very small compared with bending: shearing has just been discussed to be irrelevant. It is pretty natural to expect lipids to strongly resist a change of volume in the fluid phase, and this is confirmed in experiment [32]. Bending, on the other hand, changes the local volume very little. Ref. [26] also provides a very simple yet vivid analogy between paper and membrane bending, showing that stretching is much harder than bending, if a sheet is sufficiently thin.

A more formal mathematical derivation of bending energy will be covered shortly in Section 2.4. Here we only put the result for a homogeneous, thin bilayer plate without considering its Poisson ratio. The energy *per area* is [26]

$$e_{\text{bend}} = \frac{1}{96} K_{\text{stretch}} \left(\frac{h}{R} \right)^2 , \quad (2.8)$$

where h is the thickness of the plate (each layer is $h/2$), $1/R$ is the curvature of bending, $K_{\text{stretch}} := Yh$, and Y is the material's Young modulus. If we define the bending rigidity κ as

$$\kappa := \frac{1}{48} K_{\text{stretch}} h^2 , \quad (2.9)$$

then we have a quadratic relation similar to the previous section:

$$e_{\text{bend}} = \frac{1}{2} \kappa \left(\frac{1}{R} \right)^2 . \quad (2.10)$$

This could be used as a very rough way to calculate κ from K_{stretch} , but it is not very accurate because it is not immediately obvious what value we should take for h . The definition of “thickness” in a real membrane is ambiguous since more than

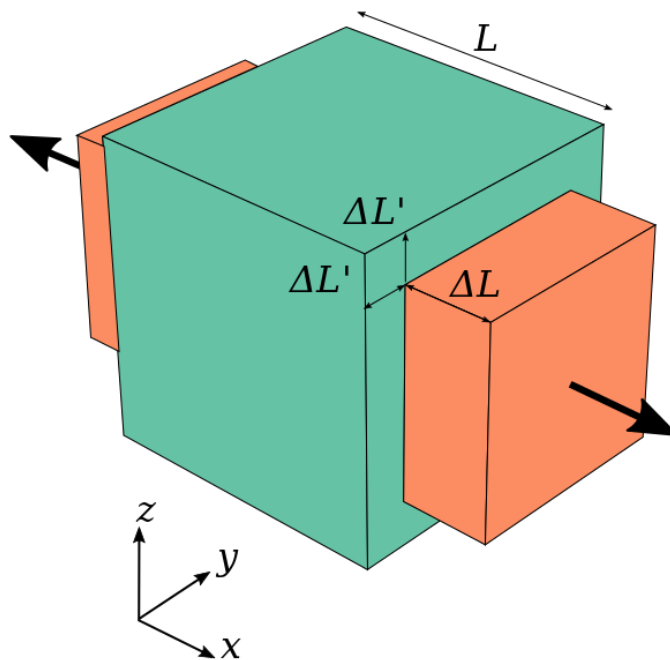


Figure 2.5: Poisson's effect for a cube.

one choice seems plausible. Do we take the width of the hydrophobic core? The separation between the phosphate groups? The distance between the Luzzati planes? This ambiguity is something we will revisit in later chapters.

2.2.5 Poisson's Ratio

All analyses in previous sections share one common assumption: ignore Poisson's effect; but this is not always negligible.

Poisson's effect is the phenomenon that a material tends to contract in the direction perpendicular to the direction of its extension. And Poisson's ratio ν is the parameter which describes the extent of this effect:

$$\nu = -\frac{d\epsilon_{\text{trans}}}{d\epsilon_{\text{axial}}} \quad (2.11)$$

Take a cube as an example, as shown in Figure 2.5, the cube is pulled in x direction, and we have

$$\nu = -\frac{d\epsilon_{\text{trans}}}{d\epsilon_{\text{axial}}} = -\frac{d\epsilon_y}{d\epsilon_x} = -\frac{d\epsilon_z}{d\epsilon_x} . \quad (2.12)$$

If we put $d\epsilon_x$ on the left hand side and integrate on both sides, we find

$$\left(1 + \frac{\Delta L}{L}\right)^{-\nu} = 1 + \frac{\Delta L'}{L} \quad (2.13)$$

Here both ΔL and $\Delta L'$ are real numbers that could also be negative. The first order approximation generates

$$\nu = -\frac{\Delta L}{\Delta L'} . \quad (2.14)$$

Thermodynamic stability confines the range for Poisson's Ratio ν to $[-1, 0.5]$, but in practice negative values (“auxetic materials”) are very rare. For most common materials Poisson's ratio is within the range $[0.3, 0.5]$, see e.g. Refs [3, 29]. And $\nu = 0.5$ corresponds to incompressible materials. One quick way to test this is from the definition of an incompressible material,

$$(x + \Delta x)(y + \Delta y)(z + \Delta z) = xyz . \quad (2.15)$$

Suppose again we pull in x direction, and the transverse direction is isotropic; in other words, $\Delta y = \Delta z$ and $y = z$. Combine all these equations, and to first order we get $2xz\Delta z + z^2\Delta x = 0$. Putting this back into the definition of ν , we get

$$\nu = -\frac{\Delta x/x}{\Delta z/z} = \frac{1}{2} . \quad (2.16)$$

Poisson's effect exists in most elastic material, and hence also in lipid membranes. Sometimes Poisson's effect only contributes a higher order term and is thus negligible; however, ignoring ν without a careful check might lead to noticeable inaccuracies. For example, for the bending energy, Ref. [69] carefully evaluates Poisson's effect, and provides a modified version of the bending energy, amending it by a prefactor of $1/(1 - \nu^2)$. If we take $\nu = 0.5$, this will bring a 33% increase! The influence of this effect is not restricted to bending and will appear again later when we set out to calculate the position of the pivotal plane, namely in Chapter 3.

2.3 Theory of Membrane Surface Curvature

We have shown that for a fluid phase bilayer membrane, the most significant deformation is bending. Hence, a key observable to describe this deformation is curvature; how much a surface is bent. The definition of curvature is rather straightforward for 1-D curves, but not quite so for 2-D surfaces. Thus, a careful and clear mathematical description, leading to a definition for surface curvature, is necessary.

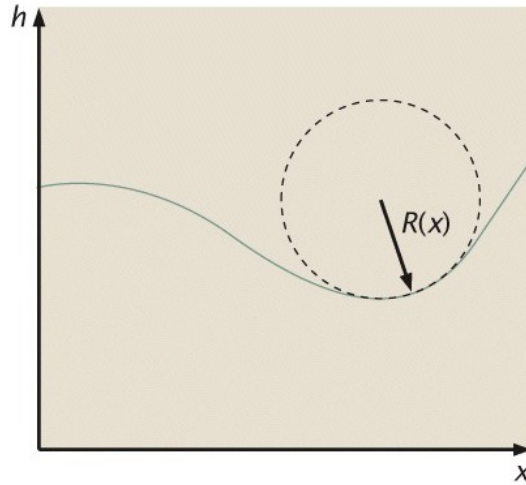


Figure 2.6: The osculating circle for illustrating a curve’s curvature (taken from Ref. [111]).

2.3.1 Directional Curvature and Principal Curvature

The curvature describes how much a curve/surface is “bent”, or how much it deviates from a straight line/flat plane. For the point on a one-dimensional smooth curve, firstly find an osculating circle, or “kissing circle”, which passes through this point, and a pair of additional points on the curve infinitesimally close to this point. The circle’s center lies on the inner normal line. And both this point and the circle share the same curvature: the inverse of this circle’s radius (as shown in Figure 2.6).

What about a two dimensional curved surface? Because most surfaces are not isotropic, there is no guarantee we could find an “oscillating sphere” similar to the circle in the one-dimensional case. Or in other words, the curvature on a surface is direction dependent. The way to deal with this is introduce a concept called *directional curvature*.

For any point on the surface, there is a unit normal vector going through this point which is perpendicular to the surface. Thus we have an infinite number of normal planes containing both the normal vector and a unique direction tangent to the surface, cutting the surface in a plane curve. Thus, we end up with a curvature (namely, that of the plane curve) for any given point and direction. This is called the directional curvature (see Figure 2.7).

Among all directional curvatures, the maximum and minimum value, k_1 and k_2 , are named *principal curvatures*, and their corresponding directions turn out to be

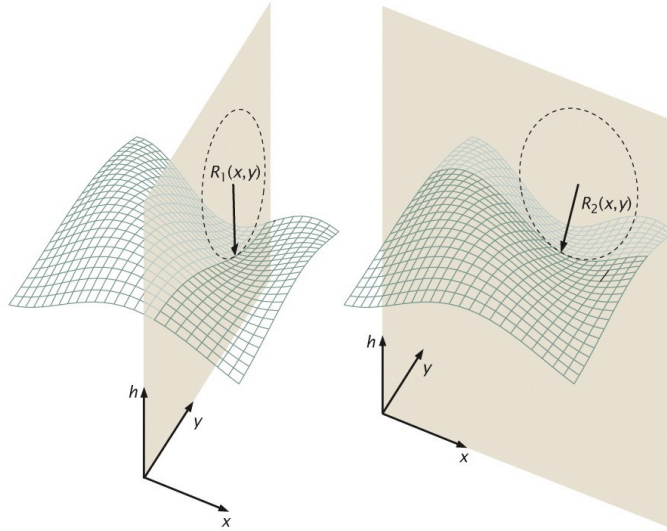


Figure 2.7: Directional curvature for a two dimensional surface (taken from Ref. [111]).

perpendicular to each other.

Based on this, we can define two new quantities, the *total curvature* K and the *Gaussian curvature* K_G , as

$$\begin{aligned} K &:= k_1 + k_2 , \\ K_G &:= k_1 k_2 . \end{aligned} \tag{2.17}$$

The choice of these two quantities has a deeper mathematical reason, and we will explain this in next section. There is also another quantity, the *mean curvature* $H = K/2$. Since it is only a factor of 2 different from the total curvature, we will only talk about K in this thesis.

2.3.2 Mathematical Description of a Curved Surface

In the last section we gave a first definition of the curvature for surfaces. Even though this definition is physically intuitive, a precise mathematical description of both the surface and the curvature is useful and will help us in our further analysis.

A membrane, as a two dimensional object located in three dimension space, can be described by two independent coordinates. Thus, the idea is to find a local coordinates system $[u^1, u^2]$ on the surface and map it to the three-dimensional space

vector $\mathbf{r}(u^1, u^2)$ that sweeps out all points on the surface. Then the tangent vectors are

$$\mathbf{e}_a := \frac{\partial \mathbf{r}}{\partial u^a} = \partial_a \mathbf{r} \quad a \in \{1, 2\} . \quad (2.18)$$

Pay attention to the position of the index, since it indicates whether it is co-variant (lower index) or contra-variant (upper index). The basic difference is how the value changes under coordinate transformations, as discussed in more detail in Ref. [27]. The unit surface normal vector is

$$\mathbf{n} := \frac{\mathbf{e}_1 \times \mathbf{e}_2}{|\mathbf{e}_1 \times \mathbf{e}_2|} . \quad (2.19)$$

Now we have everything needed to define the two important surface tensors on which the differential geometric description relies, *the first* and *the second fundamental form*. The first fundamental form, or the *metric tensor*, or simply the *metric*, is defined as

$$g_{ab} := \mathbf{e}_a \cdot \mathbf{e}_b \quad a, b \in \{1, 2\} . \quad (2.20)$$

The inspiration behind the name “metric” comes from the arc length expression

$$(ds)^2 = \sum_{a,b=1}^2 (\mathbf{e}_a du^a) \cdot (\mathbf{e}_b du^b) = \sum_{a,b=1}^2 g_{ab} du^a du^b , \quad (2.21)$$

and if we take a look at the determinant of metric and write it as g , we have

$$\begin{aligned} g &= g_{11}g_{22} - g_{12}g_{21} = |\mathbf{e}_1|^2|\mathbf{e}_2|^2 - (\mathbf{e}_1 \cdot \mathbf{e}_2)^2 \\ &= |\mathbf{e}_1|^2|\mathbf{e}_2|^2(1 - \cos^2 \phi) = |\mathbf{e}_1|^2|\mathbf{e}_2|^2 \sin^2 \phi \\ &= |\mathbf{e}_1 \times \mathbf{e}_2|^2 . \end{aligned} \quad (2.22)$$

That is to say, we could use g to represent the area element

$$dA = |\mathbf{e}_1 du^1 \times \mathbf{e}_2 du^2| = \sqrt{g} du^1 du^2 . \quad (2.23)$$

As for the second fundamental form, it is defined as

$$\begin{aligned} \mathbf{K}_{ab} &:= \mathbf{e}_a \cdot \partial_b \mathbf{n} = \partial_b (\mathbf{e}_a \cdot \mathbf{n}) - \mathbf{n} \cdot \partial_b \mathbf{e}_a \\ &= 0 - \mathbf{n} \cdot \partial_b \partial_a \mathbf{r} = -\mathbf{n} \cdot \partial_{ab} \mathbf{r} . \end{aligned} \quad (2.24)$$

This tensor is also called *extrinsic curvature tensor*. The word “extrinsic” reminds us that a normal vector is required in this definition, and a normal vector means a higher dimensional space (an “embedding”) outside the surface is involved.

The word “curvature”, as shown in Ref. [27], comes from the form of the directional curvature. We have already discussed how to get directional curvature: consider a point P on the surface and a tangent vector $\mathbf{t} = t^a \mathbf{e}_a$ at point P . The directional curvature in the direction \mathbf{t} turns out to be $K_{ab} t^a t^b$, where K_{ab} depends on the surface alone and contraction with the dyad $t^a t^b$ projects onto the \mathbf{t} -direction.

The principal curvatures we mentioned earlier in Section 2.3.1 are simply the *eigenvalues* of K_{ab} . This shows that total curvature K and Gaussian curvature K_G , as defined in Equation (2.17), are simply the trace and the determinant of the second fundamental form.¹ As such, they are geometric invariants [27]. Later we will see why the invariance property of K and K_G is important and how we can construct a Hamiltonian from them.

2.3.3 Monge Parametrization

So far, we have a pretty elegant mathematical description of general surfaces. But what about doing a calculation with an actual one? It is not easy to find a general and equally elegant specific parametrization strategy. In many cases, additional aspects, such as a surface’s special symmetry, need to be considered to make this clean. Introducing all these is not this section’s main goal, but one strategy, the *Monge Parametrization*, or the *Monge gauge*, has been used a lot in the literature, and it is helpful to cover it. The basic idea is to describe the membrane as a height function $h(x, y)$, thus

$$\mathbf{r} = (x, y, h(x, y)) , \quad (2.25)$$

and from Section 2.3.2, we have

$$\mathbf{e}_x = (1, 0, h_x) \quad \mathbf{e}_y = (0, 1, h_y) . \quad (2.26)$$

Here $h_x = \partial h / \partial x$. Thus, the metric tensor becomes

$$g_{ab} = \begin{pmatrix} 1 + h_x^2 & h_x h_y \\ h_x h_y & 1 + h_y^2 \end{pmatrix} . \quad (2.27)$$

The determinant is $g = 1 + h_x^2 + h_y^2 = 1 + (\nabla h)^2$, where $\nabla = (\partial_x, \partial_y)$ is the gradient operator in the base plane, and the area element becomes

$$dA = \sqrt{1 + (\nabla h)^2} dx dy . \quad (2.28)$$

One important simplification arises when the membrane is only weakly bent, because then $|\nabla h| \ll 1$, and we have

$$dA \approx \left[1 + \frac{1}{2} (\nabla h)^2 \right] dx dy . \quad (2.29)$$

¹We now also understand why the two principal directions are orthogonal: they are the two eigenvectors of a symmetric matrix

For the extrinsic curvature tensor, we need to know the normal vector first,

$$\mathbf{n} = \frac{\mathbf{e}_x \times \mathbf{e}_y}{|\mathbf{e}_x \times \mathbf{e}_y|} = \frac{1}{\sqrt{1 + (\nabla h)^2}} \begin{pmatrix} -h_x \\ -h_y \\ 1 \end{pmatrix}. \quad (2.30)$$

And in turn we have second fundamental form

$$K_{ab} = -\frac{1}{\sqrt{1 + (\nabla h)^2}} \begin{pmatrix} h_{xx} & h_{xy} \\ h_{yx} & h_{yy} \end{pmatrix}. \quad (2.31)$$

From this we can calculate the two invariants, total and Gaussian curvature. If we again restrict to the weak deformation limit, the simplified version is

$$K = -\text{Tr}[\partial^2 h] = -\nabla^2 h \quad (2.32)$$

$$K_G = -\det[\partial^2 h] \quad (2.33)$$

These results, including area element, total and Gaussian curvature, will be used in the next section as an illustrating example.

2.4 Theory of Membranes: Helfrich Hamiltonian

In Section 2.2, we have considered a membrane's basic deformation modes and their corresponding energy, including the most relevant bending energy. This, combined with a mathematically better description and deeper understanding of surface curvature, which we covered in Section 2.3, finally allows us to reach an improved version of the energy expression (a Hamiltonian) for the whole system. In this section, we will first derive the famous Helfrich Hamiltonian, together with other more refined forms based on it. Then we will take a look at two applications of the Helfrich Hamiltonian.

2.4.1 Physical Guidelines for the Hamiltonian

A Hamiltonian is used to describe the energy of a system as a function of its degrees of freedom, and understanding either the features or assumptions of the system is very important. Here are several essential aspects [27, 123]:

- **Length-scale separation:** Lipid length is in the nanometer range, but the size of a membrane usually is in micrometer range. This indicates the energy expression valid at large-scale should be expressible solely in terms of large-scale quantities.
- **Fluidity:** As mentioned in Section 2.2, a fluid phase membrane does not resist shear forces within the membrane.

order L^{-n}	full set of independent surface scalars
$n = 0$	1
$n = 1$	K
$n = 2$	K^2, K_G
...	...

Table 2.1: The independent geometric surface scalars list [14]

- **Insolubility:** No lipids would escape from the membrane, even though in actual experiment or simulation this is not strictly true.
- **Stretching:** If external forces are applied, any change in total area would cost a significant energy. In contrast to that, bending requires a much smaller energy and hence constitutes the “soft mode”. We may therefore ignore area changes to leading order [69].
- **Tilting:** The direction of lipids might not align with the local normal vector, and this *usually* is a high order term [93, 113, 126, 139]. But at scales comparable to the membrane thickness, it is not necessarily negligible anymore, and we will prove this in later chapters.
- **Bilayer architecture:** It is hard for lipids to change between two monolayers in *most* cases. And if there does exist a difference of lipid number, or total area, between two layers, then the Hamiltonian will couple to this area difference [67, 91, 135], giving rise to what is called the area-difference-elasticity (ADE) model.

All these considerations have guided biophysicists in modeling the system energy, and they will be the guidance for this section as well.

But before we get into all kinds of curvature models, there is one interesting perspective emphasized in Ref. [14]. The basic idea is that from the guidelines we mentioned above, the large scale energy of a bilayer membrane, ignoring the in-plane deformation, should only depend on large-scale geometric scalars. And the problem becomes how many independent surface scalars are there. According to Ref. [14], we have Table 2.1.

The energy could then be written as an area integration of an energy density using the following scalars as “basis functions”:

$$H = \int dA \{ C_0 + C_1 K + C_2 K^2 + C_2' K_G + \mathcal{O}(L^{-3}) \} . \quad (2.34)$$

If we stop at quadratic order and relabel these constant, we end up with the famous Helfrich Hamiltonian

$$H = \int dA \left\{ \sigma + \frac{1}{2} \kappa (K - K_0)^2 + \bar{\kappa} K_G \right\} . \quad (2.35)$$

2.4.2 Curvature Models and Helfrich Hamiltonian

Minimal Model

The first description of a fluid membrane as a curvature elastic surface was given by Canham in 1970 [13]. This model is called the *Minimal Model*. It only contains local curvature energy and close to the one we talked about in Section 2.2. Within this model, the bending energy density is

$$e_{\text{bend,Canham}} = \frac{1}{2}\kappa(k_1^2 + k_2^2) = \frac{1}{2}\kappa(K^2 - 2K_G) , \quad (2.36)$$

where k_1, k_2 are the principal curvatures, and κ is the elastic modulus. Observe that the model only has one elastic constant, even though there are two quadratic invariants. Also, there is no linear term.

Spontaneous Curvature Model

In 1973, Helfrich modified these two aspects of the minimal model [48]. He added a spontaneous curvature K_0 , and he distinguished the elastic modulus between the total curvature term and the Gaussian curvature term. Now we have two moduli, “bending modulus” κ and “Gaussian curvature modulus” $\bar{\kappa}$:

$$e_{\text{bend,Helfrich}} = \frac{1}{2}\kappa(K - K_0)^2 + \bar{\kappa}K_G . \quad (2.37)$$

The motivation for introducing a spontaneous curvature K_0 is mainly for membranes with different lipids in each layer, or different chemical environments on both sides. But for the simple cases, say both layers have the same lipid type, the spontaneous curvature would be 0 then. Because of this, this model is also called the *Spontaneous Curvature Model*.

Distinguishing the two moduli means that the Hamiltonian has to make fewer assumptions. But often this modification might not make a difference. Here is why: there is a theorem called the *Gauss-Bonnet Theorem* [17, 29]. It states that for a closed surface, we always have

$$\int dA K_G = 4\pi(1 - G) , \quad (2.38)$$

where G is the “genus” of the surface, a topological invariant that represents how many “handles” the surface has. For example, a sphere has no handles, so its genus is 0; a ring or “torus” has one hole in the middle and thus one handle, so $G = 1$. In other words, if the topology of the shape remains the same, the value of G won’t change either.

Obviously, the total Hamiltonian always requires an area integration sweeping over the whole surface. If we assume $\bar{\kappa}$ is a material related constant that has the same value all over the surface, then integrating the second term in Equation (2.37) becomes

$$\int dA \bar{\kappa} K_G = \bar{\kappa} \cdot 4\pi(1 - G) , \quad (2.39)$$

a value that does not change when we deform of the membrane! (Suppose no new holes would appear.) In turn, the Gaussian curvature does not affect the total energy change unless some cutting on the surface happens.

If the patch of membrane we care about is in contact with a membrane reservoir that sets the surface tension σ , such that an increase of the area of the patch by ΔA costs the energy $\sigma\Delta A$, then we can account for this change of ensemble by writing the Hamiltonian as

$$H = \int dA \left\{ \sigma + \frac{1}{2}\kappa(K - K_0)^2 + \bar{\kappa}K_G \right\} . \quad (2.40)$$

Recall from Monge gauge and the weak deformation approximation discussed in Section 2.3 that we have $dA \approx (1 + \frac{1}{2}(\nabla h)^2)dxdy$, and $K \approx -\Delta h$. The energy can then approximately be written as

$$H = \frac{1}{2} \int dxdy \{ \sigma(\nabla h)^2 + \kappa(\Delta h)^2 \} , \quad (2.41)$$

where we ignored the spontaneous curvature and the Gaussian term.

Area Difference Elasticity (ADE) Model

In the last section, we mentioned that some aspects of the bilayer architecture are essential when we construct the Hamiltonian. To be more specific, suppose there is a flat membrane, which we now suddenly bend. The outer layer will be stretched while the inner layer will be compressed. The elastic energy stored in such a deformation can be relaxed if the two layers could glide past each other and adjust the overall lipid number difference by exchanging lipids between leaflets. But for a closed topology, especially the latter is usually hard to achieve, at least on short time scales.

This effect of area-difference-elasticity (ADE) has been appreciated early on [33, 34, 47], and defined later by three independent groups [8, 125, 146]. Thus, if the lipid number in both layers is not commensurate with the area difference dictated by the shape, we would end up with an additional global elastic term in the energy, the

so-called ADE Model [123]:

$$H = \frac{1}{2} \int dA \kappa K^2 + \frac{\kappa' \pi}{8A_0 h^2} (\Delta A - \Delta A_0)^2. \quad (2.42)$$

The first term is the regular local bending energy we have seen before, while the second term is the ADE term, related to the deviation of the area difference between two layers ΔA from the equilibrium value ΔA_0 ; $2h$ is the thickness of the membrane and κ' is something called the “non local bending rigidity”. It can be expressed as

$$\kappa' := 2k^{(m)} h^2 / \pi \quad (2.43)$$

where $k^{(m)}$ is the monolayer compression modulus.

So far, we have introduced several popular curvature models and their energy roughly in historical chronological order. There are also several other related models we have not covered. For example, the Hamiltonian coupled to a lipid tilt field has not been touched yet, but this will be talked about in more details in the tilt modulus chapter.

2.4.3 Applications of the Helfrich Hamiltonian

Knowing the Hamiltonian allows us to quantitatively reason about membranes. The most widespread applications are the analysis of the shape equations and in turn thermal fluctuations of the shape.

Shape Equations

We have derived Equation (2.9), a simple and approximate expression for calculating the bending modulus. And by applying proper values for K_{stretch} (from micropipette experiments) and h (from structural studies such as X-ray scattering), we could get $\kappa \approx 6k_{\text{B}}T$, and usually tens of $k_{\text{B}}T$ would be a good evaluation for κ [57]. This tells us the membrane will keep a relatively stable shape under thermal fluctuation, which agrees with the phenomena discussed in Chapter 1. Thus, the most natural way to estimate the static shape is finding a shape minimizing the total energy.

To get the shape equation, variational calculus is needed. For Monge gauge, the energy expression is Equation (2.41). If we make a small variation of the height function $h(x, y)$, skipping the middle steps, the variation on the total energy would be

$$\begin{aligned}
\delta H &= \frac{1}{2} \int dx dy \{ \kappa (\Delta h + \Delta \delta h)^2 + \sigma (\nabla h + \nabla \delta h)^2 \} - \frac{1}{2} \int dx dy \{ \kappa (\Delta h)^2 + \sigma (\nabla h)^2 \} \\
&= \int dx dy [\kappa \Delta \Delta h - \sigma \Delta h] \delta h + \oint ds \mathbf{l} \cdot [(\kappa \Delta h) \nabla \delta h + (\sigma \nabla h - \kappa \nabla \Delta h) \delta h] .
\end{aligned} \tag{2.44}$$

The static shape requires the lowest energy, which in particular requires $\delta H = 0$. And we need to have all terms in Equation (2.44) be equal to 0. Demanding the first term in Equation (2.44) to be 0 from any choice of δh gives us the shape equation

$$\kappa \Delta \Delta h - \sigma \Delta h = 0 . \tag{2.45}$$

If we define the characteristic length $\lambda := \sqrt{\kappa/\sigma}$, the equation above becomes

$$\Delta (\Delta - \lambda^{-2}) h = 0 . \tag{2.46}$$

Solving Equation (2.46) with the appropriate boundary conditions, which come from the requirement that the second term in Equation (2.44) must vanish as well [26], will give us the static shape of the membrane. In particular, the general solution is a linear combination of eigenfunctions of the laplacian to the eigenvalues 0 and λ^{-2} , because the two operators Δ and $\Delta - \lambda^{-2}$ commute. This allows us to solve two second order differential equations instead of one fourth order one.

Flicker Spectroscopy Experiment

Even though we stated that the membrane will generally keep a stable shape, not surprisingly, there will be thermal fluctuation of that shape as well.

Suppose we have a flat membrane spanning an $L \times L$ frame. Assuming periodic boundary conditions and applying Monge gauge, we can Fourier expand the height function:

$$h(\mathbf{r}) = \sum_{\mathbf{q}} h_{\mathbf{q}} e^{i\mathbf{q}\cdot\mathbf{r}} \quad , \quad \mathbf{q} = \frac{2\pi}{L} \begin{pmatrix} n_x \\ n_y \end{pmatrix} , \tag{2.47}$$

where $n_x, n_y \in \mathbb{Z}$. Putting this expression into the results from Section 2.3.3, as well as Equation(2.41), we see that the energy in Fourier space can be written as

$$H = L^2 \sum_{\mathbf{q}} |h_{\mathbf{q}}|^2 \left\{ \frac{1}{2} \kappa q^4 + \frac{1}{2} \sigma q^2 \right\} . \tag{2.48}$$

Since these modes are independent and harmonic, we immediately get from the equipartition theorem

$$L^2 \langle |h_{\mathbf{q}}|^2 \rangle \left\{ \frac{1}{2} \kappa q^4 + \frac{1}{2} \sigma q^2 \right\} = \frac{1}{2} k_B T . \tag{2.49}$$

Thus, the mean squared thermal amplitude for each mode is

$$\langle |h_{\mathbf{q}}|^2 \rangle = \frac{k_{\text{B}}T}{L^2[\kappa q^4 + \sigma q^2]} . \quad (2.50)$$

By integrating over all modes, we have the full mean squared membrane amplitude (in the $\sigma \rightarrow 0$ limit)

$$\langle h^2 \rangle = \sum_{\mathbf{q}} \langle |h_{\mathbf{q}}|^2 \rangle \approx \frac{k_{\text{B}}T}{16\pi^3\kappa} L^2 . \quad (2.51)$$

Equation (2.50) has frequently been used to obtain the bending modulus κ in experiment, in a technique called *flicker spectroscopy* [10, 36, 122]. Indeed, the idea of measuring a physical quantity via quantifying its thermal fluctuations is quite common. This passive measuring method, together with several complementary active bending methods, are two major ways for quantifying the elastic parameters of lipid membranes.

2.5 Molecular Dynamics (MD) Simulation

2.5.1 MD Simulation and Coarse-grained Model

To understand the physical basis of the structure and function of biological macromolecules, including the membrane lipids, there is a useful and important tool: the molecular dynamic simulation, or the MD simulation. It provides the ultimate detail concerning individual particle motions as a function of time, as well as complementary information to experimental results, *e. g.* the macro observables of a system in equilibrium. What is more, since all potentials and molecules in a simulation are under control of the user, one can alter certain parameters and determine its contribution to some specific property [60].

To build such a particle-based system, one must first define all degrees of freedom within the system. For the atomically detailed model, it is obvious that each simulation particle simply corresponds to one atom. Such a system, while most closely reproducing the real biological system, demands a lot of computing resources.

Since a large system will need much longer time to equilibrate, a coarse-grained (CG) model seems a reasonable alternative: the particles, or so-called “sites”, in the CG representation typically correspond to groups of several atoms. If carefully done, this will capture the key features related to system properties of interest while eliminating the less important atomic details. The computational efficiency will increase due to a decrease in the number of degrees of freedom.

This transformation from an atomic model to a CG model actually involves two aspects: the “system mapping” and the “coordinate mapping” [100]. The former fulfills the task of mapping each individual site to a realistic atom group and associating it with an appropriate chemical character as well as “CG bonds” representing the chemical bonds to other atom groups. The latter mainly determines the configuration of the new CG model on the basis of the underlying atomistic model.

The actual process of a CG model construction, however, requires many more considerations. Different philosophies are behind various coarse-graining processes [100]: the “top-down” models focusing on the experimental observations, the “bottom-up” models stressing the fundamental description of the real material and so on. Readers who are interested can refer to Ref. [100, 60] for a more detailed review.

One thing worth mentioning is that not all atomistic models are following the one-to-one rule of mapping. There is also another class of atomistic models, the united-atom models, in which every CH, CH₂ and CH₃ are combined into a pseudo-atom. Conventionally, these are still considered as atomistic models, since all heavy atoms are represented individually [54].

2.5.2 Coarse-grained Model Examples

Here two CG models used in this thesis will be introduced: the 3-bead Cooke model and the MARTINI model for DMPC.

The Cooke Model

The generic top-down Cooke model, or the 3-bead model, is a solvent-free coarse grained model developed by Cooke and Deserno to study mesoscopic membrane physics [19, 21]. As the name indicates, the lipid consists of three beads/sites (we will use the name “beads” in our discussion): a hydrophilic “head” bead and two hydrophobic “tail” beads (as shown in Figure 2.8), whose sizes are fixed by a Weeks-Chandler-Anderson (WCA) potential:

$$V_{\text{rep}}(r; b) = \begin{cases} 4\epsilon[(b/r)^{12} - (b/r)^6 + \frac{1}{4}], & r \leq r_c \\ 0, & r > r_c \end{cases} . \quad (2.52)$$

Here, $r_c = 2^{1/6}b$ and ϵ is the unit of energy. The WCA potential is a shifted and truncated Lennard-Jones potential. The physical meaning of b is the size of the bead, and common choice of b is: $b_{\text{head,head}} = b_{\text{head,tail}} = 0.95\sigma$ and $b_{\text{tail,tail}} = \sigma$, where σ is the unit length.

Within a lipid, all three beads are linked by two **F**inite **E**xtensible **N**onlinear **E**lastic (FENE) bonds:

$$V_{\text{bond}} = -\frac{1}{2}k_{\text{bond}}r_{\infty}^2 \log[1 - (r/r_{\infty})^2]. \quad (2.53)$$

where the stiffness $k_{\text{bond}} = 30\epsilon/\sigma^2$ and the divergence length $r_{\infty} = 1.5\sigma$ are chosen.

Besides the two potentials just mentioned, a third potential between head bead and the second tail bead is applied to straighten the lipid:

$$V_{\text{bend}} = \frac{1}{2}k_{\text{bend}}(r - r_{\text{rest}})^2 \quad (2.54)$$

where $k_{\text{bend}} = 10\epsilon/\sigma^2$. It is a harmonic spring with rest length $r_{\text{rest}} = 4\sigma$. For example, if the two bonds connecting three beads have a angle θ , the harmonic bending potential will approximately be $\frac{1}{2}k_{\text{bend}}\sigma^2\theta^2$.

One thing special about the Cooke model is that it is solvent-free: it counts for the embedding solvent only implicitly. This feature is one of the reasons why this model is so computational efficient. To compensate the loss of explicit solvent molecules, an attractive interaction among all tail beads is needed:

$$V_{\text{attr}}(r) = \begin{cases} -\epsilon, & r < r_c \\ -\epsilon \cos^2 \frac{\pi(r-r_c)}{2w_c}, & r_c \leq r \leq r_c + w_c \\ 0, & r > r_c + w_c \end{cases} \quad (2.55)$$

This is an attractive potential with a depth ϵ and a width w_c , and it smoothly increase to zero from $r = r_c$ to $r = r_c + w_c$. The width w_c is a tunable parameter, and one can easily adjust the bending rigidity and area per lipid by altering the value of w_c [19].

Since we do not need to calculate the solvent molecules' motion, and there are only three beads within one lipid, the computational efficiency of the Cooke model is very high. Another advantage of this model is that we can easily change its spontaneous curvature: simply changing the ratio of the head bead to tail beads, which we will apply later in Section 3.6.4.

The MARTINI Model

Another CG model example is the MARTINI model, which is also a top-down model: instead of focusing on an accurate reproduction of structural details, the MARTINI model stresses an extensive calibration of the non-bonded interactions among all sites/beads against experiment data. Considering the balance between computational efficiency and chemical representability, the basic rule of “system mapping” is

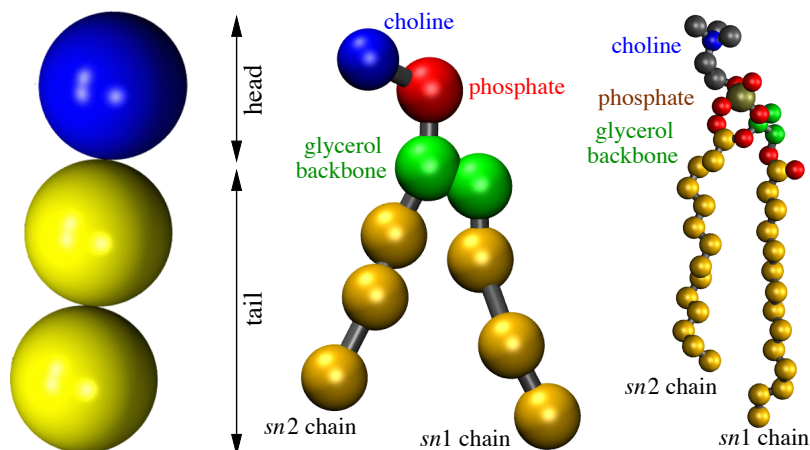


Figure 2.8: Illustration of the Cooke model for a generic lipid (left) and the MARTINI model for DMPC (middle) and Berger model for DMPC (right).

a four-to-one mapping, *i. e.*, mapping four heavy atoms to one site of all four main types, which are categorized based on the polarity and charging situation of the atom groups. For example, the DMPC lipid we mentioned in Section 2.1.1 is mapped onto 10 beads, three beads per tail (as shown in Figure 2.8). The same rule goes with the solvent molecules, and four water molecules are mapped into one CG site [79, 80, 82].

Compared with the Cooke model, the MARTINI model has a higher resolution. Since the MARTINI model aims to represent actual physical systems, its parameters are given in real SI units (nanometer, Joule), not generic CG units (σ, ϵ). But both models are top-down models. In other words, none of the models are built from the atomic structure, and we can see later this might cause errors in elasticity studies related to the coarse grained nature of lipid configurations.

2.5.3 United Atom Model

Even though CG models have many advantages, some amount of loss of information during the coarse-graining step is unavoidable. Hence, simulations on atomistic models are always good complementary information. We choose a united atom model as our atomistic model, involving the minimum simplification compared to a “full” all atom model, while maintaining the most of the structural information.

Among united atom models, the Berger model [6] is a good example. The non-polar hydrogen atoms are grouped together with carbons into one pseudo atom. The non-bonded interactions are Lennard-Jones interactions combined with the Coulomb interactions, with a fine tuning of the parameters inside these interactions on the basis

of experimental data. An illustration figure of a DMPC lipid is shown in Figure 2.8.

Chapter 3

Determination of the Pivotal Plane Position of Fluid Lipid Membranes in Simulation

The major work discussed in this chapter has been published in Ref. [141].

3.1 Introduction

3.1.1 The Bridge Between the Monolayer and the Bilayer

The structure of a lipid bilayer, as introduced before, is made up of two oppositely oriented lipid leaflets that can slide past each other and hence do not transmit lateral stress across the bilayer’s midplane. As a consequence, the microscopic origin of membrane elasticity is to be found at the monolayer level: important bilayer observables, such as the elastic moduli or the spontaneous curvature, are determined by their monolayer counterparts, as well as by parameters that are defined for the monolayer but have no equivalent on the bilayer level. Efforts to predict bilayer elastic properties from the underlying lipid architecture must hence start with the monolayer. This course of action rests on two prerequisites: **first**, we must understand how monolayer properties give rise to bilayer observables; and **second**, we need to be able to measure both the monolayer and the bilayer parameters in order to test this connection.

The first problem is fairly well under control: simple differential geometric identities for parallel surfaces suffice to lift monolayer observables onto the bilayer level. The second problem is partially solved: decent protocols exist for measuring most bilayer properties—both in experiment and in simulation. What remains a real challenge are the monolayer properties, because the “coarse-graining step” from the monolayer to the bilayer typically eliminates information, such that (some) monolayer observables can no longer be uniquely inferred from knowledge of large-scale bilayer properties.

In this chapter we show how to overcome this difficulty in one particular case: we propose a highly accurate simulation strategy for determining the pivotal plane of a bilayer’s leaflet, the position inside the monolayer where the area per lipid coincides with the flat bilayer value and hence the area strain vanishes.

Let us put this in more quantitative terms. We have written down the classical continuum-level description of fluid lipid membranes, a quadratic curvature-elastic functional, in Equation (2.40). This reasoning holds just as well for each leaflet, for which we can therefore write the monolayer equivalent of the Helfrich Hamiltonian [48]

$$H_m = \int dA' \left\{ \sigma_m + \frac{1}{2} \kappa_m (K' - K_{m0})^2 + \bar{\kappa}_m K'_G \right\} . \quad (3.1)$$

Here, dA' is the area element on the monolayer, the total curvature $K' = c'_1 + c'_2$ is the sum of the two principal curvatures, and the Gaussian curvature $K'_G = c'_1 c'_2$ is their product; the primes indicate that this geometry refers to the monolayer. Besides this, we have the monolayer tension σ_m , the monolayer spontaneous curvature K_{m0} , the monolayer bending modulus κ_m and the monolayer Gaussian curvature modulus $\bar{\kappa}_m$.

The most fundamental coarse-graining step in writing down Equation (3.1), as we mentioned in Section (2.4), is to describe a thin but still three-dimensional material in terms of a mathematical two-dimensional surface. Besides an appropriate energy functional this also requires a choice for the reference surface itself, the so-called *Gibbs dividing surface*. Its position will affect the values of most material parameters [12, 62, 63]. While this dividing surface might be chosen to lie anywhere, including outside of the monolayer, physical considerations suggest some particularly useful choices, which end up placing the dividing surface somewhere in the middle of the monolayer (see Section 3.2.1 below). In contrast, when describing a bilayer with a curvature-elastic energy functional, one would naturally pick its *midplane* as the dividing surface. This shift of reference creates a subtle difference between the monolayer Hamiltonian (3.1) and its bilayer counterpart, and it requires us to identify certain monolayer properties—in particular the distance between a monolayer’s dividing surface and the bilayer’s midplane—in order to bootstrap from the monolayer to the bilayer level. Let us give four examples:

- The monolayer spontaneous curvature contributes to the bilayer tension.
- The transition from monolayer to bilayer Gaussian modulus involves the dividing surface, as well as both monolayer spontaneous curvature and bending modulus.
- Continuum theory shows that the monolayer spontaneous curvature and the monolayer Gaussian modulus are related to moments of the lateral stress profile, centered at the dividing surface of the monolayer.

- The trans-leaflet area difference over some bilayer patch is proportional to the integrated curvature and the position of the dividing surface.

A more detailed discussion of these four examples, as well as further references, can be found in Sec. 3.4 of Ref. [27].

3.1.2 Previous work on pivotal plane identification

How does one measure monolayer properties, given that they tend to leave incomplete information in bilayer observables? One way out is to investigate curved lipid phases that essentially only consist of monolayers—most prominently the inverse hexagonal H_{II} phase. Measuring how its lattice constant changes with water or alkane content permits access to important monolayer properties, including the pivotal plane [16, 15, 39, 70, 115]. As we will see in Section 3.6.1, the H_{II} phases experiment usually requires additions of lipids with large negative curvature, in contrast to the low curvature in fluid lipid membrane’s natural state, the *lamellar phase*. As Leikin *et al.* [70] rightfully emphasize, it is remarkable how well these results can be analyzed within the framework of quadratic curvature elasticity, given how highly curved H_{II} phases are.

Unfortunately, re-creating the H_{II} setup in simulations is quite challenging, for reasons of equilibration as well as accurate pressure measurements, and has only recently been tackled by Sodt and Pastor [131]. They show that bilayer properties can be inferred from the H_{II} phase, even though with relatively large uncertainty; they also estimate that the position of the pivotal plane lies near the glycerol backbone.

Given how challenging these direct simulation approaches are, a more common indirect strategy is to infer monolayer properties from the lateral stress profile $\Sigma_0(\xi)$. For instance, continuum arguments show [41, 49, 50, 83, 84, 136] that the first moment of $\Sigma_0(\xi)$ across a monolayer is proportional to K_{m0} , a link that has been frequently exploited [41, 49, 50, 81, 83, 84, 104, 105, 107, 108, 121, 136]. No such relation exists for the pivotal plane; instead, several heuristic suggestions connect its position to certain features in $\Sigma_0(\xi)$, such as its maximum [106, 107], or its first minimum after the interfacial peak [108, 121, 138], or somewhere in-between [103].

In this chapter, we propose two simple and very direct methods for obtaining the position of the pivotal plane in simulations of lamellar phases, which are curved considerably less than an H_{II} phase. We will start with two different resolution coarse-grained models as a proof of principle: Cooke [21, 19] and MARTINI [81]; their main features have been briefly described in Section 2.5.2. Of these two methods, the conceptually simpler one only works for solvent-free models with a high lipid flip flop rate (such as Cooke), but its main purpose is to validate the more sophisticated second method. After this, we will apply our method to a model with full atomistic resolution.

3.2 Theoretical Preliminaries for the Pivotal Plane

In Chapter 2, we have covered the fundamentals of basic membrane elasticity, the differential geometry and the Hamiltonian to describe a biological membrane system. However, to better serve the specific purpose of the pivotal plane identification, there are three topics that need a more detailed discussion. These three essential points are not only the continuation of previous chapters, but also preliminaries for the subsequent sections. Section 3.2.1 will give a strict definition of the pivotal plane and clarify the difference between the pivotal plane and another already mentioned concept serving a similar purpose, the neutral surface; Section 3.2.2 illustrates the parallel surface concept and states three important differential geometric identities that hold for them; and Section 3.2.3 will show that the position of the pivotal plane does not remain unchanged upon bending, but actually depends on the local curvature. Again, readers familiar with these topics should feel free to skip this section and directly jump into the next section, where we introduce methods to determine the position of the pivotal plane.

3.2.1 The choice of the Gibbs dividing surface

Describing a thin but still three-dimensional material with a Hamiltonian of the form (3.1) requires a two-dimensional reference surface. This is not unique, so how should one pick? While no choice is “wrong”, some are more convenient than others. Here we will briefly contrast two important ones: the *neutral surface* and the *pivotal plane*.

Writing down a quadratic theory for the elastic deformation of a thin sheet involves two modes of deformation: stretching and bending. The first is defined by the area strain, the second by the curvature(s). This will involve three types of moduli: a stretching modulus, two bending moduli (for mean and Gaussian curvature, respectively), and a cross-modulus that multiplies a term that is linear in stretching and linear in bending [62]. The values of all these moduli depend on the choice of the reference surface. Interestingly, it is possible to choose the position of the Gibbs dividing surface in such a way that the cross-modulus vanishes, so that with this particular choice stretching and bending deformations decouple energetically. This special surface is called the neutral surface [63]. Its distance from any other reference surface can be calculated from the knowledge of all moduli and the spontaneous monolayer curvature, measured with respect to the latter [63]. Another elegant characterization of the neutral surface is the following: if we know the depth-dependent lateral stretching modulus of the monolayer, $\lambda(\xi)$, then the neutral surface is the position with respect to which the first moment of $\lambda(\xi)$ vanishes [12]. Campelo *et al.* have recently shown that this relation can in fact be used to find the neutral surface in simulations [12].

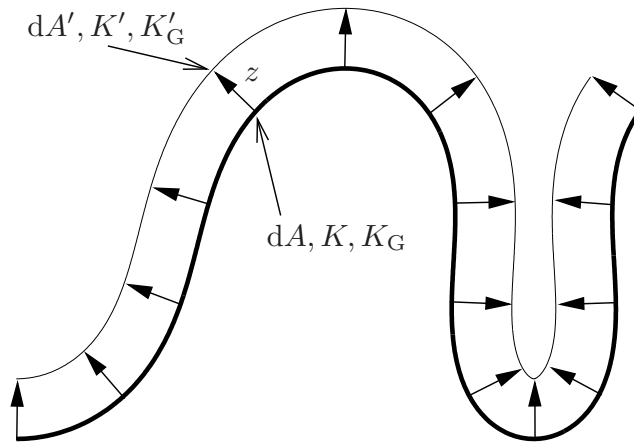


Figure 3.1: Illustration of a parallel surface, reduced by one dimension. The bold parent surface is translated at each point by a fixed distance z along its local normal vector, leading to a parallel surface with new (primed) values for area element and curvatures, which satisfy the parallel surface equations (3.3).

Alternatively, imagine bending a thin sheet. The material on its inside will be compressed, while the material on its outside will be stretched. Hence, somewhere in the material there is a position where neither compression nor stretching happens; in other words, where the area strain vanishes. This position is called the pivotal plane [115].

Unfortunately, most of the time neutral surface and pivotal plane do not coincide. But there are also exceptions; Leikin *et al.* [70] show that bending deformation of symmetrical bilayers in the absence of bilayer stretching and when the monolayers can freely slide along each other, the pivotal plane coincides with the neutral surface, which is exactly the case we are going to cover in later sections. And they also claim that the value of the spontaneous monolayer curvature changes relatively little upon switching between these two reference surfaces, but the (percental) difference in bending rigidity is four times bigger and can be significant [70]. What is more, as we will see shortly, the position of the pivotal plane changes with membrane deformation while the neutral surface remains invariant [70]. As far as monolayer observables are concerned, one hence ought to be specific with respect to which dividing surfaces they are to be understood.

3.2.2 The parallel surface equations

The difference between the dividing surface of a monolayer and the midplane of a bilayer is a centerpiece in the connection between monolayer and bilayer observables. It impacts all subsequent results because both area element and the two curvatures differ on these two surfaces. As a simple illustration, imagine a spherical surface of radius R that is displaced outwards by a distance z . The new area is $4\pi(R+z)^2$, thus the ratio of these two elements would be $(R+z)^2/R^2$, and the resulting local area element change has the form of

$$dA \longrightarrow dA' = dA \left[1 + \frac{2}{R}z + \frac{1}{R^2}z^2 \right], \quad (3.2)$$

Similar changes hold for the curvatures too. The generalization of this situation to arbitrary shapes gives rise to the notion of parallel surfaces.

Let us more formally define a parallel surface belonging to some parent surface as that surface which arises by translating each point on the parent surface by a constant distance z along the local normal vector (see Figure 3.1) [28, 132, 148]. Notice that we might have to restrict to sufficiently small z in order to avoid singularities [38]. A beautiful result in differential geometry of surfaces links the area element dA and curvatures $\{K, K_G\}$ of the parent surface to their counterparts on the parallel surface (the latter denoted by primes) [28, 132, 148]:

$$dA' = dA [1 + Kz + K_G z^2], \quad (3.3a)$$

$$dA' K' = dA K [1 + (2K_G/K)z], \quad (3.3b)$$

$$dA' K'_G = dA K_G. \quad (3.3c)$$

In our later analysis, the pivotal planes in each leaflet are parallel to the midplane of the bilayer membrane. Hence these equations provide the required transformation to a change between a monolayer and a bilayer description.

3.2.3 Curvature dependence of the pivotal plane

The position of the pivotal plane can itself change when a thin sheet is bent. To lowest order the change is proportional to the curvature, and its physical origin is a Poisson ratio effect: lateral area strains generally induce a concomitant strain along the sheet's normal, unless the Poisson ratio vanishes. This phenomenon occurs not only for solid plates but also for fluid membranes, which are not just simple isotropic fluids.

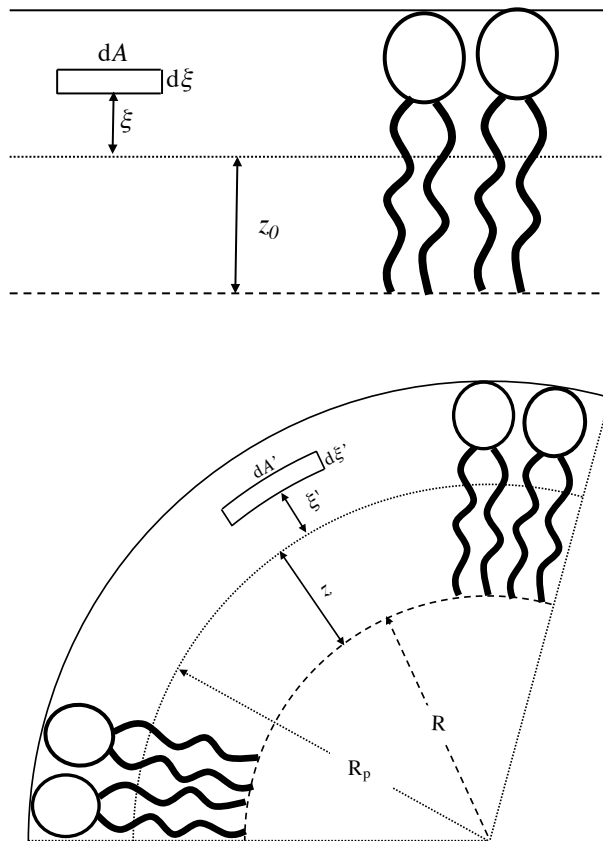


Figure 3.2: Illustration of how the pivotal plane changes with curvature. The dashed line is the midplane, the dotted line is the pivotal plane, the solid line is the interface between lipid and solvent, sometimes called the Luzzati plane. The top picture illustrates a planar leaflet and highlights some volume element $dA d\xi$ in it, a distance ξ away from the pivotal plane; the bottom picture shows the bent leaflet and indicates that the volume element changes its dimensions as well as its position within the leaflet.

Consider Figure 3.2: a single leaflet of a flat lipid membrane has its pivotal plane position some distance z_0 away from the location of the tail ends, which in a full bilayer is the location of the midplane. Upon bending the leaflet, this distance will generally move within the bilayer, $z_0 \rightarrow z(K)$. Any volume element $dA d\xi$ at position ξ therefore changes both its dimensions as well as its location. One thing worth mentioning is that the distance ξ from the area element to the pivotal plane could be negative, for instance the midplane is at $\xi = -z_0$ for a flat membrane.

Poisson's effect & Derivation

While the membrane, or the solid thin plate, is bent, the lateral area strains cannot be independent of the deformation along the normal direction. This is Poisson's effect discussed in Section 2.2.5. To be more specific in this example, the change of thickness $d\xi$ is linked to the change of area dA .

To look at it more quantitatively, we set up a local tangential coordinate system for any point in a membrane and choose an orientation in which the x - and y -axes coincide with the local principal directions and the z -axis with the normal vector. Let σ_{ij} and u_{ij} be linear stress and strain tensor, respectively. In this coordinate system both stress and strain tensor are diagonal. If we define Young modulus Y and Poisson ratio ν , the stress-strain relation within linear elasticity is [69]

$$Y u_{ij} = (1 + \nu)\sigma_{ij} - \nu\sigma_{kk}\delta_{ij} . \quad (3.4)$$

where i, j, k stand for x, y, z . Notice there is a sum implied over the index k in the second term. Considering this specific case, assume further that σ_{xx} and σ_{yy} are nonzero (and potentially different), while $\sigma_{zz} = 0$, since in the normal direction the membrane is free. Thus Equation (3.4) becomes

$$Y u_{xx} = \sigma_{xx} - \nu\sigma_{yy} \quad (3.5a)$$

$$Y u_{yy} = \sigma_{yy} - \nu\sigma_{xx} \quad (3.5b)$$

$$Y u_{zz} = -\nu\sigma_{xx} - \nu\sigma_{yy} \quad (3.5c)$$

Canceling out σ_{xx} and σ_{yy} , we find a connection between the normal and the tangential strains, namely

$$u_{zz} = -\frac{\nu}{1 - \nu}(u_{xx} + u_{yy}) . \quad (3.6)$$

Next, if $d\ell_i$ is the local line element along the principal direction i , then a distance ξ' along the normal vector the line element gets changed to $d\ell'_i = d\ell_i(1 + \xi'/R_p)$ (Recall the pivotal plane has the same line element before and after bending.). But for conveniency, we will write it down as $d\ell'_i = d\ell_i(1 + \xi'/R_i)$, where the R_i are the principal radii of curvature. Later we will see the difference of these two forms is negligible to the second order in membrane thickness. This is the one-dimensional special case of the parallel surface equation (3.3a), and since $dA' = d\ell'_1 d\ell'_2$ and $dA = d\ell_1 d\ell_2$, we can in fact recover Equation (3.3a) from its one-dimensional specializations.

Let us now look at one of the leaflets of a flat lipid bilayer, for which the pivotal plane lies a distance z_0 away from the midplane (see Figure 3.2, top). Continuing the discussion from above, consider a small volume element with area dA and thickness $d\xi$, having a distance ξ away from the pivotal plane. If we bend the leaflet, we create a local curvature K at the midplane and K_p at the pivotal plane (which are $1/R$ and

$1/R_p$ in the two-dimensional sketch of Figure 3.2, bottom). The dimensions of the little volume element become dA' and $d\xi'$, respectively. In particular, we obtain the strains along the principal directions as

$$u_{xx} = \frac{d\ell'_x - d\ell_x}{d\ell_x} = \frac{\xi'}{R_x} , \quad (3.7a)$$

$$u_{yy} = \frac{d\ell'_y - d\ell_y}{d\ell_y} = \frac{\xi'}{R_y} . \quad (3.7b)$$

Together with Equation (3.6) we hence find a differential equation that describes how volume elements in our thin surface move normally upon bending:

$$u_{zz} = \frac{d\xi' - d\xi}{d\xi} = \frac{d\xi'}{d\xi} - 1 \quad (3.8a)$$

$$u_{zz} = -\frac{\nu}{1-\nu}(u_{xx} + u_{yy}) = -\frac{\nu}{1-\nu} K \xi' , \quad (3.8b)$$

where $K = 1/R_x + 1/R_y$. Again as mentioned earlier, strictly speaking, this curvature would have to be taken at the pivotal plane, but Equations (3.3a,3.3b) show that $K_p/K = 1 + \mathcal{O}(z)$. Since we aim for a final result correct up to quadratic order in membrane thickness, it suffices to get the right hand side of this differential equation correct up to linear order in thickness variables, and hence we need not distinguish between K_p and K .

Finally, we reach an expression linking ξ' and ξ from Equation (3.8)

$$\frac{d\xi'}{d\xi} = 1 - xK\xi' , \quad (3.9)$$

where we introduced the abbreviation $x = \nu/(1-\nu)$. Separating variables and expanding to linear order in ξ' , we get:

$$d\xi = \frac{d\xi'}{1 - xK\xi'} \approx d\xi' [1 + xK\xi' + \mathcal{O}(\xi'^2)] , \quad (3.10)$$

and this is easily integrated to

$$\xi' = \xi - \frac{1}{2}xK\xi^2 + \mathcal{O}(\xi^3) . \quad (3.11)$$

This derivation seems to rely on solid mechanics, but it can in fact be generalized to the case of surfaces that are laterally fluid but exhibit a transverse shear resistance—like fluid membranes. (See Appendix C of Ref. [141].)

Pivotal Plane’s dependence on curvature

For the special case of a volume element at the midplane we obviously have $\xi = -z_0$ and $\xi' = -z$, from which we obtain the curvature dependence of the pivotal plane:

$$z = z(K) = z_0 \left[1 + \frac{1}{2}xKz_0 + \mathcal{O}(z_0^2) \right] . \quad (3.12)$$

Equation (3.12) shows that the pivotal plane position depends on curvature and hence the membrane deformation, which agrees with Ref. [70]. Plus, we can quickly check that this equation makes physical sense: for the deformation illustrated in the bottom part of Figure 3.2 all material below the pivotal plane is laterally compressed. If the Poisson ratio is positive, we therefore expect the distance between the curved midplane and the new pivotal plane to increase—which is indeed what Equation (3.12) states: a positive Poisson ratio leads to a positive x , and in turn $z > z_0$. Notice that in the incompressible limit the Poisson ratio takes its largest value $\nu = \frac{1}{2}$ (and thus we have $x = 1$), leading to the simpler relation $z \approx z_0 + \frac{1}{2}Kz_0^2$. Up to linear order in curvature this agrees with the exact result derived by Sodt and Pastor for the special case of a cylindrical deformation, for which $K = 1/R$ [131].

To get a sense for the size of this correction term, we could estimate it by evaluating both the value for Poisson ratio and local curvature. As mentioned in Section 2.2.5, the largest possible value for ν is 0.5. And for many biological materials, the value tends to be close to this incompressible limit 0.5 [42], so a good guess for x would be a little bit less than 1, since x is an increasing function of ν . For our simulation, in Section 3.6, we will see for MARTINI DMPC, $z_0 \approx 0.85\text{nm}$, and the upper bound of the local curvature satisfies $K \leq K_{\max} \approx 0.19\text{nm}^{-1}$. Hence, the correction term $\frac{1}{2}xKz_0 \approx 0.08$. This 8% correction looks small, but might not be negligible at all, not to mention when it comes to the much more highly curved H_{II} phase, as we will see later.

To summarize, the pivotal plane position will shift when a membrane is bent, and this local curvature dependence reminds us to be more clear about the state of membrane deformation, especially the local curvature when the pivotal plane position is mentioned. In order to reduce ambiguity, a good definition for the pivotal plane could be its location in a flat membrane:

$$z_0 = \lim_{K \rightarrow 0} z(K) . \quad (3.13)$$

If one is interested in the value for z at some particular point, Equation (3.12) would

provide it (with curvature induced shift) immediately.

3.3 Two Simulation Strategies

Since the pivotal plane is characterized by a purely geometric property (*i. e.*, it refers to neither energies nor forces), it can be measured with much higher accuracy in experiment than the neutral surface [70]. This geometric advantage also translates to simulations. According to parallel surface theory, if we assume both pivotal planes are parallel to the midplane, the general connection is shown in Equation (3.3). Hence if the area and local curvature is known, we can derive where the pivotal plane is. What is more, the pivotal plane holds a convenient good property due to its own definition: the area per lipid remains unchanged after bending. So measuring areas reduces to counting lipids. Even though difficult in experiment, this is easy in simulations, and both our proposed protocols rely on it.

The general strategy is as follows: create a curved membrane configuration, and count the number of lipids in opposing leaflets. Given the membrane’s curvature, their number difference can be used to access the pivotal plane position. The complexities of the membrane’s shape will directly determine how hard each specific question is. Thus the simplest strategy is to use closed vesicles, such as spheres and (periodically connected) cylinders, and we will discuss this in Section 3.3.1. In this case it is crucial that the number of lipids in both leaflets—the observable to be measured—can actually equilibrate. If it can not, then one needs more sophisticated geometries which avoid this difficulty; we propose that a lipid membrane buckle will work, and discuss the details in Section 3.3.2.

3.3.1 Simple Configurations Strategy

Two simple configurations will be covered in this sub-section: cylinder and sphere. Even though the geometry is straightforward, the Poisson effect term in Equation (3.12) renders the solution not quite as trivial as the simple configuration would otherwise suggest.

Cylinder Case

Starting with the cylinder case, consider a cylindrical bilayer membrane, periodically connected across the simulation box with its axis coinciding with the z -axis. (Notice that here the label “ z ” for the z axis has nothing to do with the pivotal plane position $z(K)$.) There are two leaflets, we call them “inner” and “outer” layer respectively, and use subscript “ $-$ ” representing the inner layer while “ $+$ ” representing the outer

layer. Suppose the radius for the bilayer midplane is R , and the curvature is $K = 1/R$. And obviously the radii $R_{p\pm}$ for each leaflet's pivotal plane are

$$R_{p\pm} = R \pm z(\pm K) . \quad (3.14)$$

Since both pivotal planes have the same area per lipid, a_0 , we have the lipid number ratio $\rho = N_+/N_-$ as

$$\rho \equiv \frac{N_+}{N_-} = \frac{R + z(+K)}{R - z(-K)} \approx \frac{R + z_0 + \frac{1}{2}xz_0^2/R}{R - z_0 + \frac{1}{2}xz_0^2/R} . \quad (3.15)$$

The last \approx is a direct result from Equation (3.12).

If we naïvely ignored the the Poisson correction and set $x = 0$, or in other words, we ignore the fact that pivotal plane shifts with curvature changes, the solution to Equation (3.15) becomes:

$$\overset{\circ}{z}_0 := z_0(x = 0) = \frac{\rho - 1}{\rho + 1} R . \quad (3.16)$$

If we put Equation (3.15) together with Equation (3.16), we have

$$\frac{1 + \overset{\circ}{z}_0/R}{1 - \overset{\circ}{z}_0/R} = \frac{R + z(+K)}{R - z(-K)} \approx \frac{R + z_0 + \frac{1}{2}xz_0^2/R}{R - z_0 + \frac{1}{2}xz_0^2/R} , \quad (3.17)$$

We can solve this equation for z_0 and write the result down as a series expansion in the naïve solution $\overset{\circ}{z}_0$:

$$z_0 = \overset{\circ}{z}_0 \left[1 + \frac{1}{2}xK^2\overset{\circ}{z}_0^2 + \mathcal{O}(\overset{\circ}{z}_0^4) \right] . \quad (3.18)$$

This result is quite interesting: the position of the pivotal plane itself, Equation (3.12), shifts by a term *linear* in the curvature. But the value for the pivotal plane, which is deduced from the lipid counting in the form of a naïve calculation that ignores Poisson ratio effects, has a correction term *quadratic* in curvature. Hence, at the accuracy we will strive for, this can be ignored, and so it suffices to use Equation (3.16) for determining the pivotal plane position. This is really helpful since we no longer need to know the Poisson ratio.

The deeper reason for this cancellation of the linear order is bilayer symmetry: Recall that the definition of z_0 is the value for the *flat* membrane, and the bilayer symmetry indicates the same z_0 for both the upper and the lower layer of a flat membrane. If this is not the case, and there is a difference Δ in the pivotal plane position,

we need to rewrite Equation (3.17) as:

$$\frac{1 + \dot{z}_0/R}{1 - \dot{z}_0/R} \approx \frac{R + (z_0 + \Delta) + \frac{1}{2}x(z_0 + \Delta)^2/R}{R - z_0 + \frac{1}{2}xz_0^2/R} . \quad (3.19)$$

The Δ is added to z_0 in the numerator, and repeating the calculation that lead to Equation (3.18), the solution has for z_0 :

$$z_0 = -\frac{\Delta}{2} + \dot{z}_0 \left[1 + \frac{1}{2}K\Delta\dot{z}_0 + \frac{1}{2}xK^3\Delta\dot{z}_0^2 + \mathcal{O}(\dot{z}_0^4) \right] . \quad (3.20)$$

All higher order Δ terms have been neglected. Again, any terms containing the curvature K at higher than linear order are not important. But compared to Equation (3.18), there is one extra correction term introducing the bilayer imbalance in the flat membrane, which is proportional to the curvature. And another minor shift since we did not consider such asymmetry property when we calculate the naïve solution \dot{z}_0 .

Sphere Case

We can apply a similar strategy to spherical vesicles. This time, an equation similar to Equation (3.15) can be written down as

$$\rho = \left(\frac{R + z(+K)}{R - z(-K)} \right)^2 \approx \left(\frac{R + z_0 + xz_0^2/R}{R - z_0 + xz_0^2/R} \right)^2 , \quad (3.21)$$

the biggest difference is the curvature $K = 2/R$, where R is the radius for the mid-plane of the bilayer spherical vesicle. And the naïve solution for $x = 0$ is

$$\dot{z}_0 := \frac{\sqrt{\rho} - 1}{\sqrt{\rho} + 1} R . \quad (3.22)$$

In the previous cylinder case, due to the bilayer symmetry and ignoring high order term, we could directly take the naïve solution as the value for z_0 , or the flat membrane pivotal plane position. Fortunately, the same conclusion exists for the sphere case. Specifically, the full solution for the combination of Equation (3.21) and Equation (3.22) is

$$z_0 = \dot{z}_0 \left[1 + \frac{1}{4}x(K\dot{z}_0)^2 + \mathcal{O}(\dot{z}_0^4) \right] , \quad (3.23)$$

and again, we do not need to worry about the quadratic term of K , neither do we

need to consider the bilayer asymmetry based on our assumption.

To summarize, for the simple configuration, a naïve analysis suffices to serve our purpose of finding the position of pivotal plane z_0 , while this should not be taken for granted.

Shortcomings of the Simple Configuration

These two examples have the advantage of being conceptually extremely simple, but they suffer from the problem that they can usually not be applied in a real simulation. The catch is that the key observable $\rho = N_+/N_-$ tends to equilibrate poorly. If we set up a simulation, any initial choice for N_+ and N_- can only relax to the actual equilibrium value if lipids can switch between leaflets. This happens naturally through lipid flip-flop, but for most lipid models the rate for this is much too slow (compared to typical simulation times). So unless explicit measures are taken to equilibrate this observable, counting lipids on the outside and inside of cylindrical or spherical vesicles is not a promising strategy.

It should also be mentioned that if the model contains explicit solvent, since the space is divided into an “inside” and an “outside” compartment by the membrane vesicle, the chemical potential of the solvent must also be equilibrated between these two parts. And any pressure difference between these two region in the presence of explicit solvent must be relaxed. All these are processes which take too long to happen spontaneously in simulations.

Of the two coarse grained lipid models and the one atomistic model we use, only the Cooke model contains no explicit solvent and has a sufficiently high flip-flop rate of about $10^{-4} \tau^{-1}$ [19], hence the cylinder and sphere methods are applicable. However, its main use will be to serve as a clean point of comparison with our second method, which even though much more widely applicable, is technically a bit more subtle—both in its theoretical basis as well as in its implementation. For this reason it behooves us to compare its results with a method where essentially nothing can go wrong.

3.3.2 Buckle Strategy

Simulating cylindrical vesicles has previously been proposed as a method for determining a membrane’s bending modulus [46]. This method directly measures the stress with which a membranes responds to the imposed curvature deformation (cylinder), and successfully circumvents the issue of large length scales for measuring the bending modulus. But it suffers from the same technical limitations as mentioned at the end

of the last section.

Recently another active bending approach has been proposed by Noguchi on a different configuration, eliminating these limitations [99]. The new configuration is a membrane buckle, and this method has proved remarkably successful for studying elastic properties [40, 57, 75, 95, 99]. We will now show that it can also help in the search for the pivotal plane. The buckle configuration contains the same number of lipids in both leaflets in equilibrium and hence we do not need to worry about the slow lipid flip-flop rate, but rather set the lipids' number to the same at the beginning of a simulation.

Buckle Configuration Introduction

Before we jump into the actual strategy for using a buckle configuration to determine z_0 , let us explore Noguchi's technique in a little bit more detail. Instead of following the original approach in his paper, a highly accurate and easy-to-handle series expansion proposed in Ref. [57] will be used here. This brief introduction will provide not only a better understanding of a buckle's mathematical description but also some useful formulas and conclusions for later analysis.

Consider a buckled membrane in a rectangular box with side lengths (L_x, L_y, L_z) , where the undulation moves along the x direction while the "ridges" of the buckle are parallel with the y direction. Figure 3.3 shows an $x-z$ plane cut of such a buckle.

We parametrize this membrane shape by one function: the angle $\psi(s)$ measuring the local slope of the membrane's midplane with respect to the horizontal, as a function of the arc length s measured along the buckle. We can then write down the total energy as:

$$\mathcal{E}[\psi] = L_y \int_0^L ds \left\{ \frac{1}{2} \kappa \psi^2 + f_x \left[\cos \psi - \frac{L_x}{L} \right] \right\}, \quad (3.24)$$

where L is the length of the membrane contour along the buckling direction, which is larger than the box length L_x , κ is the bending modulus, and f_x is a Lagrange multiplier to fix the x -direction box length at a given total membrane area. Physically, f_x is the lateral compressive stress in x direction, which will be determined from boundary conditions.

Recall that in Section 2.4.3 we introduced how to get the shape equation from the energy expression. Given the boundary condition $\psi(0) = \psi(L)$, the Euler-Lagrange differential equation, or the shape equation is:

$$\ddot{\psi} + \lambda^{-2} \sin \psi = 0 , \quad (3.25)$$

where the characteristic length λ is defined as:

$$\lambda^2 = \frac{\kappa}{f_x} . \quad (3.26)$$

Notice that we will restrict our solution to the lowest mode, one undulation inside the box, for the rest of our discussion. By multiplying $\dot{\psi}$ on both sides in Equation (3.25), we have

$$\frac{d(\dot{\psi} - \lambda^{-2} \cos \psi)}{ds} = 0 . \quad (3.27)$$

If we use the subscript i for the inflection point, where the buckle has the largest slope, we have $\psi_i = \psi(s_i)$ with $\dot{\psi}(s_i) = 0$. From Equation (3.27), we know $\dot{\psi} - \lambda^{-2} \cos \psi$ is a constant. The value of this constant can be chosen as the one at the inflection point, and then the first integral of Equation (3.25) is

$$\dot{\psi} = \lambda^{-1} \sqrt{2(\cos \psi - \cos \psi_i)} \quad (3.28)$$

Inserting Equation (3.28) back to Equation (3.24), we have

$$\mathcal{E} = L_y f_x (L_x - L \cos \psi_i) = f_x L L_y [2m - \gamma] , \quad (3.29)$$

where we define the dimensionless buckling strain γ as

$$\gamma = \frac{L - L_x}{L} , \quad (3.30)$$

and another variable $m = \sin^2(\psi_i/2)$.

Equation (3.27) can be separated and leads to an elliptic integral of the first kind. Thus we arrive at the expression for the shape:

$$\psi(s) = 2 \arcsin\{\sqrt{m} \operatorname{sn}[s/\lambda, m]\} , \quad (3.31a)$$

$$x(s) = 2\lambda \mathbb{E}[\operatorname{am}[s/\lambda, m], m] - s , \quad (3.31b)$$

$$z(s) = 2\lambda\sqrt{m}(1 - \operatorname{cn}[s/\lambda, m]) . \quad (3.31c)$$

But even with these expressions written down, there are still two unknown variables: ψ_i and f_x , which must be determined from the (periodic) boundary condition.

Specifically, the actual boundary condition used are $\psi(L/4) = \psi_i$ and $x(L/4) = L_x/4$, and both ψ_i and f_x are found as series expansions in γ . Here we write down

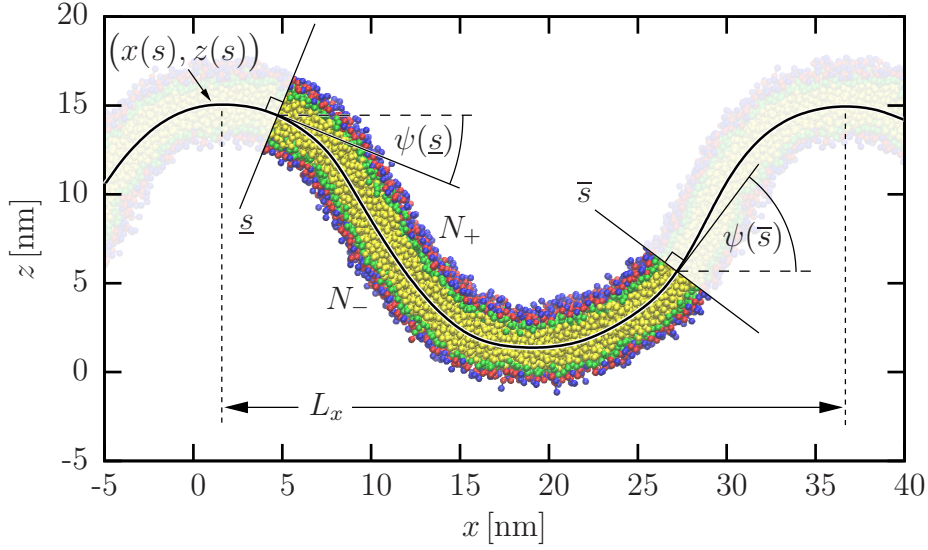


Figure 3.3: Snapshot of a MARTINI buckle simulation viewed in the xz -plane. The solid curve follows the bilayer’s midplane. Along its arc length s we pick two points—one at \underline{s} and one at \bar{s} —that cut out a segment for which we count the number of lipids N_{\pm} on the upper and lower leaflet. The boundary angles $\psi(\underline{s})$ and $\psi(\bar{s})$ are also indicated.

the expression for m instead of ψ_i for convenience in future discussions [57]:

$$m(\gamma) = \gamma - \frac{1}{8}\gamma^2 - \frac{1}{32}\gamma^3 - \frac{11}{1024}\gamma^4 - \dots, \quad (3.32a)$$

$$f_x(\gamma) = \kappa \left(\frac{2\pi}{L} \right)^2 \left[\gamma + \frac{1}{2}\gamma^2 + \frac{9}{32}\gamma^3 + \frac{21}{128}\gamma^4 + \dots \right]. \quad (3.32b)$$

To summarize, besides the advantages from the simulation point of view, the buckling method also offers a precise analytical description of the shape and the stress-strain relation. In other words, once we know the basic environmental parameters, we can calculate anything geometrical as well as the forces existing in the buckle system. Even though the shape in the simulation will fluctuate around the “standard” Euler buckle, it is still a good check during our analysis to look at a single snapshot or a time-averaged shape.

Buckle Strategy for Finding the Pivotal Plane

We now have a sense for the shape of the buckle, and now we can better appreciate the advantages of the buckling method. However, the implementation for finding z_0 turns out to be slightly more involved, though, because one of the key reasons that solves the equilibration problem will in turn render the counting problem more elaborate: for cylinders and spheres the key observable was the number difference of lipids between outside and inside leaflet, which might be hard to equilibrate. For a buckle (held conveniently under periodic boundary conditions) that difference is automatically zero in equilibrium, since the integral of the mean curvature across one period always vanishes, and so does the area difference. Therefore, since the equilibrium state contains the same number of lipids in both leaflets, we can simply set the initial configuration in this way and no longer need flip flop in later simulation.

But since the lipid number difference is now zero by construction, it does not give us any insights into the pivotal plane position. What should we do? The answer is that we need to revert to a *local* analysis, rather than consider the whole membrane all at once. Namely, we need to “cut” the buckle and only count within the cut-out part. This local counting is not as simple as the counting process for cylinders or spheres. In brief, it requires:

- Evaluating the Shape: We need to know information such as the arc length of the segment and the slope at the cut point. Since any arbitrary segment can be chosen, we need to determine the value ψ at any point.
- Cutting the Buckle: The cut should be in the direction along the local normal vector.
- Counting Lipids within the Segment: This is not trivial, since most of the time, the lipids near the cutting point are partially cut; only part of the lipid is inside the segment while the other part is outside. A choice is needed and we will discuss its implication in a later section.
- Calculating the Number Difference as a Function of z_0 : A theoretical prediction of z_0 based on the number difference is needed. And we will show how this is done.

To illustrate and parametrize our theory, the same buckle and the corresponding notations are used as in the previous section. Again, let us look at the buckle in Figure 3.3, a membrane of width L_y and (contour) length L , confined in a box of length $L_x < L$, quantified by a dimensionless buckling strain $\gamma = (L - L_x)/L$. The meaning for $\psi(s)$ and s are unchanged. Suppose some section is cut out as shown in Figure 3.3: The start- and end-point has arc length \underline{s} and \bar{s} , respectively, and both end points can be chosen arbitrarily. To distinguish the two leaflets, we use the

subscript $+$ for the upper layer and $-$ for the lower layer. The number of lipids is linked to the pivotal plane z_0 via the membrane area. Since the buckle is simply a curved plane, the midplane area element is L_y times the arc length element ds , thus the total midplane area is $A = \int L_y ds = L_y \int ds = L_y L$. From Equation (3.3a), the area of each pivotal plane A'_\pm can then be derived from a parametrization living on the midplane:

$$A'_\pm = \int dA'_\pm = \int dA [1 + K_\pm z + K_{G\pm} z^2] = L_y \int_{\underline{s}}^{\bar{s}} ds [1 \pm \dot{\psi}(s) z(\pm \dot{\psi}(s))] . \quad (3.33)$$

The two principal curvatures at the pivotal plane are $\pm\dot{\psi}$ and 0, respectively, thus we have $K_\pm = \pm\dot{\psi}$ and $K_{G\pm} = 0$. Notice that the z is the actual (*i. e.*, curvature dependant) pivotal plane position, but we want to find the value of z_0 pertaining to the flat state. So we put Equation (3.12) back into Equation (3.33) and write it down in terms of z_0 :

$$\frac{a_\pm N_\pm}{L_y} = \frac{A'_\pm}{L_y} = \int_{\underline{s}}^{\bar{s}} ds [1 \pm \dot{\psi}(s) z(\pm \dot{\psi}(s))] \quad (3.34a)$$

$$\approx \int_{\underline{s}}^{\bar{s}} ds [1 \pm \dot{\psi}(s) z_0 + \frac{1}{2} x z_0^2 \dot{\psi}^2(s)] \quad (3.34b)$$

$$= \Delta s \pm z_0 \Delta\psi + \frac{1}{2} x z_0^2 \Delta s \langle \dot{\psi}^2 \rangle_{\underline{s}}^{\bar{s}} , \quad (3.34c)$$

where we have defined the difference in arc length and angle:

$$\Delta s = \bar{s} - \underline{s} \quad \text{and} \quad \Delta\psi = \psi(\bar{s}) - \psi(\underline{s}) , \quad (3.35)$$

and where $\langle \dot{\psi}^2 \rangle_{\underline{s}}^{\bar{s}}$ is the mean square average of the curvature over the cut-out segment. This first equal sign represents the relation between surface area A_\pm and number of lipids N_\pm : $A'_\pm = a_\pm N_\pm$, where a_\pm is the area per lipid.

Let us introduce two more variables q_\pm and M_\pm as:

$$q_\pm = \frac{1}{a_+} \pm \frac{1}{a_-} \quad \text{and} \quad M_\pm = N_+ \pm N_- . \quad (3.36)$$

The motivation behind introducing these two variables will be discussed later in the subsection ‘‘Discussion of the Buckle Strategy’’. Right now, we first add/subtract Equation (3.34c) and arrive at an expression for M_\pm :

$$\frac{M_\pm}{L_y} = \frac{N_+ \pm N_-}{L_y} = z_0 \Delta\psi q_\mp + \left[1 + \frac{1}{2} x z_0^2 \langle \dot{\psi}^2 \rangle_{\underline{s}}^{\bar{s}} \right] \Delta s q_\pm . \quad (3.37)$$

Again we see the Poisson ratio term containing x making the whole expression very complicated. But fortunately this term is small enough to neglect: $\frac{1}{2} x z_0^2 \langle \dot{\psi}^2 \rangle_{\underline{s}}^{\bar{s}} \ll 1$.

We will prove this at the end of this section to avoid distracting the reader in the middle of the argument. Since the Poisson effect can be ignored, the new form of M_{\pm} looks like:

$$\frac{M_{\pm}}{L_y} = z_0 \Delta\psi q_{\mp} + \Delta s q_{\pm} . \quad (3.38)$$

In this equation, M_{\pm} , L_y , $\Delta\psi$ and Δs are either easy-to-get observables or pre-set variables from the simulation. The only two unknown variables, except for z_0 , are q_{\pm} , and it is hard to determine them with high enough accuracy directly from their definition, hence we need to determine them differently.

Remember that Equation (3.38) is valid for any part of the buckle, including for the whole period. And for a whole period, obviously we have two very simple results:

$$\Delta s^{(p)} = L \quad \text{and} \quad \Delta\psi^{(p)} = 0 , \quad (3.39)$$

where the superscript ‘‘p’’ stands for the whole period case. Inserting Equation (3.39) back into Equation (3.38), we can get expressions for q_{\pm} as

$$q_{\pm} = \frac{M_{\pm}^{(p)}}{L_y L} . \quad (3.40)$$

Focussing on M_- in Equation (3.38) and replacing q_{\pm} using Equation (3.40), we finally arrive at

$$y_p = x_p \cdot z_0 , \quad (3.41)$$

where x_p and y_p are defined as

$$x_p = \Delta\psi M_+^{(p)} \quad \text{and} \quad y_p = LM_- - \Delta s M_-^{(p)} . \quad (3.42)$$

Equations (3.41) and Equation (3.42) are the final formula helping us find the pivotal plane position z_0 . First of all, we can get the values of L , $M_{\pm}^{(p)}$ from the whole buckle. And next, for any cut-out segment, we can measure the angle difference $\Delta\psi$ between two end points as well as the arc length Δs . Thus we have a pair of x_p and y_p values for this specific cut. If we keep cutting the membrane in various ways, say fix \bar{s} at some arbitrary position and then scan \bar{s} such that Δs evenly covers the interval $[0, L]$, many sets of $\{x_p, y_p\}$ can be collected. Each pair represents a data point in the $x_p - y_p$ plane. Since Equation (3.41) tells us x_p and y_p satisfy a linear relationship, by fitting these data points with a straight line going through the origin, we can get the z_0 value, which is the slope of this fitting line.

Discussion of the Buckle Strategy

For this strategy, there are still several things that need to be clarified. To begin with, one might wonder why we choose M_- and in turn get Equation (3.41), instead of using M_+ . As a matter of fact, we can derive a similar expression using M_+ , namely

$$\left(LM_+ - \Delta s M_+^{(p)}\right) = \left(\Delta\psi M_-^{(p)}\right) \cdot z_0. \quad (3.43)$$

But this is not a good choice. We know that the ideal buckle has $M_-^{(p)} = 0$, and in simulations using models like MARTINI, a lot of the time $M_-^{(p)} = 0$, making it impossible to derive the z_0 value. Even for those with a non-zero $M_-^{(p)}$, it is a small number, and the value of y_p/x_p will have a large error, because the left hand side of (3.43) is also very small. The pivotal plane would then follow as the ratio of two small numbers, both fluctuating around zero, and this results in huge error bars.

The next thing we want to mention here is the importance of distinguishing the area per lipid for each leaflet. If both leaflets contain the same number of lipids, a_+ should be equal to a_- , and we don't need to bother using two variables and the whole derivation would be much easier. In fact, it is most likely true for many models, including the MARTINI model and the Berger model we use in this thesis, that the number of lipids in both layers is the same. But some other models, such as the Cooke model, however, do not enjoy this property. The Cooke model's easy-to-flip-flop property, as mentioned earlier, which benefits us for the simple configuration simulation, now plays against us since a small fraction of lipids (typically about 1%), might escape from the membrane during the simulation. These missing lipids cause imbalance in the lipid numbers for both layers, and in turn affect the area per lipid. And in our later analysis, we have to count the total number for each single snapshot to allow for this effect.

Last but not least, for the buckle strategy, why do we use the number difference $M_- = N_+ - N_-$, instead of the ratio N_+/N_- , as we did for the simple configuration? The short answer is to reduce the error. Specifically, for either the cylinder or the sphere case, we apply a global counting strategy. That is to say, both N_+ and N_- are relatively large numbers, and the error for each value is small. For the buckle case, however, a local counting method is taken, and many segments with various length will be used. When it comes to the case that the arc length Δs is small, both the N_+ and the N_- are small, thus the ratio is a ratio of two small numbers, which might give substantial error. But the difference can easily circumvent such small number difficulties and provide a relatively stable error across different segment sizes.

Proof that We Can Neglect the Poisson Term

We mentioned earlier that in Equation (3.37), the term $\frac{1}{2}xz_0^2\langle\dot{\psi}^2\rangle_s^{\bar{s}}$ can be ignored. Let us see why this is true.

Recall that in the first subsection of this chapter we have briefly introduced the mathematical description of the buckle configuration, and combing this with the results in Ref. [57], it is easy to show that the average squared curvature of a buckle along *one complete period* can be written as

$$\langle K^2 \rangle = \langle \dot{\psi}^2 \rangle_0^L = \frac{1}{L} \int_0^L ds \dot{\psi}^2 = \left(\frac{8\mathbb{K}(m)}{L} \right)^2 \left(m - \frac{\gamma}{2} \right), \quad (3.44)$$

where the definition of m and γ is as before, and $\mathbb{K}(m)$ is the complete elliptic integral of the first kind with parameter m . As shown in Equation (3.32a), m can be written as a series in γ , and inserting the series expansion back into the exact solution for $\langle \dot{\psi}^2 \rangle$, we get

$$\langle \dot{\psi}^2 \rangle_0^L = 2 \left(\frac{2\pi}{L} \right)^2 \left(\gamma + \frac{1}{4}\gamma^2 + \frac{3}{32}\gamma^3 + \dots \right). \quad (3.45)$$

For the term $\frac{1}{2}xz_0^2\langle\dot{\psi}^2\rangle_0^L$, let us consider the worst case scenario, in other words the largest possible value, for the Cooke model: the largest possible x is $x = 1$ for the incompressible case, and the largest strain in our simulation is $\gamma = 0.5$. A good approximation for the total arc length is $L = 67\sigma$ and $z_0 \approx 1.5\sigma$. All these result for γ , L and z_0 will be shown in the next section. Hence the Poisson term has the approximation value

$$\frac{1}{2}xz_0^2\langle\dot{\psi}^2\rangle_0^L \approx 0.011 \ll 1. \quad (3.46)$$

This is the estimation for the whole period buckle. The average squared curvature over a segment can be larger, but is still bounded by the maximum squared curvature, which the buckle assumes at its two turning points. Its value is given by a formula curiously similar to Equation (3.44) [57]:

$$\begin{aligned} K_{\max}^2 &= \left(\frac{8\mathbb{K}(m)}{L} \right)^2 m \\ &= 4 \left(\frac{2\pi}{L} \right)^2 \left(\gamma + \frac{3}{8}\gamma^2 + \frac{3}{16}\gamma^3 + \dots \right), \end{aligned} \quad (3.47)$$

showing that for all relevant strains $K_{\max}^2 \approx 2\langle K^2 \rangle$. Using the same Cooke parameters as above, we now get

$$\frac{1}{2}xz_0^2K_{\max}^2 \approx 0.025. \quad (3.48)$$

Both estimates of the whole buckle and the largest possible value show that this term will only add a few percent on top of the leading order term “1”. However, our results will show that we can determine z_0 with better than percent accuracy, so why do these few percent not matter?

The answer is because they hardly affect the slope in the $\{x_p, y_p\}$ plot. In Equation (3.42), we have $y_p = L M_- - \Delta s M_-^{(p)}$ and the correction term contributes a few percent to the term $\Delta s M_-^{(p)}$. If we compare $\Delta s M_-^{(p)}$ with another term $L M_-$ in y_p , we have

$$\frac{\Delta s M_-^{(p)}}{L M_-} = \frac{\Delta s M_-^{(p)}}{\Delta \psi M_+^{(p)} z_0 + \Delta s M_-^{(p)}} \quad (3.49a)$$

$$< \frac{\Delta s M_-^{(p)}}{\Delta \psi M_+^{(p)} z_0} \quad (3.49b)$$

$$\sim \frac{M_-^{(p)}}{K M_+^{(p)} z_0} = \frac{M_-^{(p)}}{M_+^{(p)}} \frac{1}{K z_0} . \quad (3.49c)$$

Here Equation (3.49a) is simply inserting Equation (3.41). In Equation (3.49c), we use an estimation that K is some “average” curvature for the small segment. And if we put in numbers for the Cooke model, we get $1/K z_0 \sim 5$, but $M_-^{(p)}/M_+^{(p)}$ is on the percent level. That is to say, $\Delta s M_-^{(p)}$ is a few percent of $L M_-$. Since they add together, even though the term $\Delta s M_-^{(p)}$ matters, its own few-percent correction, which is the Poisson effect correction, can be neglect.

The same reasoning applies to the MARTINI and Berger simulations.

3.4 Analysis & Results for Simple Configuration

Now we are going to apply these two strategies to various configurations and models. In particular, for the solvent free three-bead Cooke model, we will test both the simple configurations (cylinder and sphere) and the buckle, and for the more complicated MARTINI model, which is also a coarse-grained model, only buckles are simulated and analyzed due to the equilibration limitations of the model itself. Then we push our analysis even further to the full resolution atomistic Berger model.

The structure for the following two sections is as follows. This section focuses on the analysis of cylinders and spheres, which are only tested using the Cooke model.

The next section mainly talks about the buckle configuration. Since three separate models are investigated, the universal analysis process will be introduced first. Then we move on to the buckle’s result. For the Cooke model, because it has the advantage of being suitable for both strategies, we will compare the results of z_0 across three configurations. There are two possible choices for x axis: the isotropic tension Σ and the average squared curvature K^2 , both of which have definitions among three configurations. After checking the consistency between them, we will explore the MARTINI model and the Berger model.

3.4.1 Simulation Model Specifications

Before we enter the actual analysis part for both the simple and the buckle configurations. Let us specify all three models used in this study: the Cooke model, the MARTINI model and the Berger model, together with the detailed simulation parameter settings.

The Cooke Model

As we have mentioned in Section 2.5.2, the generic top-down Cooke model represents each lipid by three beads—one for the head, and two for the tail, see Figure 2.8. In the absence of solvent, aggregation is driven by an attraction between the tail beads of tunable range w_c . As a generic model, the units are (tail) bead size σ (which roughly maps as $\sigma \approx 1$ nm), Lennard-Jones energy parameter ε , and bead mass m . This gives the generic simulation time unit $\tau = \sigma \sqrt{m/\varepsilon}$. The main tuning parameters for the model are temperature T and the width of the tail attraction w_c , and we choose $k_B T = 1.1 \varepsilon$ and $w_c = 1.6 \sigma$. At this state point the area per lipid is $a_\ell \approx 1.19 \sigma^2$, and the bending rigidity is $\kappa = 12.8 k_B T$ [56]. The head bead size is regularly chosen as 95% the size of the two tail beads, but this value can be tuned to change the spontaneous curvature of the lipid. The simulations were run using ESPRESSO [73], temperature was fixed with a Langevin thermostat [43], and the time step was set to $\delta t = 0.002 \tau$. Details for how to create buckles under these conditions are described in Ref. [57]. The stress profile was calculated from 1600 snapshots of a system containing 128 lipids, using a square membrane patch with $L_x = L_y = 8.39 \sigma$ and $L_z = 10 \sigma$, which assured a membrane tension close to zero.

The MARTINI Model

The MARTINI model is a medium resolution explicit solvent CG model where on average four heavy atoms are mapped to one CG bead, as we introduced in Section 2.5.2 [80]. It can model many different lipids by choosing different tail lengths and interaction potentials. Our specific choice is DMPC (1,2-dimyristoyl-*sn*-glycero-3-phosphatidylcholine, or (14:0)-PC) which we describe by 10 beads (3 beads per tail),

see Figure 2.8. The explicit CG solvent combines four atomistic water molecules into one effective bead. We ran the simulations with GROMACS 4.5 [51], employing a Berendsen thermostat [5] and a time constant $\tau_T = 1$ ps at a reference temperature $T = 300$ K. At this state point, the area per lipid is $a_\ell \approx 0.59$ nm², and the bending rigidity (using a buckling protocol) has recently been determined to be $\kappa = (29 \pm 1) k_B T$ [56], which is about 20% smaller than the previously determined value $\kappa \approx 36 k_B T$ (based on measuring undulations) [9]. The time step is $\delta t = 40$ fs (not rescaled), and we employed a 1.2 nm-cutoff neighbor list (updated every 10 steps), a relative dielectric constant $\epsilon_r = 15$, and 1.2 nm cutoffs for Lennard-Jones and Coulomb interactions. Details for how to create buckles under these conditions are again described in Ref. [57]. The stress profile was calculated from a simulation of a system with 256 lipids and 2926 CG water molecules, using a square membrane patch with a barostat of 1 bar isotropically coupled to the xy -plane and independently along the z -direction, leading to a fluctuating box size of $L_x = L_y = (8.725 \pm 0.025)$ nm and $L_z = (8.389 \pm 0.048)$ nm, which assured a membrane tension close to zero.

The Berger Model

As introduced in Section 2.5.3. The Berger force field is a united atom atomistic force field for lipids in which nonpolar hydrogen atoms are grouped together with carbons into CH, CH₂, CH₃ beads [6]. SPC is used for water model [57]. The isothermal-isobaric ensemble was achieved by combining a Nose-Hoover thermostat [101, 53] ($\tau_T = 1.0$ ps at $T = 300$ K) and a Parrinello-Rahman barostat [109, 102] ($\tau_P = 50.0$ ps, $\kappa_{T,x} = \kappa_{T,y} = 0$, $\kappa_{T,z} = 5 \times 10^{-5}$ Pa, at 1 bar). The initial buckled configurations were backmapped from MARTINI-DMPC simulations using a special version of GROMACS [120].

3.4.2 The Analysis Process for Cylinders and Spheres

1. Exclude the Stray Lipid

The analysis for cylinders and spheres is relatively straightforward. Take the cylinder as an example: the first step is to exclude the lipids not bound within a membrane, since they would otherwise affect all subsequent calculation, *e. g.* the center position of the cylinder. The criterion to decide if a lipid is an escaped lipid is simple: for each lipid, all lipids within a certain distance threshold are named “neighbors”. Those lipids whose neighbor number is too small are regarded as an isolated lipid and will be excluded.

But it is a little bit more involved to actually apply this criterion. The first issue is that the definition of a lipid’s location is a little bit ambiguous, since every lipid has three beads and each of them is assigned with a different set of coordinates. There are multiple possible solutions to this problem: take the center of mass, declare a

certain bead as a proxy of the lipid, etc. Here, we use the head bead as the reference bead for calculation speed purpose.

In particular, the position of the head bead is treated as the lipid location, and calculating the Euclidean distance between any two lipids, accounting for the periodic boundary condition for lipids near the edge of the box. Any two lipids with a distance smaller than $r_{\text{neighbor}} = 1\sigma$ are considered as a pair of neighbors, and each lipid can have multiple neighbors. If a lipid has less than 3 neighbors, it is an isolated lipid, or a stray lipid, and can be erased from the configuration.

2. Find the Center

Then we find the center of the cylinder by averaging all remaining lipids. We only care about the x and y coordinate for cylinder axis aligned with the z -axis. Since we need to deal with the position of the lipid again, the choice of location determination is needed. Here we choose the center of mass as where the lipid is. Specifically, we will average positions of all beads, which is equivalent to averaging the center of mass of all lipids.

One thing worth mentioning is that for the purpose of cylinder center identification, both the center of mass and the reference bead strategy will give the same answer. After testing on various snapshots of cylinder systems with different radius, the discrepancy of the cylinder center between two methods is usually less than 5% of the radius.

3. Distinguish the Inner & Outer Layer

The next step is to identify which layer each lipid belongs to. Two methods are used here. The first one is to compare each lipid's orientation with the local outward-pointing membrane normal vector $\hat{\mathbf{n}}$, since lipids in the outer/inner layers should align/anti-align with $\hat{\mathbf{n}}$.

To do this, one needs to know both the local normal vector, and the lipid orientation. Given the center, the local normal is straightforward, simply pointing from the center to the lipid. The direction of this vector is not unique due to multiple choices of the lipids position. The effect of this choice, unlike the previous cylinder center calculation case, might be non-negligible for each individual lipid. For example, for a cylinder with radius $R \approx 10\sigma$, if two beads at the end of a lipid are chosen as the reference bead respectively, the difference in the corresponding normal vector can be as large as 10° , although the standard deviation of all lipids is around 3° . The deviation is about the same for other choices.

This difference results from the orientation fluctuation of the lipid. If the lipid's orientation is near perpendicular to the local normal, it is clear that choosing the head bead will differ from choosing the tail bead. A quick test for this can be in the last example, the distance between two bead is around 2σ , the worst case in which the lipid has tangential orientation, the angle would be $\arctan(2\sigma/R) \approx 11^\circ$, closed to the actual 10° .

Not only the normal vector is dependent on details of the definition, but also the lipid orientation. We will talk more about this in the tilt modulus chapter. Fortunately, for our purpose, this will not influence our analysis too much, since we only want an essentially binary discrimination between the normal vector and the lipid direction, checking if they are in the same or the opposite direction. And virtually any choice of definition will serve this purpose well.

But there are still a few lipids that cannot be classified by the first method, because sometimes the angle between the lipid direction and normal vector can be close to 90° (as the lipid in the green circle shown in Figure 3.4). Thus we introduce a second method and combine these two methods together in our analysis.

The basic idea for the second approach is to only take a look at the head bead for each lipid. These beads are well separated, hence based on the distance between lipids and center, the lipids can be clustered into two categories. One typical result from both methods is shown in Figure 3.4.

One might ask what about those few lipids located in the middle of two layers and nearly perpendicular to the normal vector? Recall that one property of the Cooke model is its high flip-flop rate. For those lipids in the process of flip-flopping, it has no physical meaning to classify them into any layer in the first place, or in other words, counting them as either layer is "correct".

4. The Radius R for the Midplane

Once we have labeled both layers, a radius can be calculated for each layer by averaging all radii of the lipids within this layer. The radius of the midplane is determined by averaging these two mean radii taken by the outer and inner lipids central bead. One thing worth mentioning is that one can not simply average the radius over all lipids, since the number of lipids is different for each leaflet.

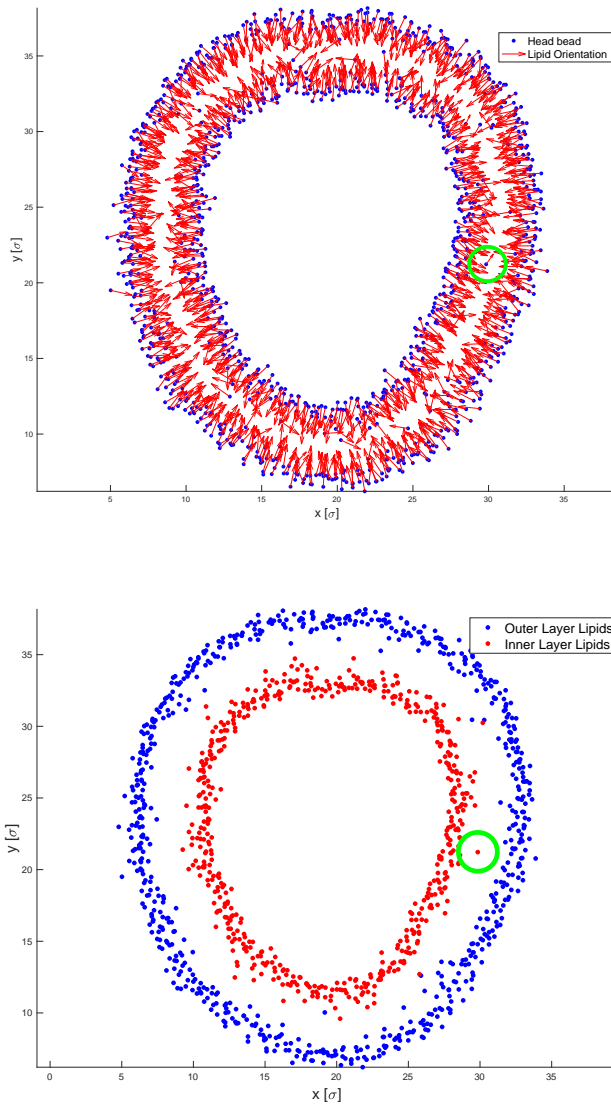


Figure 3.4: Illustration of how to determine the inner and outer layer for a cylinder configuration. Both figures show the same cylinder of 1257 lipids in the $x - y$ plane. In the upper figure, the blue dots are the head beads and the red arrow is the lipid orientation, calculating from the head and furthest tail bead. The green circle shows a bead with direction almost perpendicular to the normal vector. The lower figure shows the result of this classification, and the ambiguous lipid is labeled as the inner layer.

5. Determine the Pivotal Plane z_0

So far, for any snapshot, we have the number of lipids N_{\pm} in each layer, and the mid-plane's radius R . From Equation (3.15), we can get the value of z_0 for this snapshot.

This is done for many simulation snapshots along a trajectory, giving a mean value and an error determined via blocking [37].

The blocking error mentioned here is not the standard deviation, since the snapshots are not statistically independent from each other. Instead, we are following the blocking method proposed in Ref. [37], to estimate the error of the mean for correlated data.

The spherical case's process is similar to the cylindrical one, except that the center and normal vectors require all three coordinates.

3.4.3 Simple Configuration Results for Cooke Model

The Average Squared Curvature $\langle K^2 \rangle$ and the Isotropic Tension Σ

Recall that the Cooke model works not only for the simple configuration, but also the buckles. In order to compare our simulation results across three different geometries, we will use two variables that can be defined in all three cases. The first one is the average squared curvature $\langle K^2 \rangle$ of the membrane, the second is the isotropic surface tension Σ .

The average squared curvature for cylinders and spheres is pretty obvious. Since the curvature is $1/R$ and $2/R$, respectively, the average squared curvature is simply averaging over all lipids

$$\begin{aligned} \langle K^2 \rangle &= \left\langle \frac{1}{R^2} \right\rangle = \frac{1}{R^2} && \text{(cylinder)} \\ \langle K^2 \rangle &= \left\langle \frac{4}{R^2} \right\rangle = \frac{4}{R^2} && \text{(sphere)} \end{aligned} \quad . \tag{3.50}$$

For a buckle, the calculation is a little bit involved, but we have derived it in Section 3.3.2, and we will refer to it again in the next section.

Next, let us calculate the values of the isotropic tension Σ under which the lipids in spherical and cylindrical membranes are. The derivation for the buckle case will be covered in the next section. It is worthwhile to mention that this tension is not the total mechanical stress but rather the isotropic tangential stress that couples to the area per lipid [27].

The Helfrich shape equation [124] has the curious property that for spherical symmetry the bending contribution completely cancels from the stresses. The equation hence reduces to the Young-Laplace law $\Delta P = 2\Sigma/R$, where ΔP is the excess interior pressure and R the vesicle radius. But the Cooke model is an implicit solvent model,

and so the pressure difference between inside and outside is zero. It follows that the tension Σ is zero, too.

Cylindrical membranes have a nonzero tension, though, since they are only in equilibrium if being pulled. It is well known [11, 52] that the force to hold a cylindrical membrane tether of radius R is given by $F = 2\pi\kappa/R$, where κ is the lipid bilayer’s bending modulus, and that if the radius can equilibrate, it will be given by $R = \sqrt{\kappa/2\Sigma}$. In consequence, the tension of a cylindrical vesicle can be expressed as

$$\Sigma = \frac{\kappa}{2R^2} = \frac{F}{4\pi R} = \frac{F^2}{8\pi^2\kappa}, \quad (3.51)$$

showing that one needs two variables out of the set $\{\kappa, R, F\}$. The first one is a material parameter, which for the Cooke model at the state point we simulated has the value $\kappa = 12.8(4) k_B T = 14.1(4) \varepsilon$ [57]. Each of the other two can be extracted easily from the simulation. Since the radius follows from a simple geometrical measurement, it can usually be obtained with higher accuracy. Besides, from Equation (3.51), we can see that Σ for cylinders is clearly positive, compared with 0 for sphere, and as we can see later, negative for the buckle we investigate.

Results for the Cooke Model

R [σ]	N_{lipids}	$\Sigma \times 10^2$ [ε/σ^2]	z_0 [σ]
8.198	837	10.48	1.4782(52)
9.185	942	8.34	1.4894(57)
10.163	1047	6.82	1.4698(162)
11.142	1152	5.67	1.4871(98)
12.137	1257	4.78	1.4864(107)
			1.4862(46)

Table 3.1: Summary of Cooke model simulations in cylindrical geometry; R is the midplane radius of the cylinder, N_{lipids} the total number of lipids in the simulation box, Σ is the isotropic tension as calculated from Equation (3.51), and z_0 is the position of the pivotal plane, calculated via Equation (3.16); the bold value in the last row gives the average over all configurations. Common parameters are $L = 10\sigma$ for the cylinder length, a simulation time of $4 \times 10^4 \tau$, and 1990 configurations used for analysis.

R [σ]	N_{lipids}	time [τ]	z_0 [σ]
12.045	3000	4×10^4	1.4749(36)
13.879	4000	4×10^4	1.4850(28)
15.506	5000	2×10^4	1.4759(76)
16.981	6000	2×10^4	1.4854(60)
			1.4809(22)

Table 3.2: Summary of Cooke model simulations in spherical geometry; R is the midplane radius of the spherical vesicle, and 1990 configurations were used for analysis of each system.

For the Cooke model, the results for the cylinder configuration are listed in Table 3.1, and those for the sphere one are listed in Table 3.2. The results are also displayed in Figure 3.5, where cylinder results are solid circles and sphere results are open circles. The z_0 value result shows no dependence on either mean squared curvature or the isotropic tension. What is more, we add a shaded confidence band to the figure, and both the cylinder's $z_0 = 1.4862(46)\sigma$ and the sphere's $z_0 = 1.4809(22)\sigma$ lie in the other one's 63% confidence band. These values are close to (but a bit further out than) the position of the central bead, which is at 1.326σ . A further discussion about the physical meaning behind these specific numbers, *e. g.* comparing them with features of the stress profile, can be found in Section 3.6.

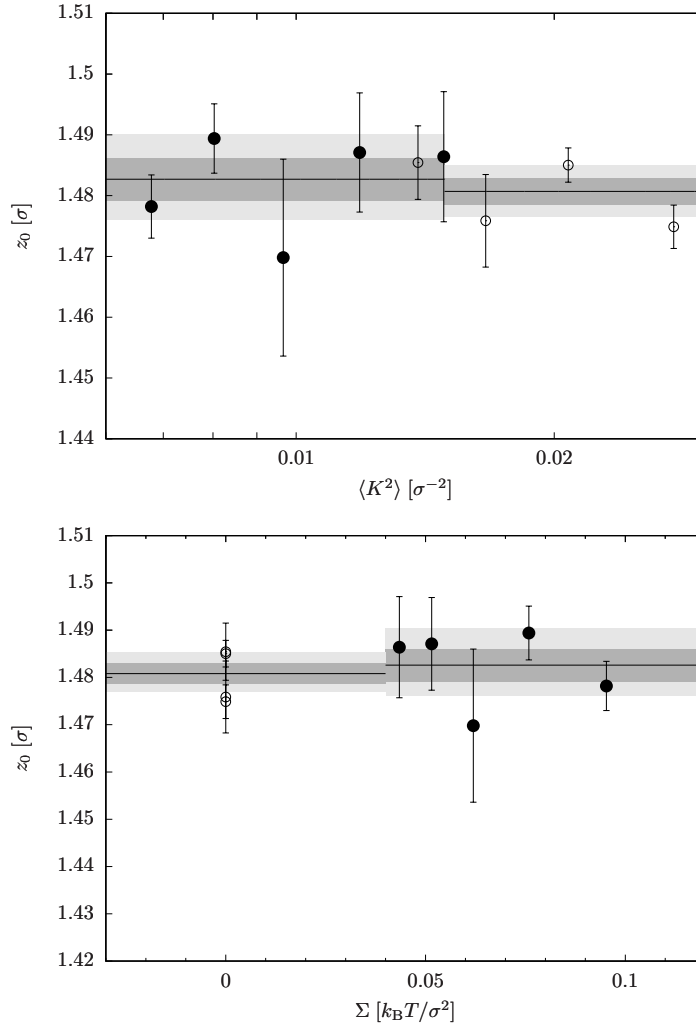


Figure 3.5: Pivotal plane position z_0 plotted against mean squared curvature $\langle K^2 \rangle$ (top) and isotropic tension Σ (bottom) for simple configurations: cylinders (filled circles) and spheres (open circles). The shaded regions are the 67% and 95% confidence bands.

3.5 Analysis & Results for Buckles

Even though one needs to be careful about certain details, the overall analysis for simple configurations is straightforward. But the buckle analysis requires more effort for two reasons: first, the shape is more complicated and we have no accurate analytical expression for every individual snapshot. Hence a shape analysis is necessary. Second, instead of counting all lipids, we need to cut the buckle in the local normal direction. For the lipids at the cutting point, it is possible that they get cut “in half”,

and how these lipids are counted is therefore not straightforward. We will solve both difficulties in our analysis process introduced as follows.

3.5.1 Shape Analysis for Buckles

1. Label Both Layers

In order to get the shape of the buckle, we need to label the lipids according to which layer they belong to, since it is not possible to fit both layers into one curve. We do not have a convenient easy-to-get parameter such as radius and normal vector as in the simple configuration case, hence we will apply a statistical method called *agglomerative hierarchical clustering* [23].

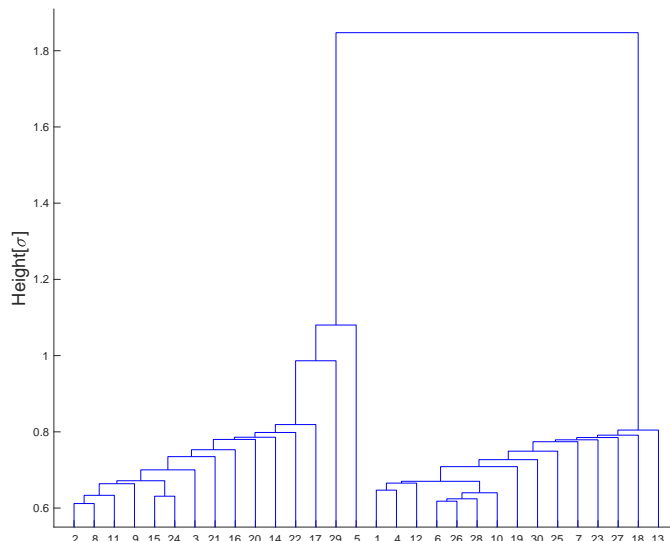


Figure 3.6: The dendrogram of one typical buckle snapshot analysis. It consists of many U-shaped lines connecting objects (lipids or small lipid clusters) in a hierarchical tree. The height of each U represents the distance between the two objects being connected. And since there are 1250 lipids, only the top part of this plot is shown.

The basic idea behind this method is clustering based on the distances or similarities among all data points. The word “agglomerative” indicates it is a bottom-up approach. In particular, one finds the two points with the shortest distance and cluster them up and treat this new cluster as a new data point. Then find the new nearest data pair again and form a new cluster. (There are multiple ways to determine the

distance between an actual data point and a cluster.) Keep repeating this process and ultimately we will have one cluster and a tree structure, or so called “dendrogram” representing the finer structure of the data points according to the distance among them. Figure 3.6 shows such a tree, and we can see that at the top part of the hierarchical tree, there are clearly two branches, corresponding to the two clusters: upper layer and lower layer. And in Figure 3.7 we show the label results of the same buckle used for Figure 3.6.

Another thing worth mentioning is that this method also has the advantage of automatically excluding any lipids which have escaped the bilayer, which happens for about 1% of the Cooke lipids. This is because the hierarchical tree will provide the information about the distance between small clusters. For the cluster containing only very little lipids (usually 1 or 2) and being too far from all other lipids, it is safe to label them as escaped lipids.

2a. Fit Each Layer (Numerical Method)

Once the monolayer is picked out from the bilayer, we can look for an analytical description of each leaflet. We choose some bead type, *e. g.* the head bead for the Cooke model, and look for a smooth surface that interpolates the positions of all beads of that type.

For this purpose, we tested three possible solutions: two analytical and one numerical method. Neither of the analytical methods work for buckles developing overhangs, because the definition of a function prevents one x value mapping to two or more y values. In contrast, the numerical approach handles the overhang problems well, but fails to provide a normal vector as accurate as the analytical approaches.

Starting with the numerical method, the general idea is to move a dot along the monolayer. If each step is small enough, the trace of the dot is a good approximation of the monolayer shape (the red dots shown in the lower plot of Figure 3.8). What is more, this method will not be limited by buckle overhangs. To be more specific, first we choose some lipid position as the starting position of the dot. And before each movement, we calibrate the dot’s position by moving it to the center of the neighbor lipids in the region (the distance threshold determining neighbor should be larger than half of the thickness). Thus we are confident it locates the center of the monolayer membrane thickness after repeating 3 or 4 such calibrations. Then we move the dot a small fixed step, in the direction perpendicular to the average of the neighbor lipids’ orientation, since this average is roughly the same direction as the local normal vector (as shown in the upper plot of Figure 3.8). Iterating this process will give us the trace of the dots and hence the surface shape.

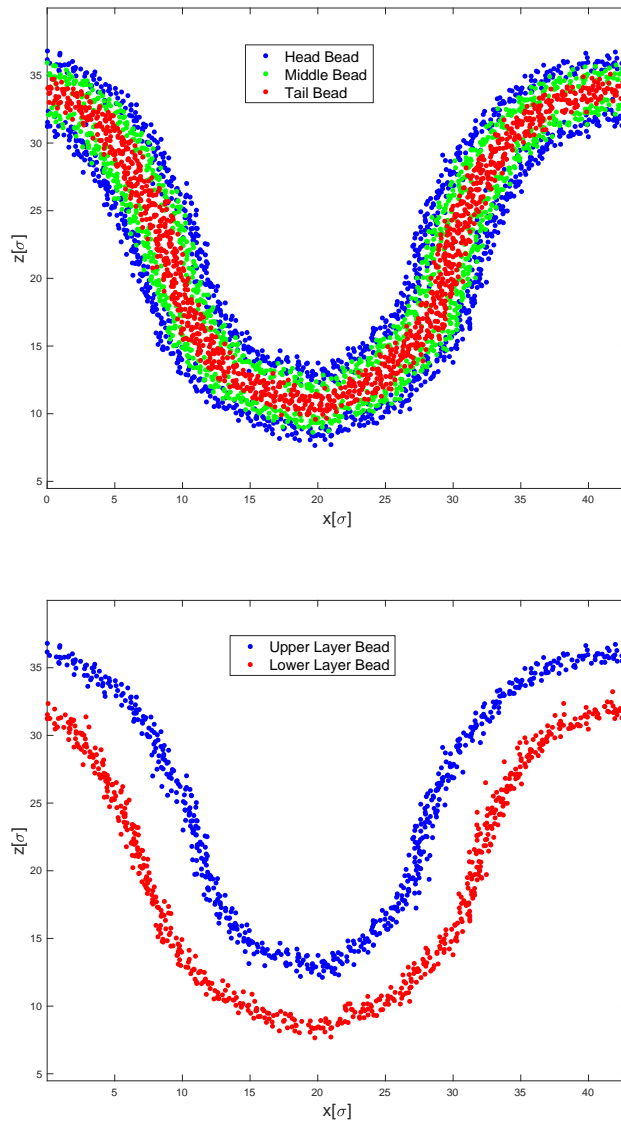


Figure 3.7: The result of upper layer label using a hierarchical clustering method. The system is a buckle membrane containing 1250 Cooke model lipids. The upper figure shows the head bead (blue dot), middle bead (green bead) and tail bead (red bead). The lower figure only plot the head bead for a clearer illustration.

Figure 3.8 shows the fitting result and we can see it deals with the overhang perfectly. But there are two disadvantages: first, it is not as easy to get the slope at any point as it is for the analytical approaches, which provides an expression for the

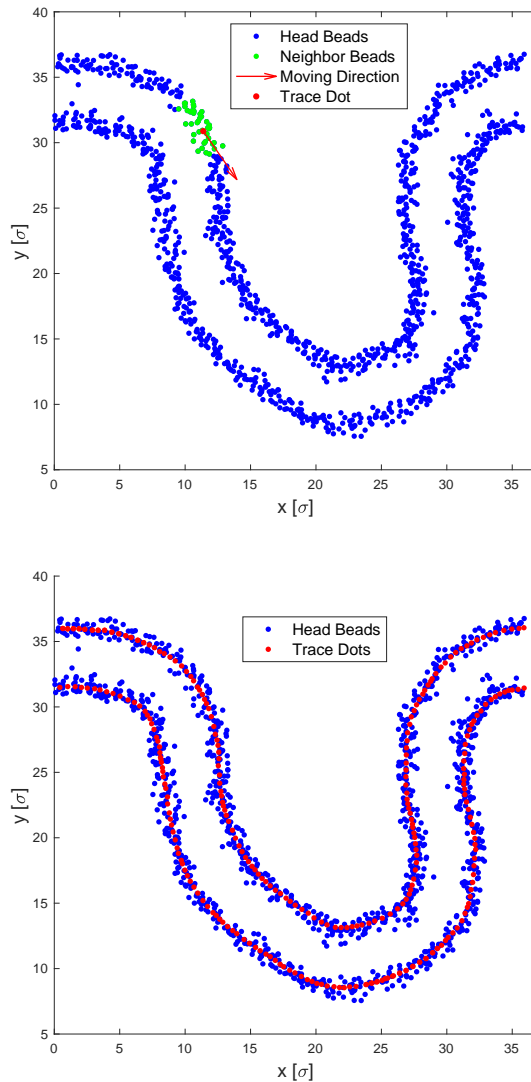


Figure 3.8: The illustration of numerical method. The upper figure shows that the tracing dot (red dot) is moving in the direction (red arrow) determined by the neighbor lipids' (green dots) orientation. And the lower figure shows that this method handles the overhang of the membrane very well.

shape. Second, we use the lipid orientation to represent the normal vector, which is physically not exactly true due to the lipid tilt. Moreover, the lipid orientation fluctuates, and this can create a difference that can be as large as 10° for the cylinder, as discussed in Section 3.4.2. Thus we ultimately chose not to use this method and instead exclude the buckles with overhangs in our analysis. Fortunately, these buckles take only a very small part of the whole data, about 5% of all snapshots for

the largest $\gamma = 0.43$ in our simulation. But it still provides a new perspective on describing a shape for which it is hard to apply the analytical method.

2b. Fit Each Layer (Analytical Method)

Then let us look at the two analytical approximations: the Fourier expansion and the smoothing spline functions. Given the periodicity of the buckle, a Fourier expansion of its shape at first sight appears to be the more obvious choice, but it does have a disadvantage: even if no overhang occurs, large-strain buckles have large slopes near their inflection points, and capturing them requires high Fourier modes, which have a tendency to otherwise create too many small “wiggles” that are unphysical. Hence, we opted for smoothing splines, which result in overall more plausible smooth curves.

Briefly, a smoothing spline is defined as follows: given a set of N data points $\{x_i, y_i\}$ on some domain of interest $[a, b]$, a spline $\mathcal{S}(x)$ is called a *smoothing spline* if it minimizes the expression [24]

$$\chi_P^2 := P \sum_{i=1}^N [y_i - \mathcal{S}(x_i)]^2 + (1 - P) \int_a^b ds [\mathcal{S}''(x)]^2 . \quad (3.52)$$

The first term in Equation (3.52) penalizes the distance between the spline and the data, the second term penalizes the integrated curvature of the spline, thus making it smooth. The parameter P balances the relative weight of both conditions: in the limit $P \rightarrow 1$ the curvature penalty vanishes and we arrive at an *interpolating spline*; in the limit $P \rightarrow 0$ the spline becomes a straight line, namely, the linear least square approximation to the data. We choose P such that we get a sufficiently smooth function that has neither too many wiggles nor any remaining systematics in the residuals, by striking the following compromise: we aim to lower the χ_p^2 describing the least square fitting error for each layer, but at the same time keep P as small as possible, to avoid overfitting; this for instance means that if χ_p^2 first strongly decreases with P but then enters a plateau phase where it only weakly decreases, we pick the P value at the transition into the plateau phase (as shown in Figure 3.9). For each strain γ we list our choice of P in Tables 3.3 and 3.4. To calculate the smooth splines, we use numerical routines implemented in MATLAB[®], taking care to extend the buckle in both directions by a quarter-period (in order to avoid discontinuities in position or slope at the end points).

3. Finding the Middle Plane

We now have an analytical description of two well-defined planes in the leaflets, but we need a description of the bilayer’s *midplane*. To do this, we now translate each bead position used to define the upper/lower spline $\mathcal{S}_{\pm}(x)$ a distance δ along the local

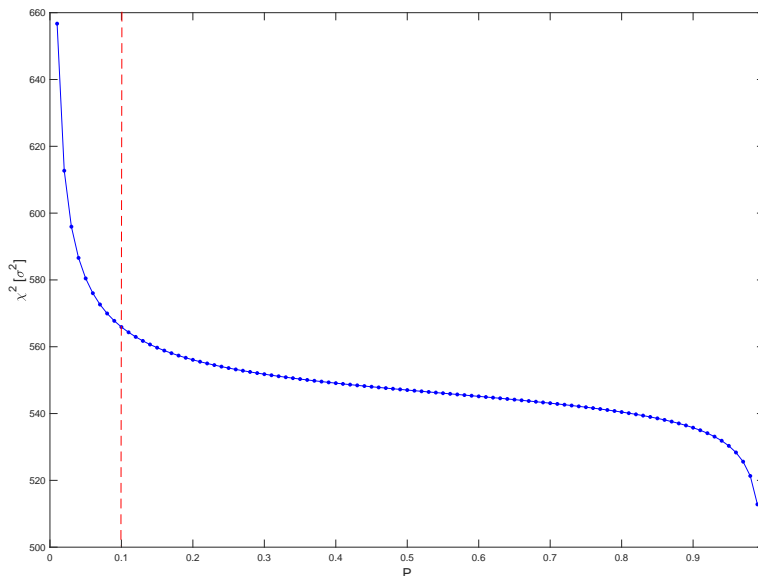


Figure 3.9: The χ^2 error changes with P value, showing an example for the Cooke model with $\gamma = 0.18$. We can see from $P = 0.1$, the error decreases only weakly, hence we choose $P = 0.1$ for this system.

normal (defined from \mathcal{S}_{\pm}) towards the midplane (*i. e.*, we translate the beads in the upper leaflet down and the ones in the lower leaflet up). We then fit the union of upper and lower shifted bead positions with one single spline $\mathcal{S}_m(x)$ that captures the midplane, and the χ^2 of that fit is a measure for how well the two surfaces have been shifted on top of each other. The minimum χ^2 identifies the optimum shift δ (as shown in Figure 3.10), and we use the corresponding fit as our best analytical expression for the bilayer’s midplane.

4. Cut the Buckle

The smooth curve describing the midplane permits us to calculate both arc length s and angle $\psi(s)$, so that we can perform cuts perpendicular to the membrane within which we subsequently count lipids. In particular, we choose two points on the fitting curve as the position for \underline{s} and \bar{s} , and by integrating or differentiating the midplane spline $\mathcal{S}_m(x)$, we obtain the arc length distance Δs and the angle difference $\Delta\psi$. The cutting planes themselves are identified by the local position and the cutting angle $\psi + \pi/2$. Lipids in either of the two leaflets are counted within the cut if a reference bead of that lipid falls within the sector between these two cutting planes. Interestingly, the choice of reference bead will cause a systematic trend in the results of z_0 .

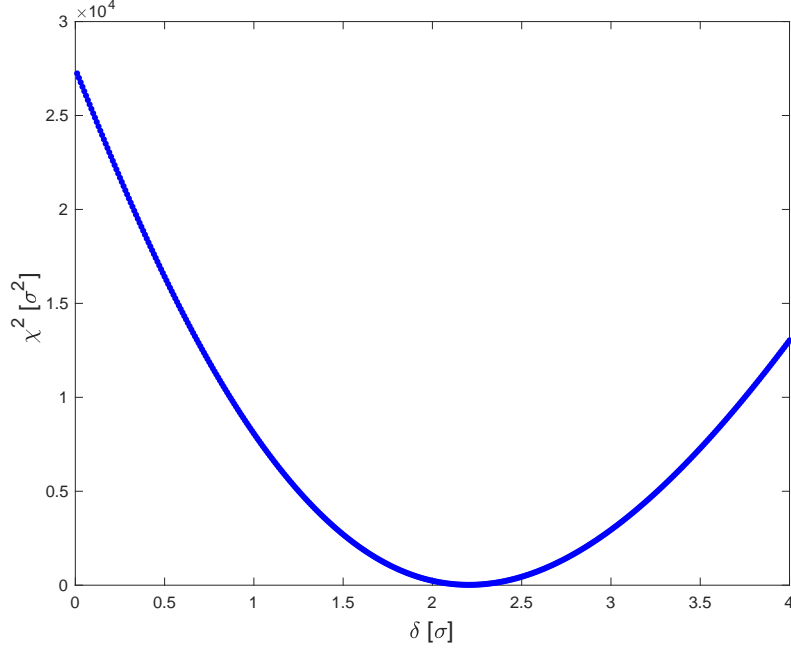


Figure 3.10: The χ^2 error changes with step size δ during midplane finding process, this is an example for Cooke model with $\gamma = 0.18$. Notice there is a minimum error corresponding to $\delta = 2.20\sigma$, and the lowest error is 18.84.

We will discuss which bead to choose, how it affects the result, and how to deal with it in the next subsection.

5. Lipid Counting and Self-consistent z_0 Calculation

When counting lipids, we need a criterion to decide if a lipid is inside the buckle segment we cut, because for some lipids near the starting or ending point it might happen that only part of the lipid is inside the segment. One solution can be to designate a reference bead, and from the result of z_0 in the simple configuration method, indicating that the pivotal plane lies at somewhere near the middle bead, choosing the middle bead for the Cooke model seems to be a reasonable choice. Then for each single snapshot, we can fix the starting point and scan the value of Δs from 0 to L . For each segment, we can count the lipid and get the value for M_- , $M_{\pm}^{(p)}$. Combining with the values for $\Delta\psi$ and s from the midplane fit, a pair of $\{x_p, y_p\}$ can be calculated from Equation (3.42). According to Equation (3.41), these $\{x_p, y_p\}$ data points should lie on a line going through the origin, which they indeed do (as shown in Figure 3.11). The slope of this line is the value for z_0 . An error can be estimated for z_0 from all snapshots in the same simulation after equilibration. Again, we will

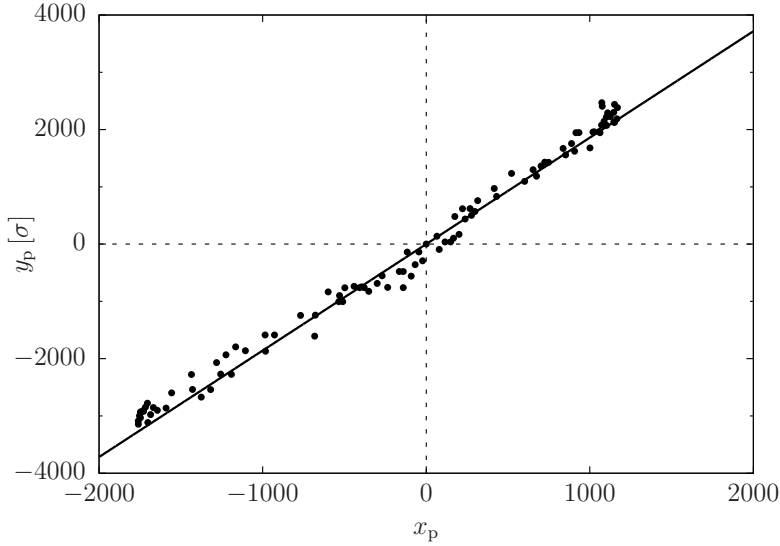


Figure 3.11: Typical example of a plot of the pairs $\{x_p, y_p\}$ from Equation (3.42), which according to Equation (3.41) are expected to lie on a line through the origin. This particular result is taken for one of the snapshots of a Cooke buckle at $\gamma = 0.43$, the largest strain we used.

use the blocking method to get an error of the mean for correlated data instead of using the standard deviation.

What about other choices of reference bead? Will they give the same result? Curiously, for a given strain γ , the value of z_0 is not independent from, but slightly related to the choice of reference bead. Figure 3.12 shows the Cooke model case of $\gamma = 0.25$, and we can see that the central bead leads to a z_0 only slightly larger than that coming from the inner tail bead. In contrast, the z_0 -value derived from the head bead is significantly smaller, and more so for large strains. Since the most natural reference point to choose would be a bead that lies exactly at the pivotal plane (which is almost but not quite true for the middle bead), we linearly extrapolate the z_0 position from the two tail beads

$$z_0(\xi) = z_{0,0} + z_{0,1} \xi , \quad (3.53)$$

where ξ is the position of a bead from the bilayer's midplane. A corrected value for z_0 can now be determined by intersecting this extrapolation with the line $z_0 = \xi$, leading to the self-consistent result

$$z_0 = \frac{z_{0,0}}{1 - z_{0,1}} . \quad (3.54)$$

Resampling the z_0 values for the two tail beads—and hence the extrapolation line—

also gives the error. The procedure is illustrated in Figure 3.12 and the results are summarized in Table 3.3.

One thing worth mentioning is that we get the value for ξ from a stress free flat membrane in the equilibrium state. The zero stress is reached by adjusting the box length and after fitting the middle plane to a smooth curve, the averaged bead distance to the middle plane is used as $\langle \xi \rangle$.

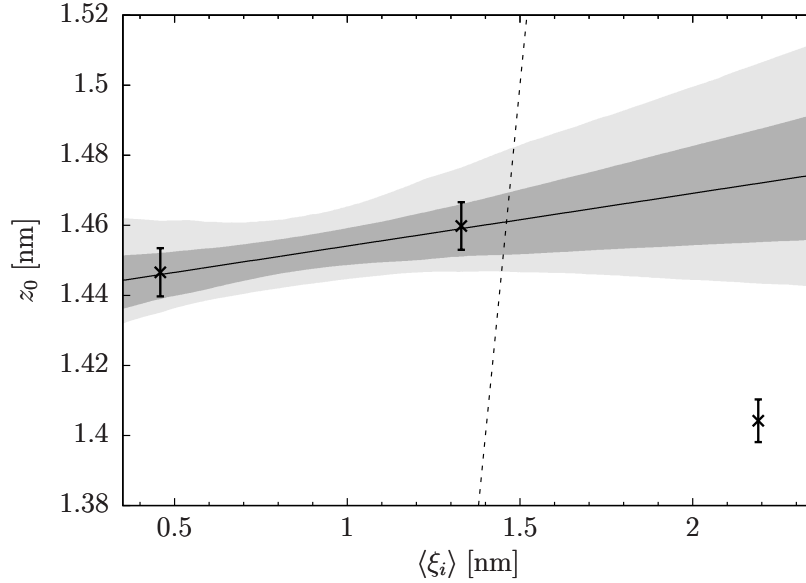


Figure 3.12: Pivotal plane position z_0 derived (via buckling at $\gamma = 0.25$) from each of the three beads of a Cooke lipid as the reference, plotted against these beads' average distance ξ from the bilayer's midplane. The shaded regions are the 67% and 95% confidence bands of the linear extrapolation.

To summarize, we have use the hierarchical clustering method to label each individual layer. And for each layer, we describe its shape using a smoothing spline fit. Then according to the normal vector based on this fitting curve, we translate the lipids towards the midplane and in turn reach a spline fitting function to describe the midplane, or the whole buckle. This provides geometrical information, such as arc length s and angle ψ , for a segment cut from the buckle, together with a reference bead counting strategy, allows us to retrieve many values of $\{x_p, y_p\}$ pairs, as well as the z_0 values from Equation (3.42). But since the pivotal plane position depends on the reference bead choice, we need to apply a self-consistent method to get the final z_0 value for the system with a certain strain value.

3.5.2 Buckle Results for Cooke Model

The Average Squared Curvature $\langle K^2 \rangle$ and the Isotropic Tension Σ

From the last section, we have a value for z_0 with an error bar for every strain γ . But before we analyze the results and compare them with the simple configurations, we need to get the value for average squared curvature $\langle K^2 \rangle$ and isotropic tension Σ .

The expression of average squared curvature has been derived in Section 3.3.2, when we proved that the Poisson effect in Equation (3.37) can be ignored. And the expression for $\langle K^2 \rangle$ is Equation (3.45).

The isotropic tension Σ for the buckle is negative since it is under compression, compared to the cylinder case, where the membrane is pulled in the z -direction. The surface tension Σ and the buckling stress f_x are related by $\Sigma = -f_x \cos \psi_i$, where ψ_i is the angle which the buckle makes at its inflection point [57]. This relation can best be understood as a balance of horizontal stresses [27].

We have derived f_x and m as a series expansion in γ , as shown in Equation (3.32). And from the definition: $m = \sin^2(\psi_i/2)$, we can write down $\cos \psi_i = 1 - 2m$ as a function of γ as well. Thus, Σ can be written as:

$$\Sigma = -\kappa \left(\frac{2\pi}{L} \right)^2 \left(1 - \frac{3}{2}\gamma - \frac{15}{32}\gamma^2 - \frac{27}{128}\gamma^3 - \dots \right). \quad (3.55)$$

The results of $\langle K^2 \rangle$ and Σ for every system are listed in Table 3.3.

Buckle Results and Comparison with Simple Configuration

For the Cooke model buckled membranes, the full results, including the system strain γ , the average squared curvature $\langle K^2 \rangle$, the isotropic tension Σ , the fitting parameter P and finally the pivotal plane position z_0 , are listed in Table 3.3. These results are also plotted in Figures 3.13 and 3.14.

The final result is averaged at $z_0 = 1.4685(32)\sigma$, and does not show any dependence on any parameters, except for a systematic decline in z_0 at large strain. We contribute this trend to the steep region of membranes introduced by large curvature. Even though we exclude the buckles with overhangs before our analysis, as mentioned in last section, these buckles, which are overhang free yet containing step portions, will cause difficulties for the shape analysis, which may in turn reflect in a depression of the inferred value of z_0 .

γ	$\langle K^2 \rangle \times 10^3 [\sigma^{-2}]$	$\Sigma \times 10^2 [\epsilon/\sigma^2]$	P	$z_0 [\sigma]$
0.04	0.716	-11.72	0.03	1.477(17)
0.06	1.080	-11.33	0.03	1.472(29)
0.07	1.263	-11.14	0.03	1.470(13)
0.09	1.632	-10.74	0.03	1.467(15)
0.10	1.818	-10.54	0.03	1.489(15)
0.12	2.193	-10.14	0.10	1.440(13)
0.14	2.573	-9.73	0.10	1.467(16)
0.18	3.344	-8.90	0.10	1.492(11)
0.25	4.736	-7.38	0.30	1.4768(80)
0.31	5.977	-6.02	0.30	1.4722(81)
0.37	7.264	-4.59	0.50	1.4642(61)
0.43	8.603	-3.08	0.50	1.4606(79)
				1.4685(32)

Table 3.3: Summary of Cooke model simulations in buckling geometry; γ is the buckling strain, $\langle K^2 \rangle$ the mean squared curvature (from Equation (3.45)), Σ the isotropic tension (from Equation (3.55)), P the smooth spline weighting in Equation (3.52), and z_0 the self-consistent position of the pivotal plane from Equation (3.54). Common parameters are $N_{\text{lipids}} = 1344$, $L = 66.75\sigma$, and $L_y = 12\sigma$. The buckles were simulated for a total time of $5 \times 10^4 \tau$, resulting in 2490 configurations that were analyzed. We used the trajectories created in Ref. [57].

3.5.3 Compare across all configuration

Now we have the results for all three geometries, together with two proper axes for comparison: $\langle K^2 \rangle$ and Σ . All data are plotted with 67% and 95% confidence bands in Figure 3.13 and Figure 3.14. From the figures, the cylinder and sphere results agree with each other very well, while there remains a small difference between the buckle and the simple configurations. Even though this difference is statistically significant, it is only about 0.8%. One may be tempted to blame the buckle systems with large strains and high curvature as being responsible for this gap. However, tentatively eliminating the highest four strains will move the pivotal plane only up to $z_0 = 1.4724(56)\sigma$, still within error bar of the old value. Hence we still plot them together with the whole data set, since this elimination will not explain the difference. At this moment, the origin of this small discrepancy is still unclear, but we stress that we only notice it because our protocols are so very precise.

Except for this less than 1% difference, we have shown that the result from the

buckle strategy is consistent with the one from the simple configuration strategy, and both of them are totally independent from each other. This validates the buckling method, and we can apply it to more complicated models: the MARTINI model and the Berger model.

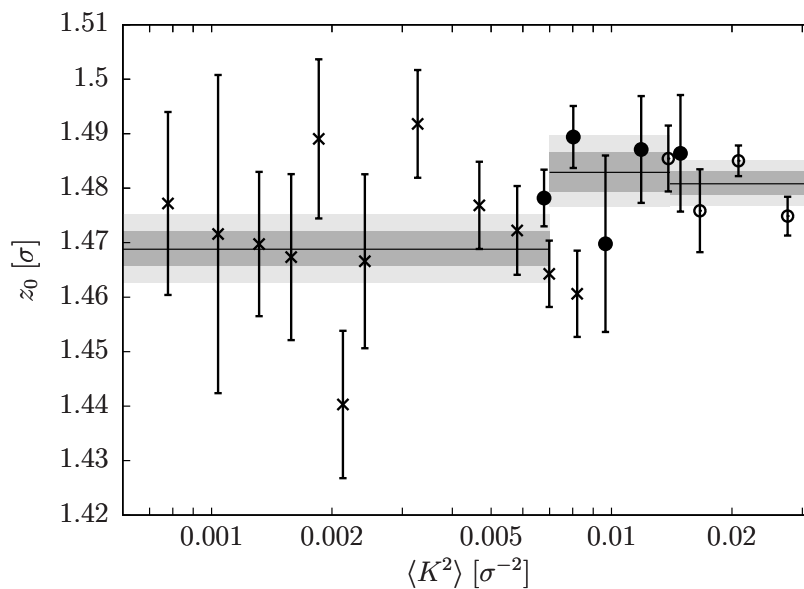


Figure 3.13: Pivotal plane position z_0 plotted against mean squared curvature $\langle K^2 \rangle$ for three different geometries: cylinders (filled circles), spheres (open circles), and buckles (crosses). The shaded regions are the 67% and 95% confidence bands.

3.5.4 Results for MARTINI Model

Self-consistent Method Determining z_0

For the MARTINI model, as mentioned in Section 3.3, the cylinder and sphere protocol are not applicable, and only the buckle configuration is investigated. The main strategy is identical to the one employed for the Cooke model. A list of all MARTINI model simulations can be found in Table 3.4.

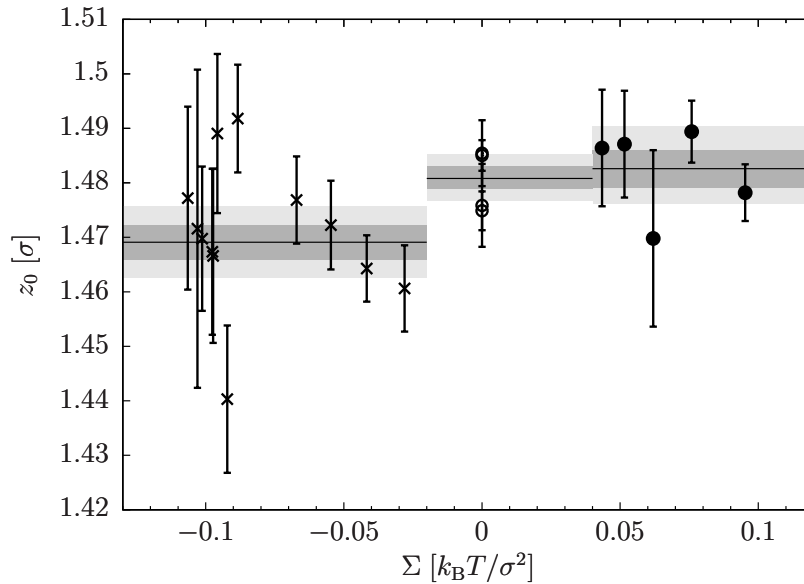


Figure 3.14: Pivotal plane position z_0 plotted against isotropic surface tension Σ for three different geometries: cylinders (filled circles), spheres (open circles), and buckles (crosses). The shaded regions are the 67% and 95% confidence bands.

γ	$\langle K^2 \rangle \times 10^2$ [nm ⁻²]	Σ [mN/m]	P	z_0 [nm]
0.05	0.183	-2.00	0.03	0.8408(37)
0.10	0.371	-1.83	0.03	0.8520(35)
0.15	0.563	-1.66	0.10	0.8543(17)
0.20	0.762	-1.47	0.10	0.8543(24)
0.25	0.966	-1.28	0.30	0.8543(13)
0.30	1.176	-1.09	0.30	0.8543(24)
0.35	1.392	-0.88	0.50	0.8543(12)
0.40	1.616	-0.67	0.50	0.8543(15)
0.45	1.847	-0.44	0.50	0.8543(18)

Table 3.4: Summary of MARTINI DMPC model simulations in buckling geometry; variables are the same as in Table 3.3. Common parameters are $N_{\text{lipids}} = 1120$, $L = 46.75$ nm, and $L_y = 7.1$ nm. The buckles were simulated for a total time of 10^3 ns after equilibration, resulting in 391 configurations that were analyzed. We used the trajectories created in Ref. [57].

The biggest difference in the MARTINI analysis is that there is no obvious good choice for the reference bead. Even though some people have suggested the interface

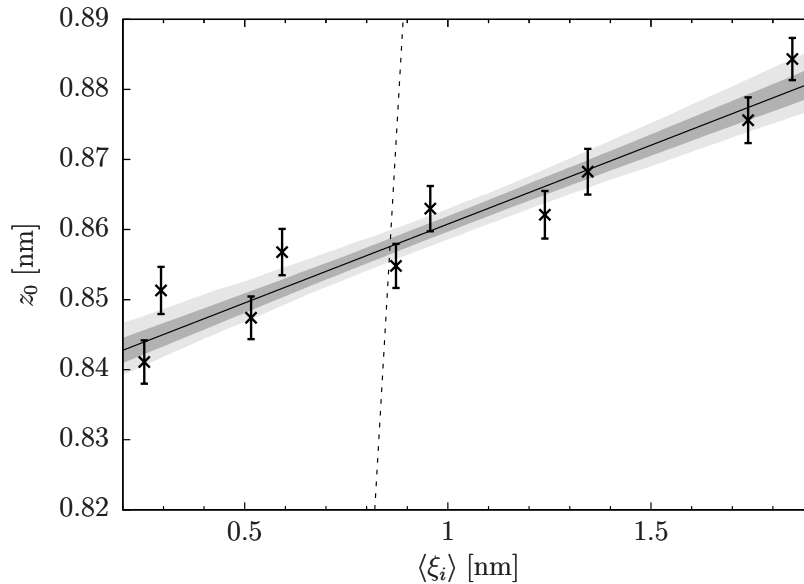


Figure 3.15: Plot of the pivotal plane position z_0 using each of the 10 beads of a MARTINI DMPC molecule as the reference, plotted against these beads’ average distance $\langle \xi_i \rangle$ from the bilayer’s midplane, and extracted from buckles with $\gamma = 0.35$. The $z_0(\xi)$ relation is well described by Equation (3.53), as the fit—together with its 67% and 95% confidence bands—indicates. The intersection with the dashed line $z_0 = \langle \xi_i \rangle$ gives the self-consistently determined value of the pivotal plane position.

of the hydrophobic/hydrophilic region as an estimation of where the pivotal plane is [115], the MARTINI DMPC lipid might have a different location because of its coarse-grained nature. Just as in the Cooke model case, we again deal with this by a self-consistent strategy. In analogy to Figure 3.12, we again plot the position of z_0 , inferred by using each of the 10 beads of a MARTINI DMPC molecule as the reference, against the average distance $\langle \xi_i \rangle$ which bead i has with respect to the bilayer’s midplane—see Figure 3.15. Recall that for the Cooke model, the z_0 generated by the head bead is significantly lower than that of the other two beads. In the MARTINI model plot, we find a *linear* dependence of z_0 on the $\langle \xi_i \rangle$. Hence we fit it using Equation (3.53) and again extract the self-consistent z_0 value through Equation (3.54). The error bar of the final z_0 result comes from the resampled confidence band and is smaller than each individual bead’s error. It also seems that the z_0 values inferred from the *sn1*-chain are systematically lower by about 0.01 nm than those from the *sn2*-chain, which could be a result of the different tilt situation of the two chains.

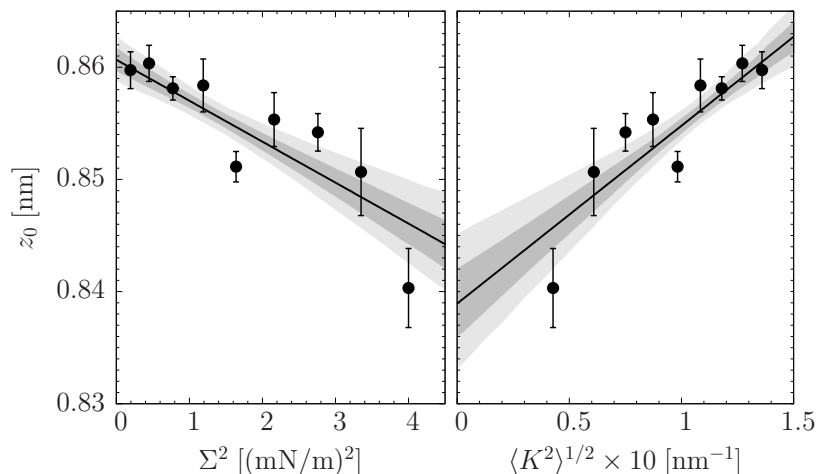


Figure 3.16: Pivotal plane position z_0 for all MARTINI DMPC simulations, plotted alternatively against the square of the surface tension (left) and the root mean squared buckle curvature (right). The shaded regions are the 67% and 95% confidence bands.

Zero tension vs. Zero curvature

Without the simple configuration results to compare with, we can still plot the pivotal plane as a function of both Σ^2 and $\langle K^2 \rangle^{1/2}$ as shown in Figure 3.16. Remember the Cooke case plots, in which except for the large strain systems, we can not see any dependence of the pivotal plane results on mean squared curvature or tension. And we have attributed the decline at large strain to the shape undulations. The MARTINI case, however, presents a small but very systematic dependence of z_0 on the system: as the curvature increases, or the tension decreases, the position of the pivotal plane moves outward. The shape undulation is less of a factor since our MARTINI buckle is about 30% smaller in length and 2.3 times higher in rigidity [57], which makes it a harder and shorter membrane than the Cooke one.

This systematic decrease is only about 1.5% of the average value between the largest and the smallest measured value, but whether one can exploit this trend and get an even more accurate value by extrapolating remains an interesting question. Obviously two possible and both plausible estimation are available: the zero tension limit and the zero curvature limit. The latter possesses the same *geometry* as the flat reference state, but the former captures the property of being *free of isotropic stresses*. From Figure 3.16, the extrapolating results of these two limits are:

$$\text{zero tension: } z_0 = 0.8607(10) \text{ nm} , \quad (3.56a)$$

$$\text{zero curvature: } z_0 = 0.8389(30) \text{ nm} . \quad (3.56b)$$

Unfortunately, no good reasons exist for preferring one value over the other. The best we can say is that this is more of a personal choice. If one is less worried about high curvature corrections, the zero-tension limit will appear more attractive, while the zero-curvature limit appears preferable if one considers the net compression (about 2 mN/m for the weakest buckle) not much of a problem. At this point, it seems appropriate not to prematurely take sides and instead state, in the absence of a theoretical explanation for the γ -dependence, that z_0 is within this range, and give the answer as $z_0 = 0.850(11)$ nm. This position is closest to the third coarse-grained tail bead on the *sn1*-chain, which is about 0.4 nm away from the *sn1* glycerol bead.

But the question remains: why do we have this dependence on curvature or compression? We have previously shown that the pivotal plane $z(K)$ is a function of local curvature K in Equation (3.12), and this plot also shows a curvature related dependence. But all data points in Figure 3.16 quote the z_0 values for the flat membrane. This indicates a curvature dependence of the flat membrane value. Another possibility is related to the Poisson term we dropped in Equation (3.37), which contains the mean squared curvature, but this is impossible for the following reason: the term, if not dropped, will still multiply $M_-^{(p)}$. For the MARTINI simulation, the value of $M_-^{(p)}$, however, is zero, since the lipids are very hard to either flip-flop or escape from the bilayer. Nevertheless, the z_0 value also depends on the strain, and we might conjecture that it is an effect of membrane compression instead of a curvature influence. And if this is the case, the zero tension limit looks like a more appropriate choice.

3.5.5 Results for Berger Model

Self consistent method determining z_0

Having determined the pivotal plane position z_0 both for the Cooke model and for MARTINI-DMPC, let us now a similar analysis for the Berger model. The full results are listed in the Table 3.5 below.

γ	$\langle K^2 \rangle \times 10^2$ [nm ⁻²]	Σ [mN/m]	P	z_0 [nm]
0.12	0.636	-2.13	0.10	1.3057(67)
0.14	0.746	-2.05	0.10	1.3155(51)
0.16	0.857	-1.97	0.10	1.3372(98)
0.24	1.314	-1.61	0.30	1.3417(67)
0.27	1.491	-1.47	0.30	1.3149(58)
0.30	1.670	-1.32	0.50	1.3218(36)
0.33	1.853	-1.17	0.50	1.3189(39)
				1.3225(44)

Table 3.5: Summary of Berger DMPC model simulations in buckling geometry; variables are the same as in Table 3.3 and Table 3.4. Common parameters are $N_{\text{lipids}} = 934$, $L = 39.20$ nm, and $L_y = 7.1$ nm. The buckles were simulated for a total time of 100 ns after equilibration, resulting in 1000 configurations that were analyzed. We used the trajectories created in Ref. [57].

Again, no obvious choice exists for the reference bead of the Berger case, and we will plot one more time the value of z_0 against the average bead position $\langle \xi_i \rangle$ in Figure 3.17. Since DMPC in the Berger force field contains 46 heavy atoms per lipid, this gives 46 points in the plot. Compared with the MARTINI plot (Figure 3.15), instead of falling onto a straight line, the tail region shows a linear relation with fairly good accuracy, while beyond the glycerol backbone the slope noticeably decreases and ultimately even changes sign.

Thus, a self-consistent determination of z_0 will not use all beads but only the tail beads, and by intersecting the measured data with the line $z_0 = \langle \xi_i \rangle$, the pivotal plane is found at the end of the linear region, close to the glycerol backbone. A more careful analysis, averaging over all buckles and all values of γ , gives $z_0 = 1.3225(44)$ nm, placing the pivotal plane roughly at the carbonyl carbon in the *sn1* chain. The results are plotted against isotropic tension square Σ and averaged square curvature $\langle K^2 \rangle$ in Figure 3.18.

Two comments will be made here. Firstly, there is a noticeably nonlinear shape of $z_0(\xi)$ in the head region, which is different from the case of MARTINI DMPC. The existence of this non-linear region has further interesting physical implications for the lipid tilt, which we will discuss in more detail in the next chapter.

Secondly, recall that in the analysis of the MARTINI results we found a linear dependence of z_0 on both Σ and $\langle K^2 \rangle$, and I concluded that whether a zero curvature

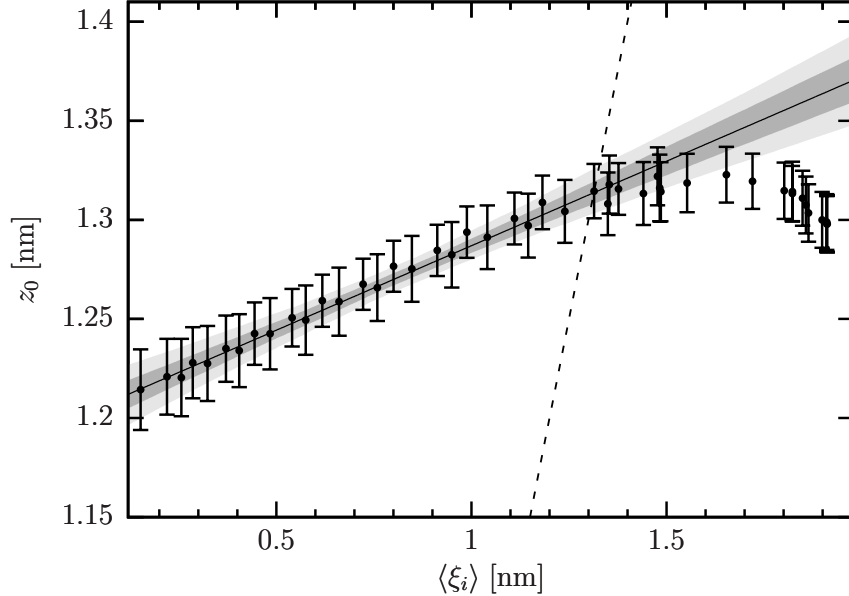


Figure 3.17: Position of the pivotal plane z_0 for the Berger DMPC model, plotted against the average position $\langle \xi_i \rangle$ of the i^{th} reference atom in the lipid, for the strain $\gamma = 0.24$. The solid line is a linear fit to the 28 carbon atoms in the two myristoyl tails, flanked by the 1σ and 2σ confidence bands. The dashed line is the identity $z_0 = \langle \xi_i \rangle$, which intersects the data at the self-consistently determined value of z_0 .

limit or a zero tension limit is taken is a matter of personal choice in terms of the appropriate value for z_0 . But in the Berger atomistic lipid simulation, this trend no longer exists. But then, the goodness of fit for the Berger case is not very good, and there is a hint of a slight increase for the low curvature case. The reason for this increase is currently unknown and since the value reaches a plateau under high curvature/low tension conditions, we still fit the data points with a constant, and get the z_0 value from this.

3.6 Discussion of the Results

3.6.1 Bare numbers and a comparison with experiment

A first look at the bare numbers

To begin with, it is important to realize how precise the results for z_0 are. Either method can pinpoint the pivotal plane's position with a percent-level error of the mean. This in retrospect justifies our consideration of several high order terms, say

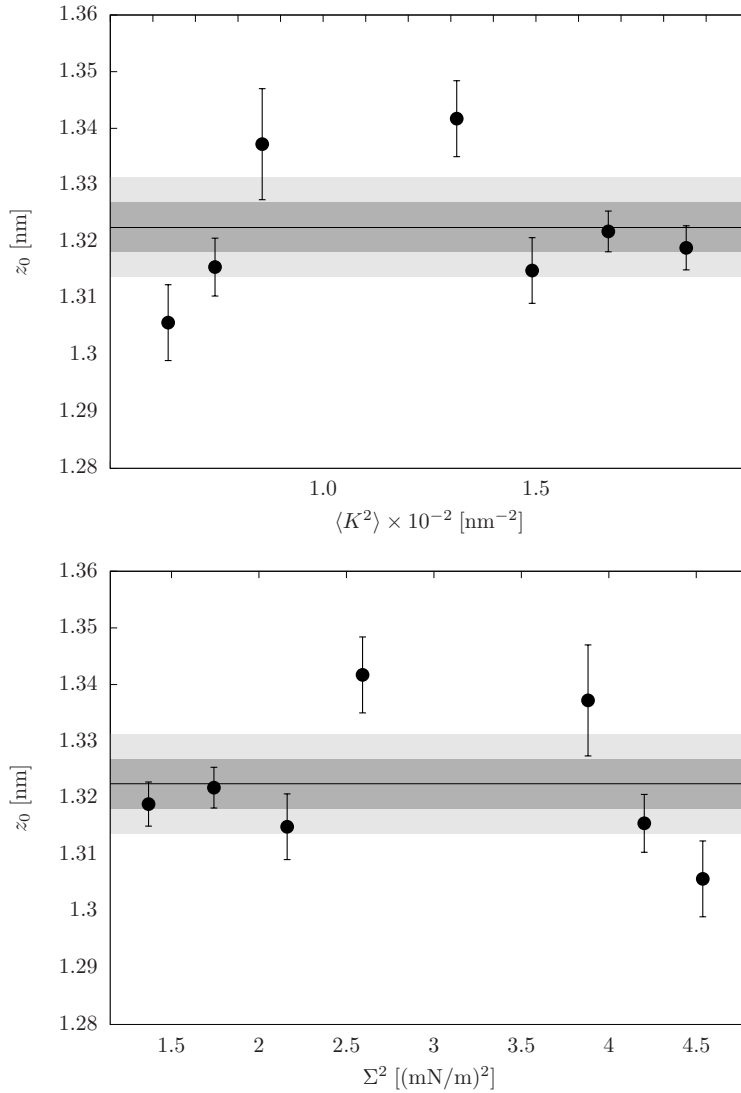


Figure 3.18: Pivotal plane position z_0 for all Berger DMPC simulations, plotted alternatively against the root mean squared buckle curvature (top) and the square of the surface tension (bottom). The shaded regions are the 67% and 95% confidence bands.

the Poisson term in Equation (3.12), since it is not obvious what term is negligible at the theoretical framework building stage. And what is more, a result with higher precision may offer us more insight into the physical properties of the membrane, as we will see in the next chapter.

Checking the pivotal plane position given by our analysis and comparing with existing experimental results is a good starting point. For the generic Cooke model,

there are of course no direct predictions to compare with. Instead, we introduce a new parameter: the dimensionless ratio between pivotal plane and lipid length. In particular, we take the average distance ξ_h between head bead and midplane as the lipid length, and here we have $\langle \xi_h \rangle = 2.19 \sigma$. Thus, the ratio is $z_0 / \langle \xi_h \rangle \approx 0.678$. This is remarkably close to expectation: for real lipids, the position of the pivotal plane is estimated to be near the hydrophilic/hydrophobic interface, about two thirds of the length of a lipid [115].

For the MARTINI membrane, we take the CG phosphate bead, in analogy to the head bead in the Cooke case, since it is a simple proxy for the Luzzati plane, or the interface between water and lipid (as mentioned in Section 3.2.2). This position is $\langle \xi_{Ph} \rangle \approx 1.739 \text{ nm}$, and the ratio in turn is $z_0 / \langle \xi_{Ph} \rangle \approx 0.491$, which is substantially smaller than the $\frac{2}{3}$ rule of thumb.

The result for the Berger model is $z_{0, \text{Berger}} = 1.3225(44) \text{ nm}$, which is noticeably larger than the MARTINI-derived value $z_{0, \text{MARTINI}} = 0.850(11) \text{ nm}$. This value agrees with the hydrocarbon core thickness measured in experiment, which in Nagle *et al.*'s paper [98], is 1.31 nm. Consider the lipid length difference and compare the ratio instead: $\langle \xi_{Ph} \rangle = 1.80 \text{ nm}$ for Berger.¹ This leads to $z_0 / \langle \xi_{Ph} \rangle = 0.73$ for Berger, substantially higher up towards the head region than MARTINI's value 0.49. What is more, this ratio is also closer to the $\frac{2}{3}$ rule of thumb.

We keep mentioning this empirical rule, but considering that this rule is derived from a highly curved configuration experiment (namely, an inverse hexagonal phase), a closer examination, accounting for such high curvature effects, seems warranted.

Experimental Results from H_{II} phase

Let us look at the experiment by Chen and Rand [16], who have measured the pivotal plane position for dioleoylphosphatidylethanolamine (DOPE) in the inverse hexagonal H_{II} phase—pure, as well as with the addition of small amounts (16% by weight) of either decane or tetradecane to fill in the interstitial threefold symmetry defects. Since both the pivotal plane position, denoted as “ δ_{hc} ” in their paper, and the bilayer membrane thickness, denoted as “ d_l ”, are measured under highly curved condition, we need to translate them back to the flat membrane situation in order to compare with our results.

Firstly, their values for the pivotal plane are 0.87(5) nm for the pure case, and

¹Our value of the width of a flat leaflet agrees with experimental results of Nagle et al. [98], who measured the headgroup peak-peak value D_{HH} , or phosphate to phosphate distance, which is 3.6 nm for DMPC, resulting of course in the value 1.8 nm for monolayers.

1.06(5) nm and 1.09(5) nm for the decane and tetradecane case, respectively. All these numbers are what we called $z(K)$, and to back out the flat reference value z_0 , we need to invert Equation (3.12); up to quadratic order this leads to

$$z_0 = z(K) \left[1 - \frac{1}{2} x K z(K) + \mathcal{O}(z(K)^2) \right] . \quad (3.57)$$

The curvature K is that of the pivotal plane, for which Chen and Rand’s data give $K = 1/R_p \approx -1/2.7(1)$ nm (in the decane case). Notice the negative sign: the monolayer curvature of the *inverse* hexagonal phase is *negative*, and so $Kz(K) \approx -0.39$.

Unfortunately we also need the Poisson ratio to translate the results back to the flat reference case. If $\nu = 0$, no shift happens, while in the incompressible limit $\nu = \frac{1}{2}$ (and thus $x = 1$) the correction factor in Equation (3.57) becomes $1 - \frac{1}{2} \times (-0.39) \approx 1.20$, showing that in this case z_0 is about 20% bigger than δ_{hc} , or about 1.27 nm and 1.31 nm for the decane and tetradecane measurements, respectively. These are substantial curvature corrections, and they shift the pivotal plane further up towards the head group region. This direction is expected, for unbending a highly curved H_{II} monolayer will push the lipid tails closer together and hence will make them stretch out even more.

Secondly, for the bilayer width, Chen and Rand identify it as the distance between apposing Luzzati planes ($d_l = 3.39$ nm for the decane case), and so they also get the distance between the pivotal plane and the Luzzati plane—in their notation: $\delta_{pol} = 0.64$ nm for the decane case. Extending above’s reasoning, we can calculate the width $d_{l,0}$ of the uncurved bilayer:

$$d_{l,0} = 2\delta_{hc} \left[1 + \frac{1}{2} x |K| \delta_{hc} \right] + 2\delta_{pol} \left[1 - \frac{1}{2} x |K| \delta_{pol} \right] , \quad (3.58)$$

which in the incompressible limit gives $d_{l,0} \approx 3.67$ nm, about 8% wider than in the H_{II} phase. The fraction which the pivotal plane takes of the monolayer width is hence $z_0/(d_{l,0}/2) = 0.69$, slightly larger than the $\frac{2}{3}$ rule of thumb and 10% larger than the uncorrected result $\delta_{hc}/(d_l/2) = 0.63$. Repeating the analysis for the tetradecane case gives the very similar result $z_0/(d_{l,0}/2) = 0.68$, while the pure case leads to the substantially smaller value $z_0/(d_{l,0}/2) = 0.61$.

So far, we have found that the ratio for the *flat* membrane is between 0.61 and 0.69, but our ratio from analyzing our MARTINI DMPC buckling simulations is 0.49. This is significantly smaller. This discrepancy could be attributed to the difference of lipids: DOPE used in the experiment has the longer unsaturated oleoyl chains (18 carbons, one cis double bond at position 9) and a smaller PE head group. On the other hand, the size difference has already been accounted for by taking the ratio between z_0 and lipid length. One might also wonder whether it is because of spontaneous curvature, but we can exclude this possibility later in Section 3.6.4. Among all

the other possible explanations for this small ratio, some inherent deficiency of the coarse-grained model starts to become very likely.

Being skeptical about the CG models

From the investigation above, we know that both general expectation and experiment suggest that z_0 lies somewhere about $\frac{2}{3}$ up towards the head group region.² In other words, the pivotal plane locates just barely below the glycerol backbone region, where the lipid tails get joined to the more rigid head group region [115]. The question arises for the MARTINI model: why would a coarse-grained but still fairly well resolved lipid model get that number wrong?

The most straightforward possible reason can be the information lost during the coarse-graining process, say the lipid tails' coarse-grained representation. The in principle curvature-dependent entropy embodied in the tail statistics is replaced by a curvature independent energy of a CG interaction potential. This reduces the extent to which tails can respond to curvature changes. This lack of response in turn pulls the pivotal plane closer to the leaflet's midplane, since in the extreme case, which is the elastically homogeneous material, one would expect the pivotal plane to be in the middle of the lipid leaflet. If this is really what causes the discrepancy between the MARTINI result and the general prediction, an essentially atomistically resolved Berger force field should not suffer from this problem and instead place the pivotal plane closer to the glycerol backbone. And this is indeed what we find.

While it is dangerous to read too much into the outcome of a single investigation, the underlying CG approximation is well known and uncontested: CG potentials invariably inherit aspects of the state point at which they are constructed or for which they have been developed. Lipid models are generally optimized to reproduce the L_α phase of membranes, not highly curved lipid leaflets. Notice, however, that MARTINI is *not* a structurally coarse-grained model, and so it should suffer less from any all-too-eager attempt to optimize the structural aspects of a flat bilayer. And still, its very construction (equal bead size all the way down the tail) is at least inspired by the geometry of a bilayer phase. Had the developers aimed at surfactants that

²Besides the 2/3 rule of thumb, other means of comparison would also be possible. For instance, one could compare the pivotal plane position not with the width of a monolayer all the way up to the phosphate bead, but instead only up to the glycerol backbone, in effect comparing it to the width of the hydrocarbon region (John Nagle, personal communication). This would lead to an alternative weighting when comparing lipids which differ in their hydrocarbon tail length, but would ignore the structure of the head group and its impact on overall elastic pliability of the entire leaflet. Ultimately, whether a universally good point of comparison exists that might even be used as a proxy for the pivotal plane position for cases that have not yet been measured, remains to be seen—for instance by determining z_0 for a wider set of lipids.

assemble into spherical micelles, a more “tapered” design might have suggested itself. The surprising lesson is that such subtle aspects in an otherwise fairly well-resolved model can show up so noticeably even in relatively benignly deformed bilayers.

We hasten to add that this does of course *not* invalidate the use of CG models to study membrane phenomena that involve membrane bending. The curvature modulus could be well reproduced, and this is often all that matters at larger scales. But we believe that CG studies which explicitly aim to *explain* the value of the bending modulus or its dependence on lipid architecture—say, how it depends on tail length and saturation—ought to be viewed with some skepticism. If the chain conformations in curved coarse-grained membranes do not—and *can* not—capture the physics of free fatty acid tails, and hence end up bending the bilayer around a noticeably shifted reference surface, the relative contributions of head- and tail-regions to the overall rigidity are misbalanced, rendering claims about the relation between bending modulus and specific tail properties somewhat suspect.

3.6.2 Calculating moments of the lateral stress profile

The Lateral Stress Profile for Monolayer and Bilayer

As mentioned in Section 3.1.1, the pivotal plane serves as the bridge between several monolayer and bilayer observables. Let us look at one typical example, the trans-bilayer stress profile. If the membrane spans the xy -plane, such that its normal vector aligns with the z -direction, the pressure tensor Π_{ij} is diagonal in the xyz -coordinate system. We may then define the trans-bilayer stress profile as

$$\Sigma_0(\xi) = \langle \Pi_{zz} \rangle - \frac{1}{2} \langle \Pi_{xx}(\xi) + \Pi_{yy}(\xi) \rangle , \quad (3.59)$$

where ξ measures the position along the normal direction of the membrane, such that $\xi = 0$ corresponds to the bilayer midplane. The perpendicular component $\langle \Pi_{zz} \rangle$ does not depend on ξ for reasons of mechanical stability and coincides with the bulk pressure. Figure 3.19 and 3.20 shows this stress profile for the Cooke and MARTINI model, respectively. For reasons of symmetry, the plots can restrict to positive ξ -values.

A well-known result from continuum theory relates moments of this stress profile to various mono- and bilayer observables. If we define the monolayer moments as

$$\mathcal{M}_m^{(n)} := \int_0^w d\xi \Sigma_0(\xi) (\xi - z_0)^n , \quad (3.60)$$

where the integral spans over the entire monolayer-support of $\Sigma_0(\xi)$, then [41, 49, 50,

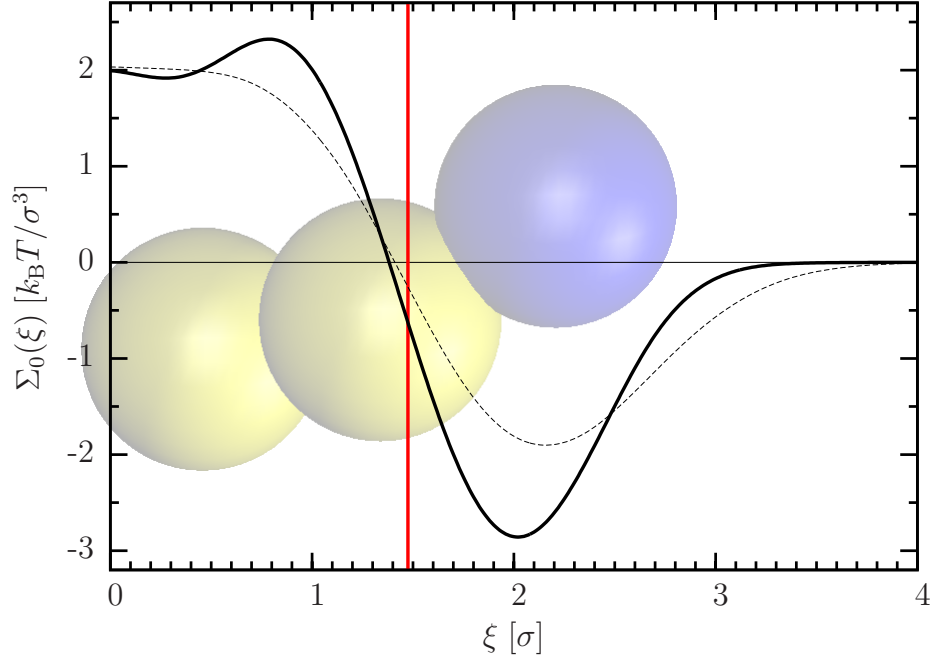


Figure 3.19: Stress profile $\Sigma_0(\xi)$ from Equation (3.59) for the Cooke model. The bold solid curve was computed with a system of 128 lipids, the fine dashed curve comes from Ref. [57] and is based on a system of 1000 lipids. The stress profile for the bigger membrane is smoothed by thermal shape undulations; it is largely identical to a convolution of the sharper profile with a Gaussian of width 0.4σ . The red vertical line denotes the position of the pivotal plane. For reference purposes, the faded lipid model in the background has all beads located at their average distance form the bilayer's midplane.

81, 83, 84, 103, 106, 104, 105, 107, 108, 121, 136, 138]

$$\mathcal{M}_m^{(0)} = \frac{1}{2}\Sigma, \quad (3.61a)$$

$$\mathcal{M}_m^{(1)} = -K_{m0}\kappa_m, \quad (3.61b)$$

$$\mathcal{M}_m^{(2)} = \bar{\kappa}_m. \quad (3.61c)$$

We remind the reader that the monolayer observables κ_m , K_{m0} and $\bar{\kappa}_m$ are to be understood as those for which z_0 is the Gibbs dividing surface [63, 12].

If we instead define the integral in Equation (3.60) over the bilayer, and with the midplane as the reference point,

$$\mathcal{M}_b^{(n)} := \int_{-w}^w d\xi \Sigma_0(\xi) \xi^n, \quad (3.62)$$

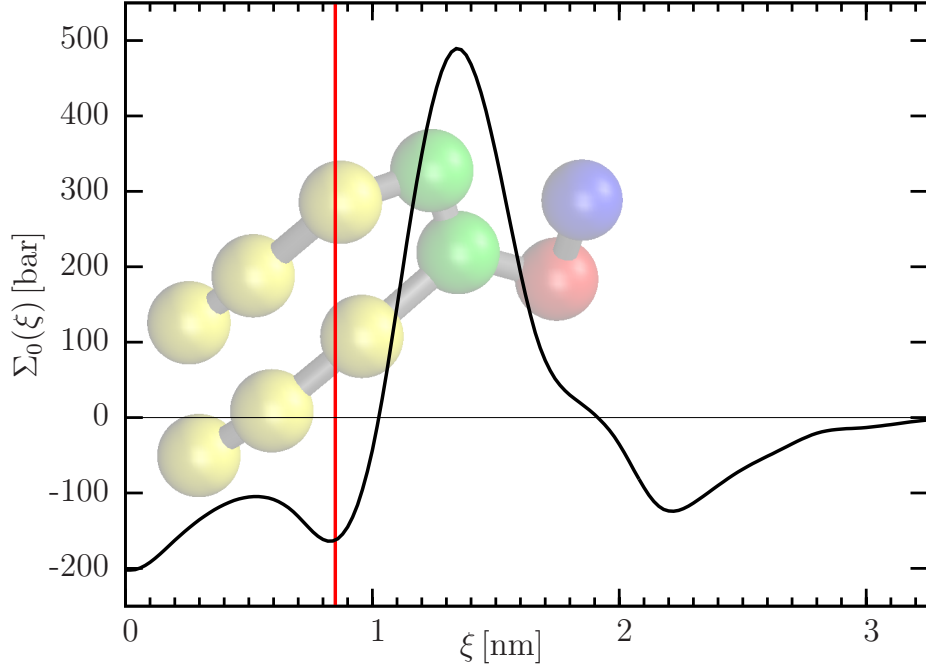


Figure 3.20: Stress profile $\Sigma_0(\xi)$ from Equation (3.59) for the MARTINI DMPC model. The red vertical line denotes the position of the pivotal plane. For reference purposes, the faded lipid model in the background has all beads located at their average distance from the bilayer’s midplane. (The apparent tilt is an artifact of this enforced representation; at 300 K MARTINI DMPC is in an untilted fluid L_α phase.) Curiously, the stress profile shows structure into the water phase that reaches almost a nanometer beyond the position of the outermost lipid bead.

we obtain the corresponding bilayer relations

$$\mathcal{M}_b^{(0)} = \Sigma , \quad (3.63a)$$

$$\mathcal{M}_b^{(1)} = 0 , \quad (3.63b)$$

$$\mathcal{M}_b^{(2)} = \bar{\kappa} , \quad (3.63c)$$

where (3.63b) is a consequence of bilayer up-down symmetry. Combining Equations (3.61), (3.62), and (3.63c), we get

$$\bar{\kappa} = 2[\mathcal{M}_m^{(2)} + 2\mathcal{M}_m^{(1)}z_0 + \mathcal{M}_m^{(0)}z_0^2] \quad (3.64a)$$

$$= 2[\bar{\kappa}_m - 2\kappa_m K_{m0}z_0 + \frac{1}{2}\Sigma z_0^2] , \quad (3.64b)$$

showing that the Gaussian curvature modulus of the bilayer can be obtained from the first three moments of the monolayer’s lateral stress profile. The third term vanishes at zero tension; and while even for simulations ostensibly at $\Sigma = 0$ the residual tension does sometimes not quite vanish, it is typically so small that the z_0^2 -correction

contributes negligibly to the total expression, and so it is usually ignored. Notice finally that Equation (3.64b) expresses $\bar{\kappa}$ in terms of monolayer observables that could be defined without reference to an underlying stress profile. Indeed, Equation (3.64b) can alternatively be derived by relating the monolayer Hamiltonian (3.1) to its bilayer counterpart with the help of the parallel surface equations (3.3).

Calculating the moments using z_0

Having obtained the position of the pivotal plane, we can calculate the monolayer moments without having to guess z_0 . Let us take the Cooke model as an example: Figure 3.19 shows the stress profile $\Sigma_0(\xi)$, computed for a tensionless membrane consisting of 128 lipids.

Using an average value across all our simulations, $z_0 = 1.475\sigma$, we find the extremely large positive spontaneous curvature $K_{m0} = 0.617\sigma^{-1}$, and the *positive* monolayer Gaussian modulus $\bar{\kappa}_m = 0.628 k_B T$. Here we use the latest value of $\kappa_m = \frac{1}{2}\kappa = 6.4 k_B T$ [57]. Since $\partial\bar{\kappa}_m/\partial z_0 = 7.9 k_B T/\sigma$ in the vicinity of z_0 , this modulus only becomes negative for $z_0 < 1.396\sigma$, significantly smaller than the actual pivotal plane position. The Gaussian modulus for the bilayer, however, $\bar{\kappa} = \mathcal{M}_b^{(2)} = -22.15 k_B T$. It is quite curious that the Gaussian modulus for the bilayer is extremely far on the negative side, while the monolayer modulus is even positive. One consequence of this is that from the three terms in Equation (3.64b), the *second* term contributes by far the most to $\bar{\kappa}$. Even without comparing to the measured $\bar{\kappa}$ value [55] these numbers appear suspicious—and they cannot simply be blamed on the coarse-grained nature of the model, since the connection between stress profile and these parameters makes no assumption about how physically realistic a model is.

Applications related to the moments

These values can give us more insights into a lot of problems. Here we only mention two examples.

The first example is that Hu *et al.* have recently pointed out discrepancies in the link between the stress moments and the elastic parameters, based in part on a direct way to determine the Gaussian modulus of the bilayer [55, 56]. For instance, while the direct method indicates $\bar{\kappa}/\kappa \approx -0.92$ for the Cooke model (at the state point considered in this paper), the stress profile method instead suggests $\bar{\kappa}/\kappa \approx -1.7$ [55]. For the MARTINI DMPC method they report $\bar{\kappa}/\kappa \approx -1$, but using the more recently determined value for the bending modulus of MARTINI DMPC, $\kappa \approx 29 k_B T$ [57], this would change to $\bar{\kappa}/\kappa \approx -0.7$; in contrast, the stress profile

approach gives $\bar{\kappa}/\kappa \approx -0.07$ (with the new value for κ) [56].

Now we can push this problem further to the monolayer situation. For the Cooke model, based on our previous result, it is obvious that $\bar{\kappa}_m/\kappa_m = 0.10$. And if we apply the same analysis in the MARTINI DMPC case, this leads to $\bar{\kappa}_m/\kappa_m = -0.23$ (using the more recent value for $\kappa_m = \frac{1}{2}\kappa = 14.5 k_B T$ [57]). Also, the slope of $\bar{\kappa}_m(z_0)$ in the vicinity of the pivotal plane is now negative, $\partial\bar{\kappa}_m/\partial z_0 \approx -2.8 k_B T/\sigma$. This monolayer elastic ratio in itself is not unreasonable, but the strong difference to the bilayer ratio implies that Equation (3.61b) and (3.64b) compensate this with a negative spontaneous monolayer curvature of $K_{m0} = -0.1 \text{ nm}^{-1}$, which goes against the experimental finding that DMPC should have a quite noticeable positive spontaneous curvature of $K_{m0} = +0.3(1) \text{ nm}^{-1}$ [84].

The second example is that the position of the pivotal plane helps us to gauge how strongly these moments are affected by membrane undulations. While fluctuations will always smear out the measured *function* $\Sigma_0(\xi)$, this does not necessarily affect the *moments*. In fact, Hu *et al.* have shown that for symmetric membranes the lowest order bilayer moment that is affected is $\mathcal{M}_b^{(4)}$ [56]. However, they also show that the same is not true for the monolayer moments (Equation (3.61)), for which one additionally needs the root mean square width δ of the fluctuations to be small compared to z_0 . Since $\delta^2 \simeq k_B T L^2 / 16\pi^3 \kappa$, where L is the side length of a square membrane patch under periodic boundary conditions, requiring $\delta/z_0 < 10\%$ limits the membrane to $L \lesssim 2.23 z_0 \sqrt{\kappa/k_B T}$.

Relying on the older value $\kappa \approx 40 k_B T$ and the guess $z_0 \approx 1.25 \text{ nm}$ this led Hu *et al.* to conclude $L \lesssim 17.5 \text{ nm}$, and hence $N_{\text{lipids}} \lesssim 10^3$ (since the area per MARTINI DMPC lipid at 300 K is $a_\ell \simeq 0.6 \text{ nm}^2$) [56]. Using the newer rigidity $\kappa = 29 k_B T$ and the measured value $z_0 = 0.85 \text{ nm}$ instead gives $L \lesssim 10.3 \text{ nm}$ or $N_{\text{lipids}} \lesssim 350$. Since the stress profile in Figure 3.20 was calculated with 256 lipids, we are still on the safe side, but less comfortably so than what Hu *et al.* originally surmised.

For the Cooke model we find $L \lesssim 11.8 \sigma$ and hence $N_{\text{lipids}} \lesssim 230$ (since $a_\ell \simeq 1.2 \sigma^2$). However, the stress profile discussed in Ref. [55] was based on a simulation of a membrane containing 1000 lipids, which would lead to significant broadening (as visible in Figure 3.19). We hence re-calculated the stress for a membrane consisting of only 128 lipids, leading to a substantially “sharper” profile (the solid line in Figure 3.19). While the bilayer moments are unaffected, monolayer observables change; for instance, the reference position z_0 where $\bar{\kappa}_m = 0$ shifts from 1.45σ to 1.40σ , about 3%. This seems small, but observe that it is much larger than the accuracy with which we can determine z_0 . These considerations illustrate that knowing the pivotal plane position may be important to evaluate the reliability of stress profile moments, or plan simulation parameters aimed at determining them, even if they might at first sight not even

depend on the value of z_0 (like the first monolayer moment).

3.6.3 Pivotal plane and features in the stress profile

A few suggestions have been made in the past how the position of the pivotal plane can be gleaned from features observable in $\Sigma_0(\xi)$ [103, 106, 107, 108, 121, 138]. How do they fare?

For the Cooke model, the measured position $z_0 \approx 1.475 \sigma$ does not correspond to any particular feature in the stress profile: neither the minimum (at $\xi \approx 2.02 \sigma$) nor the zero (at $\xi \approx 1.38 \sigma$) are close enough to be plausible candidates; and the equivalent of the first extremum inwards (at $\xi \approx 0.79 \sigma$, only visible in the sharp profile) is *much* too far inwards.

Then let us move on to the MARTINI data, for which $\Sigma_0(\xi)$ exhibits more structure (see Figure 3.20). While the overall tension peak (at $\xi \approx 1.34 \text{ nm}$) does not appear to be a good choice for z_0 [106, 107], the first minimum following this peak when going towards the bilayer center (at $\xi \approx 0.83 \text{ nm}$) is quite close to our measured value for z_0 [108, 121, 138].

3.6.4 Dependence of the pivotal plane on lipid spontaneous curvature

With access to the pivotal plane, besides using the value of z_0 to get other physical quantities, another interesting exploration would be checking the pivotal plane position's change after tuning certain parameter of the system, such as the lipid spontaneous curvature.

The effect of the spontaneous curvature is likely small, but we can also measure z_0 very precisely. Since nothing is known about such a relation, we will restrict to the case of the Cooke model, where a qualitative tuning of lipid curvature via tuning of head-bead size is readily accomplished [20], even though a quantification of the value of the curvature is not easily possible, given that the number extracted from the first moment of the stress profile might not be reliable.

First of all, it is curious that not even the *sign* of the effect is obvious. Here are two different arguments, leading to opposite conclusions. Equation (3.12) shows that bending an initially flat thin sheet will move the pivotal plane *away* from the inner surface (if the Poisson ratio is positive). Now imagine instead a sheet with a relaxed shape that has some positive spontaneous curvature K_{m0} . Straightening it

σ_h [σ]	$\langle \xi_h \rangle$ [σ]	z_0 [σ]	$z_0 / \langle \xi_h \rangle$
0.91	2.1877(51)	1.4036(123)	0.6416(58)
0.93	2.1862(77)	1.4329(64)	0.6554(37)
0.95	2.1911(71)	1.4862(46)	0.6783(30)
0.97	2.1808(68)	1.5184(73)	0.6962(40)

Table 3.6: Additional Cooke model simulations for determining the dependence of z_0 on the size of a lipid head bead, σ_h , and hence lipid curvature. For each value of σ_h *all* systems from Table 3.1 were re-run for $4 \times 10^4 \tau$, and the results were averaged. The average head bead distance $\langle \xi_h \rangle$ was determined by simulating a flat tensionless membrane of 320 lipids for $2 \times 10^3 \tau$.

out, in order to make it part of a flat bilayer, will laterally expand the inner region and hence shift the pivotal plane *towards* this direction. Hence, we expect

$$z_0 = z_{\text{rel}} \left[1 - \frac{1}{2} \frac{\nu}{1 - \nu} K_{m0} z_{\text{rel}} + \mathcal{O}(z_0^2) \right], \quad (3.65)$$

where z_{rel} is the position of the pivotal plane in the *curved but relaxed* state. This continuum-theory argument implies that the pivotal plane moves closer to the bilayer midplane as the spontaneous curvature increases, and the reason is a Poisson ratio effect.

Now consider instead Equations (3.16) or (3.22), which determine the position of the pivotal plane from the ratio $\rho = N_+/N_-$ of lipids between outer and inner leaflet of cylinders or spheres. If we were to increase the spontaneous lipid curvature, we make it easier for lipids to fit into the outer layer, but harder to fit into the inner one, which should in turn translocate a few lipids from the inside to the outside as K_{m0} increases, thus making ρ larger. And since the right hand side of Equations. (3.16) and (3.22) monotonically increases with ρ , this suggests that z_0 should *increase* with K_{m0} .

To investigate which trend (if any) prevails, we calculate z_0 in simulations relying on the simpler cylindrical protocol, but look at Cooke lipids with different spontaneous curvatures, which we tune by the head bead size. We leave all parameters as before, but pick the head bead sizes from the set $\sigma_h/\sigma \in \{0.91, 0.93, 0.95, 0.97\}$, where $\sigma_h = 0.95\sigma$ is the case studied so far; parameters and results are summarized in Table 3.6. Simple geometric arguments show that the change in lipid spontaneous curvature is proportional to the change in head bead size [55], and so we will monitor z_0 as a function of σ_h . Since changing the head bead size might also alter a lipid's length, and hence the monolayer thickness, we must also remeasure $\langle \xi_h \rangle$. Interestingly, we find it to stay the same within error; the change in lipid length is instead

compensated by lipids moving closer to or farther away from the midplane.

Figure 3.21 plots the ratio $z_0(\sigma_h)/\langle\xi_h(\sigma_h)\rangle$ as a function of head bead size σ_h . We see that the slope is unambiguously positive, $+0.963(11)\sigma^{-1}$, showing that—*ceteris paribus*—larger spontaneous curvatures move the pivotal plane outwards.

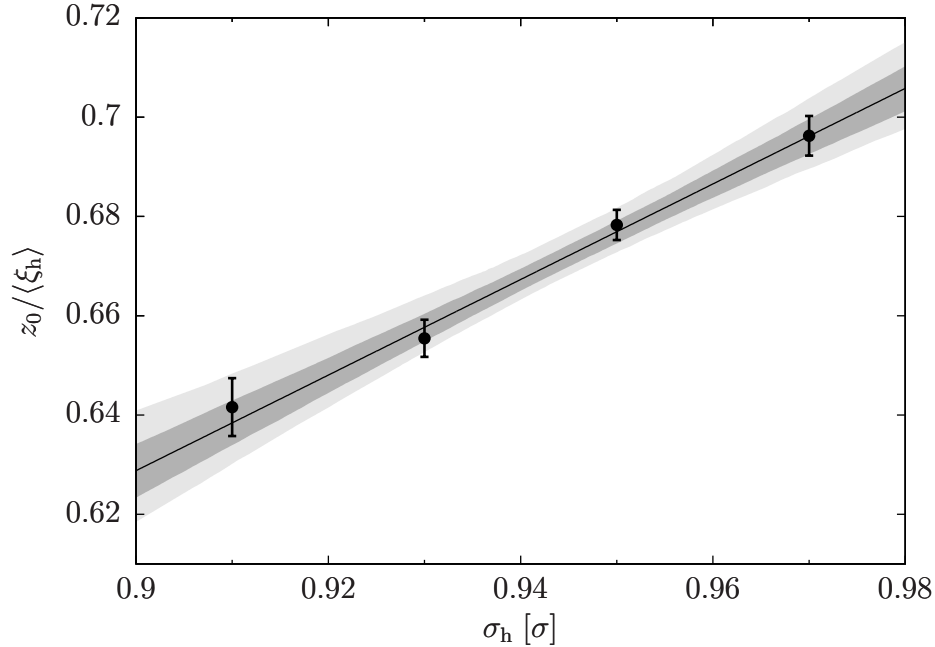


Figure 3.21: Position of pivotal plane measured versus lipid length, $z_0/\langle\xi_h\rangle$, as a function of the head group size σ_h . The case $\sigma_h = 0.95\sigma$ is the usual parameter choice; increasing σ_h will increase the lipid curvature. The confidence bands are 67% and 95% respectively.

Recall that we claim that the small value $z_0/\langle\xi_{Ph}\rangle = 0.491(4)$ measured for MARTINI DMPC can *not* be attributed to a lipid curvature effect in Section 3.6.1. Here is the reason: DMPC is believed to have a sizable *positive* spontaneous curvature of $K_{m0} = +0.3(1)\text{ nm}^{-1}$ [84], whereas Chen and Rand measure the spontaneous curvature of DOPE (taken at the pivotal plane) to be $K_{m0} = -0.35(1)\text{ nm}^{-1}$. And yet, (MARTINI) DMPC has its (relative) pivotal plane position much further inwards than (real world) DOPE.

3.7 Summary

Previous work has demonstrated that the buckled geometry can be used to determine membrane elastic moduli [57, 99], and in this chapter we have shown that the same

geometry can also be used to retrieve information on another elastic property: the pivotal plane. Its location, due to the effect of the Poisson ratio, depends linearly on the local curvature of the membrane, to the lowest order. To be precise, we therefore define the limit at vanishing local curvature as the pivotal plane position, z_0 . This correction is actually not negligible for many high curvature cases, such as the inverse hexagonal phases.

We tested our method for three different resolution lipid models: the Cooke three bead model, MARTINI DMPC and the Berger model. For the Cooke model, we start with a conceptually very straightforward analysis of simple geometrical configurations, sphere and cylinder, after which we move on to the buckle configuration. With some conceptual and technical care, all three models' results turn out to agree with each other very well. This proves that our more involved method that relies on analyzing buckled membranes is actually measuring the same observable, the pivotal plane.

After validating our buckle protocol, we apply the same process to the MARTINI DMPC and atomistic Berger model. For MARTINI DMPC, we find the pivotal plane in the middle of the lipid, about 0.4 nm beneath the *sn1* glycerol bead, which is not quite the same as what has been found in experiment [16]: even though it is on DOPE, after converting back to the flat membrane, the pivotal plane is found at around $\frac{2}{3}$ of the lipid height, not $\frac{1}{2}$.

This discrepancy is likely due to the coarse-grained nature of MARTINI DMPC, especially the fact that the tails are not as pliable as those of real lipids. This assumption is actually supported by the result of the higher resolution Berger model. Since the Berger model has a finer tail structure, they can better adjust their conformational tail statistics to the local curvature state of the lipid leaflet. The pivotal plane is indeed found a little beneath the glycerol backbone, which is compatible with other studies.

Chapter 4

Determining the lipid tilt modulus

The major work discussed in this chapter has been published in Ref. [142].

4.1 Introduction

4.1.1 Tilt plays an important role in biological processes

We have mentioned the significance of a membrane's elastic deformation, which is crucial in numerous biological and biotechnological processes. The study of the corresponding elastic properties is essential for understanding lipid membrane behavior.

The traditional study, as we mentioned earlier, starts from Helfrich and Canham [13, 48], who describe the membrane as a smooth, structureless sheet with a penalty term for bending and stretching in the energy expression. Hence, the most extensively studied elastic modes of membrane are bending [48] and stretching [35]. The pivotal plane, which has been our focus in the last chapter, is a very important concept when the membranes are described as mathematical surfaces in Helfrich's theory. Besides all these properties, lipid membranes undergo another deformation in many situations, namely, the tilt of the lipid molecules' hydrocarbon chains away from the membrane normal vector.

Tilt effects are found in many biological situations, especially when the monolayer structure is perturbed by localized defects or membrane insertions. There are many examples involving the tilt degree of freedom, including the intermediate structure of membrane fusion stalks [18, 64, 65, 128], the line tension between lipid domains [68], aqueous pores in lipid bilayers [88], and the deformation caused by protein insertion [22, 66, 88, 89, 90]. What is more, many non-biological phases, even if not as important for biological study, also have this tilt deformation. A prominent example is the inverse hexagonal phase [44], which we have already encountered in Chapter 3, where chain tilt is generated by the molecular packing within the hydrophobic inter-

stices of neighboring lipid cylinders [116].

Due to its unique significance, lipid tilt has drawn more attention recently. The original Helfrich theory, however, is insufficient for such studies, since it only considers bending and stretching, and a generalization of Helfrich theory involving tilt terms is needed. Hamm and Kozlov (HK) [45] have derived an elastic theory including the tilt field for non-stretched monolayers. This theory has inspired much work related to the tilt field; for example, May *et al.* [87] simulated the undulation of a flat membrane and provide a new explanation of the transition between bending and protrusion fluctuations modes in the context of HK theory. In HK theory, in front of the quadratic tilt term, a new modulus is introduced, the tilt modulus, which reflects how much the membrane will respond to the tilt deformation, and scientists have begun to measure it in simulation [71, 140] and experiment [59, 97]. We will discuss this more in Section 4.4.

In this chapter, we will first introduce a mathematical description of the tilt field, as well as HK theory in Section 4.2. Based on HK theory, two strategies on the subject of a buckled membrane are derived, including a direct measurement of the tilt field, and an indirect method generated from the shape analysis. Then we will show the results for each method (Section 4.3) and discuss their physical meaning (Section 4.4).

4.2 Theoretical Framework

4.2.1 Hamiltonian with a lipid tilt field: the theory of Hamm and Kozlov

We have reviewed the Helfrich Hamiltonian in the last chapter, and displayed the Helfrich Hamiltonian for the monolayer in Equation (3.1). This equation, however, does not account for lipid tilt, which describes the difference between a lipid's orientation and the membrane's local normal. In particular, as shown in Figure 4.1, the directions of lipids, \mathbf{n} , plotted as red and blue lines, need not coincide with the membrane's local normal, \mathbf{N} , which should be perpendicular to the black outline. To describe this difference, an additional tangential vector field \mathbf{T} has been introduced [78]

$$\mathbf{T} = \frac{\mathbf{n}}{\mathbf{n} \cdot \mathbf{N}} - \mathbf{N} . \quad (4.1)$$

Since both \mathbf{n} and \mathbf{N} are unit vectors, the tilt angle θ between these two vectors, as shown in Figure 4.1, is simply

$$\tan \theta = |\mathbf{T}| . \quad (4.2)$$

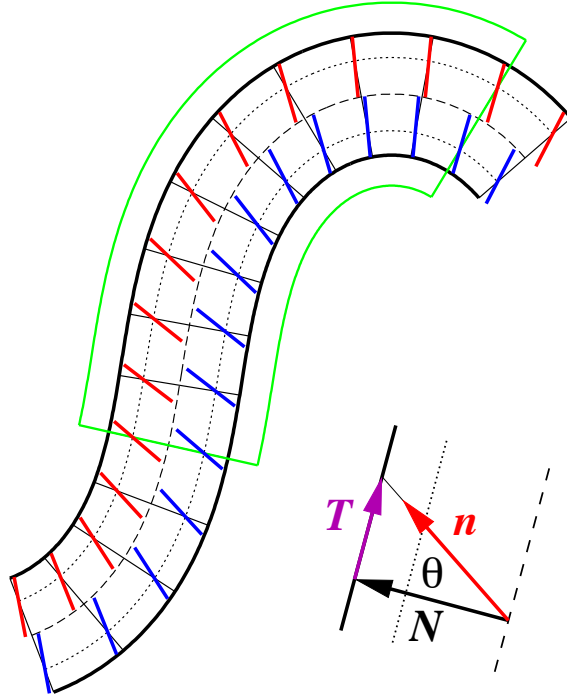


Figure 4.1: Illustration of lipid tilt fields in a buckled lipid bilayer. Solid black curves are the outer surfaces of the bilayer, the dashed curve is the bilayer’s midplane, and the two dotted curves are the pivotal planes of each leaflet. Local normals are indicated by solid lines perpendicular to the midplane. Tilted lipids are illustrated as red and blue lines in the upper and lower leaflet, respectively; the extent of tilt is strongly exaggerated. The green outline is an example of a cut-out segment. Notice that for this particular cut the head groups of the lipids in the upper leaflet tilt *into* the cut-out segment, while the head groups of the lipids in the lower leaflet tilt *out* of the cut. The small inset illustrates the tilt definition from Equation (4.1).

As mentioned in Section 1.2.2, Hamm and Kozlov have developed a theory that includes this degree of freedom [44, 45]. In their theory, the new elastic description containing the \mathbf{T} field has two major modifications compared to the original Helfrich Hamiltonian.

Firstly, a new term involving the tilt field itself is added, in a quadratic form together with a tilt modulus $\kappa_{t,m}$. Secondly, the curvature tensor \mathbb{K} gets replaced by a “dressed” curvature tensor $\tilde{\mathbb{K}} = \mathbb{K} + \nabla \otimes \mathbf{T}$ (where ∇ is the vector differential operator on the surface). This changes the total curvature into $\tilde{K} = \text{Tr}(\tilde{\mathbb{K}}) = \text{Tr}(\mathbb{K} + \nabla \otimes \mathbf{T}) = K + \nabla \cdot \mathbf{T}$ (meaning, the tilt divergence adds to the curvature), and the Gaussian curvature into $\tilde{K}_G = \det(\tilde{\mathbb{K}})$. Hence, their joint curvature-tilt Hamiltonian becomes

$$H = \int dA \left\{ \frac{1}{2} \kappa_m \left(K + \nabla \cdot \mathbf{T} - K_{0,m} \right)^2 + \bar{\kappa}_m \tilde{K}_G + \frac{1}{2} \kappa_{t,m} \mathbf{T}^2 \right\} .$$

Here the difference between K_G and \tilde{K}_G is of higher order (it contains terms quadratic in both tilt *and* curvature), and so we can ignore the tilde to lowest order. In fact, since we will subsequently be interested in planar buckles, for which $K_G = 0$, the Gaussian term will vanish anyways.

We have retrieved the shape equation using functional variation in Section 2.4.3. Similarly, if we vary Equation (4.3) with respect to \mathbf{T} , we obtain the Euler-Lagrange equation satisfied by the tilt

$$\nabla \nabla \cdot \mathbf{T} - \ell^{-2} \mathbf{T} = -\nabla K \quad \text{with } \ell = \sqrt{\kappa_m / \kappa_{t,m}} . \quad (4.3)$$

Two things are worth mentioning about this equation: first, the Green function of the left hand side has an exponential decay form, and the characteristic length ℓ describes the range over which a tilt excitation decays. Although the values of the two moduli κ_m and $\kappa_{t,m}$ vary, the characteristic length ℓ is on the order of one nanometer (the typical simulation results of both moduli can be found in Table 4.2, and experimental results will be discussed in Section 4.4). In other words, the influence of tilt on the membrane is very local. Second, the right hand side indicates that the gradient of the local curvature will induce such a tilt field. If a membrane does not have a gradient in the curvature, such as a flat membrane, a sphere, a cylinder, or a minimal surface, no tilt field will exist in the membrane.

4.2.2 Hamm and Kozlov model for the buckle

Equation (4.3) can be applied to an undulatory buckle as well. Since such a buckle is flat along one direction, the whole situation in fact reduces to a one-dimensional problem. For a given membrane, the tilt field T (not in bold, since it is only a one-dimensional variable here) can be written as a function of arc length s , and so Equation (4.3) becomes

$$T'' - \ell^{-2} T = -K' . \quad (4.4)$$

The explicit form of the Green function is $G_T(s) = -\frac{1}{2} \ell e^{-|s|/\ell}$, showing that, indeed, tilt decays on the length-scale ℓ , and that the excitation magnitude is proportional to $\ell \sim \kappa_{t,m}^{-1/2}$.

If no tilt is considered, we have the shape equation from Equation (3.25), which contains the expression for ψ'' . Since $K' = \psi''$, we can plug Equation (3.25) back into Equation (4.4), and we get

$$T'' - \ell^{-2} T = \lambda^{-2} \sin \psi . \quad (4.5)$$

This can be used to solve T .

However, the assumption that the presence of tilt does not affect the membrane's shape requires further discussion. The imposed curvature will introduce a tilt field $T(s)$ in the energy expression (Equation (3.24)), hence Equation (3.25) needs to be rewritten. In other words, instead of a simple clean expression of $\psi(s)$, a precise solution requires us to solve for $\psi(s)$ and $T(s)$ simultaneously.

Fortunately, the correction due to this tilt effect on the geometrical shape can be ignored to the lowest order. From a physical perspective, the characteristic length ℓ , or the range on which the tilt field decays, is on the order of a few nanometer, as we said earlier. The shape, on the other hand, usually varies on much larger scales.

4.2.3 Fourier expansion of the buckle

The field $T(s)$ can be calculated from Equation (4.5), but the right hand side—in the case of an Euler buckle—contains a Jacobi elliptical function, and this renders the resulting equation for the tilt rather unwieldy. However, the buckle configuration holds an inherent advantage of periodicity, thus applying a Fourier expansion and comparing the coefficients on both sides appears to be a natural and much easier approach to solve for $T(s)$.

The expression of $\psi(s)$ is given in Equation (3.31). Using some elementary identities for Jacobi elliptic functions, we can rewrite the sine of the angle as

$$\sin \psi(s) = -2\sqrt{m} \lambda \frac{d}{ds} \text{cn}[s/\lambda, m] . \quad (4.6)$$

Our aim is to expand the right hand side in a Fourier series in s . To do so, let us recall that elliptic functions are doubly periodic—in both the real and the imaginary direction. The quarter period in the real direction is given by $\mathcal{K} = K[m]$, and the one in the imaginary direction is $\mathcal{K}' = K[1 - m]$, where $K[m]$ is the complete elliptic integral of the first kind [4]. From these periods we can define the so-called “nome” $q = \exp\{-\pi\mathcal{K}'/\mathcal{K}\}$. It now turns out that all elliptic functions can be written as Fourier expansions involving powers of the nome. Specifically, we are interested in $\text{cn}[x, m]$, for which the expansion is [4]

$$\text{cn}[x, m] = \frac{2\pi}{\mathcal{K}\sqrt{m}} \sum_{\substack{n=1 \\ n \text{ odd}}}^{\infty} \frac{q^{n/2}}{1 + q^n} \cos \frac{\pi n x}{2\mathcal{K}} . \quad (4.7)$$

Using this in Eqn. (4.6), we get the series expansion

$$\sin \psi(s) = \frac{2\pi^2}{\mathcal{K}^2} \sum_{\substack{n=1 \\ n \text{ odd}}}^{\infty} \frac{n q^{n/2}}{1+q^n} \sin \frac{2\pi n s}{4\mathcal{K}\lambda} . \quad (4.8)$$

Since we furthermore know that this function has period L , it must be true that

$$\frac{L}{4\lambda} = \mathcal{K} , \quad (4.9)$$

and with this we can eliminate the occurrence of \mathcal{K} in the argument of the sine, rewriting the Fourier series expansion in such a way that the period L becomes manifest:

$$\sin \psi(s) = \frac{2\pi^2}{\mathcal{K}^2} \sum_{\substack{n=1 \\ n \text{ odd}}}^{\infty} \frac{n q^{n/2}}{1+q^n} \sin \frac{2\pi n s}{L} . \quad (4.10)$$

This expansion still contains the elliptic quarter periods \mathcal{K} and \mathcal{K}' , which in turn depend on the elliptic parameter m . We have previously shown that the latter can be written as a rapidly converging series expansion in the buckling strain $\gamma = (L - L_x)/L$, see Equation (3.32). From this we obtain the coefficients of the Fourier expansion as a Taylor series in γ :

$$\sin \psi(s) = \lambda^2 \left(\frac{2\pi}{L} \right)^2 \sum_{\substack{n=1 \\ n \text{ odd}}}^{\infty} B_n(\gamma) \sin \frac{2\pi n s}{L} , \quad (4.11)$$

where the coefficients B_n are defined by

$$B_n(\gamma) = 2\sqrt{\gamma} A_n(\gamma) n \left(\frac{\gamma}{16} \right)^{\frac{n-1}{2}} , \quad (4.12)$$

and the Taylor series $A_n(\gamma)$ for $n \leq 9$ (*i. e.*, the first 5 modes) are listed in Table 4.1 (the notation is chosen such that $A_n(0) = 1$ for all n).

4.2.4 Determining the tilt field

So far, we have a Fourier expansion of the right hand side of Equation (4.5)

$$\lambda^{-2} \sin \psi(s) = \left(\frac{2\pi}{L} \right)^2 \sum_{\substack{n=1 \\ n \text{ odd}}}^{\infty} B_n(\gamma) \sin \frac{2\pi n s}{L} . \quad (4.13)$$

Since the equation is linear, the field $T(s)$ should have the same form

$$T(s) = \sum_{\substack{n=1 \\ n \text{ odd}}}^{\infty} C_n \sin \frac{2\pi n s}{L} . \quad (4.14)$$

n	$A_n(\gamma)$
1	$1 + \frac{1}{8}\gamma + \frac{19}{512}\gamma^2 + \frac{7}{512}\gamma^3 + \frac{2867}{524288}\gamma^4 + \dots$
3	$1 + \frac{9}{16}\gamma + \frac{159}{512}\gamma^2 + \frac{1411}{8182}\gamma^3 + \dots$
5	$1 + \frac{15}{16}\gamma + \frac{355}{512}\gamma^2 + \dots$
7	$1 + \frac{21}{16}\gamma + \dots$
9	$1 + \dots$

Table 4.1: Coefficients $A_n(\gamma)$ for the series expansions introduced in Equation (4.11) and (4.12).

Now the left hand side of Equation (4.5) becomes

$$T'' - \ell^{-2}T = \sum_{\substack{n=1 \\ n \text{ odd}}}^{\infty} C_n \left[\left(\frac{2\pi n}{L} \right)^2 + \frac{1}{\ell^2} \right] \sin \frac{2\pi n s}{L} . \quad (4.15)$$

By comparing coefficients, we have

$$C_n(\gamma) = \frac{B_n(\gamma)}{n^2 + (L/2\pi\ell)^2} . \quad (4.16)$$

This is the exact solution of the tilt field, except for the one approximation that we ignore the tilt effect on the shape. What is more, another approximation can be made as well: the term n^2 in the denominator of Equation (4.16) can be neglected. This approximation, however, is not straightforward. To begin with, if the tilt modulus is small, ℓ is large. Hence, for the first two modes $n = 1$ and $n = 2$, and maybe even for the third mode $n = 3$, the competing term n^2 can be neglected. And we may hope that for even higher modes the coefficients $B_n(\gamma)$ become so small, mostly because of the exponentially decreasing term $(\gamma/16)^{(n-1)/2}$, that we can ignore the mode (and all subsequent ones) altogether. For instance, at $\gamma = \frac{1}{2}$, the first few values of the B_n are

$$B_1\left(\frac{1}{2}\right) \approx 1.52 \quad (4.17a)$$

$$B_3\left(\frac{1}{2}\right) \approx 0.184 \quad (4.17b)$$

$$B_5\left(\frac{1}{2}\right) \approx 0.0119 \quad (4.17c)$$

$$B_7\left(\frac{1}{2}\right) \approx 0.000629 \quad (4.17d)$$

$$B_9\left(\frac{1}{2}\right) \approx 0.0000281 . \quad (4.17e)$$

This is interesting because if we scratch the term n^2 in the denominator, what remains are—up to some overall factor—the Fourier coefficients of $\sin \psi$. This means that to some decent (but admittedly hard to control) approximation, we have the following result:

$$T(s) \approx \left(\frac{2\mathcal{K}}{\pi} \right)^2 \left(\frac{2\pi\ell}{L} \right)^2 \sin \psi(s) = \varepsilon(\gamma) \sin \psi , \quad (4.18)$$

where we defined

$$\varepsilon(\gamma) = \left(\frac{2\pi\ell}{L} \right)^2 \left(1 + \frac{1}{2}\gamma + \frac{9}{32}\gamma^2 + \dots \right) . \quad (4.19)$$

This expression for $\varepsilon(\gamma)$ results from inserting the series expansion of $m(\gamma)$ from Equation (3.32a) into $\mathcal{K} = \mathcal{K}[m(\gamma)]$ and expanding again.

Being the amplitude in front of $\sin \psi(s)$, $\varepsilon(\gamma)$ is the largest *possible* value of the tilt; the largest one that is *realized* occurs at the inflection points of the buckle, where $\psi(s) = \psi_i$ takes its maximum value. From Equation (4.6), combined with Equation (4.9), we can readily deduce that

$$\sin \psi_i = \sin \psi(L/4) = 2\sqrt{m(1-m)} , \quad (4.20)$$

and inserting the series expansion for $m(\gamma)$ from Equation (3.32a), we arrive at

$$\sin \psi_i = 2\sqrt{\gamma} \left(1 - \frac{9}{16}\gamma - \frac{25}{512}\gamma^2 - \dots \right) . \quad (4.21)$$

Together with the series expansion for $\varepsilon(\gamma)$ from Equation (4.19), this gives a maximum tilt amplitude of

$$\frac{T_{\max}(\gamma)}{(2\pi\ell/L)^2} = 2\sqrt{\gamma} \left(1 - \frac{1}{16}\gamma - \frac{25}{512}\gamma^2 - \dots \right) . \quad (4.22)$$

Since the right hand side becomes 1 for $\gamma \approx 0.26$, this result shows that $(2\pi\ell/L)^2$ can be viewed as the maximum tilt which lipids assume in a buckle strained by about a quarter of its length. From Equation (4.2), the maximum tilt angle is hence $\theta_{\max} = \arctan(T_{\max})$.

Let us take a look at Equation (4.18) again. We know from the EL equation (Equation (3.25)) that $\sin \psi = -\lambda^2 \psi'' = -\lambda^2 K'$, and using the identity (4.9), we see that this is equivalent to

$$T(s) = \ell^2 K'(s) . \quad (4.23)$$

This is just the Euler-Lagrange equation for the tilt (Equation (4.4)), but with the second derivative term removed.

Now, $T'' \ll T/\ell^2$ holds if the tilt varies slowly compared to the decay length ℓ , and this in turn happens when the function sourcing the tilt, K' , varies sufficiently slowly. But the latter rate is set by the period of the buckle, and so we return to the condition $\ell \ll L$ —which is precisely what motivated us to drop the term n^2 in the denominator of Equation (4.16).

This also provides a new insight how to get the tilt modulus. For Equation (4.18), or Equation (4.23), we can measure the tilt $T(s)$, and we can measure $K'(s)$, or $\sin(\psi)$. Hence, this allows us to measure the value of ℓ . Since we know the bending modulus κ_m , which can also be measured directly from the same buckling simulation, we can extract the value of the tilt modulus $\kappa_{t,m}$.

4.2.5 From Pivotal Plane to Tilt modulus

We have just provided a possible way to measure the tilt modulus; but this method might be difficult to implement, since the direct measurement of tilt is extremely challenging. We will see that later in the results section. But there is another approach, even though not so obvious at the beginning, to help us obtain the tilt modulus.

Recall that in Section 3.3.2 we found the following relations

$$\frac{a_{\pm}N_{\pm}}{L_y} = \Delta s \pm z_0 \Delta\psi , \quad (4.24)$$

where Δs is the arc length between the two cuts, $\Delta\psi$ is the angle by which the buckle changes along the cut, z_0 is the distance of the pivotal plane from the bilayer's midplane, and L_y is the width of the buckle.

The key insight—as far as tilt is concerned—is that tilt further increases or decreases the available area. As Figure 4.1 illustrates, different regions along the height of a lipid may tilt into or out of any chosen cut, thus changing the count of lipids in that region. Moreover, the effect does not cancel but *amplify* across the two leaflets, thus affecting the overall lipid imbalance in a tilt-dependent way. Considering the geometry outlined in Figure 4.1, we arrive at the following tilt-correction:

$$\frac{a_{\pm}N_{\pm}}{L_y} = \Delta s \pm z_0 \Delta\psi + (\xi - z_0)[T_{\pm}(\bar{s}) - T_{\pm}(\underline{s})] , \quad (4.25)$$

where ξ is the distance away from the bilayer's midplane, which we use as a reference for lipid counting. For instance, if we use a particular bead as the reference bead, then ξ is the (average) distance of that bead from the midplane.

As it stands, this result is not yet very useful. We do not measure the tilt in our simulation, and as we just said, it is very hard to do so. Hence, we will instead use Equation (4.23) to link the tilt to the local curvature gradient. However, there is yet one more complication we need to consider: the curvature we speak of is the one of the bilayer midplane, but the monolayer tilt fields couple to the curvatures $K_{p,\pm}$ at the two pivotal planes, not the curvature K at the midplane. However, these curvatures are connected by the parallel surface relation [27]

$$K_{p,\pm} = \frac{K \pm 2K_G z_0}{1 \pm K z_0 + K_G z_0^2} \quad (4.26a)$$

$$\stackrel{K_G=0}{=} \frac{K}{1 \pm K z_0} \quad (4.26b)$$

$$\stackrel{K z_0 \ll 1}{\approx} K \mp K^2 z_0 , \quad (4.26c)$$

showing that the tilt fields should in fact be written as

$$T_{\pm} = \mp \ell^2 K' (1 \pm 2Kz_0) . \quad (4.27)$$

If we want to calculate ΔT_{\pm} , we need to deal with $\Delta K'$ and $\Delta K'K$. K' , however, is not an ideal variable to use in numerical analysis, since it requires two derivatives of ψ . If we put Equation (4.18) and Equation (4.23) together, obviously we have

$$\ell^2 K' = \varepsilon(\gamma) \sin \psi \approx \varepsilon(\gamma) \psi . \quad (4.28)$$

Here we use the approximation $\sin \psi \approx \psi$. Now K' can be represented by ψ , which is a direct observable in our simulation. Now we insert Equation (4.27) into Equation (4.25) and use Equation (4.28) to replace all the K' . Doing so, we get

$$\frac{a_{\pm} N_{\pm}}{L_y} = \Delta s \pm z_0 \Delta \psi \mp \varepsilon(\gamma) (\xi - z_0) \Delta \psi - 2\varepsilon(\gamma) (\xi - z_0) z_0 \Delta(K\psi) . \quad (4.29)$$

In this equation, all variables stem from pure geometry—except for $\varepsilon(\gamma)$, which is a function of ℓ (Equation (4.19)), or the tilt correction. This gives us access to tilt information from an analysis of the buckle geometry alone.

Here, we are going to follow a similar strategy as in Section 3.3.2. Again, we define two further quantities: first, $M_{\pm} = N_{+} \pm N_{-}$, the sum/difference of the lipid numbers across the cut-out segment, and the quantity evaluated for the whole buckle: $M_{\pm}^{(p)}$. With these definitions, we can rewrite Equation (4.29) as

$$M_{\pm}^{(p)} \Delta s - M_{\pm} L = -M_{\mp}^{(p)} \Delta \psi [z_0(1 + \varepsilon) - \varepsilon \xi] + 2M_{\pm}^{(p)} \varepsilon z_0 (\xi - z_0) \Delta(K\psi) .$$

Since $N_{\text{total}} = M_{+}^{(p)} \gg M_{-}^{(p)} \approx 0$, we will now choose the lower tier signs in order to preserve the information leading to z_0 and ε , as well as avoid dealing with the $\Delta(K\psi)$ term. We can see this in more details later.

Introducing the two variables

$$x_p = M_{+}^{(p)} \Delta \psi \quad \text{and} \quad y_p = M_{-} L - M_{-}^{(p)} \Delta s , \quad (4.30)$$

which are the same as in Section 3.3.2, we can turn Equation (4.30) into the form

$$y_p = [z_0(1 + \varepsilon) - \varepsilon \xi] x_p - 2\Delta(K\psi) z_0 (\xi - z_0) \varepsilon M_{-}^{(p)} . \quad (4.31)$$

The only remaining nuisance is the last term, but thankfully it turns out that we can ignore it. Notice that it contains $M_{-}^{(p)}$, the difference in lipid number across the whole buckle. Since we always set up initial buckles such that $M_{-}^{(p)} = 0$, it can only ever become nonzero due to lipid flip-flop; but for many lipid models—especially the more highly resolved ones (such as MARTINI and Berger)—the flip-flop rate is so small that the initial lipid symmetry is preserved throughout the entire simulation,

and thus the nuisance term vanishes exactly. If the flip flop rate does not vanish (such as in the Cooke model), then $M_-^{(p)}$ will not remain zero during the simulation—but its *average* will. Hence, we can remove this term from Equation (4.31), and arrive at the very simple relation

$$z_0 = \frac{y_p/x_p}{1 + \varepsilon} + \frac{\varepsilon}{1 + \varepsilon} \xi . \quad (4.32)$$

This equation tells us three things. Firstly, the pivotal plane position z_0 is almost equal to the slope y_p/x_p , but that it will very slightly depend on the choice of reference bead, since that bead’s average position ξ away from the bilayer midplane enters the value for z_0 : the farther away the reference bead is, the larger the value of z_0 we will deduce, which agrees with our results in Figure 3.12, Figure 3.15 and Figure 3.17.

A second insight is that we choose a self-consistent way to determine the z_0 . After adding the tilt effect, the intersection between $y_p/x_p = z_0$ and $\xi = z_0$ still satisfies the updated version, Equation (4.32).

And last but not least, if we draw z_0 with respect to ξ , by fitting the slope, we can extract ε , and in turn get the tilt modulus $\kappa_{t,m}$. Using Equation (4.19), and simplifying slightly (because $\varepsilon \ll 1$), we therefore get

$$\kappa_{t,m} = \kappa_m \left(\frac{2\pi}{L} \right)^2 \frac{1 + \frac{1}{2}\gamma + \frac{9}{32}\gamma^2 + \dots}{z'_0(\xi)} . \quad (4.33)$$

Since the bending modulus is known for the system [57] (see also Table 4.2), and we already have the relation between z_0 and ξ from the data in the last chapter, Equation (4.33) permits us to determine the tilt modulus.

4.3 Results for tilt modulus determination

In the last section, we found three approaches to determine the tilt modulus. The corresponding formulas are Equation (4.18), Equation (4.23) and Equation (4.33). The first two equations involves a direct measurement of the buckle’s tilt, while the last one only requires a shape analysis, which has already been done in the last chapter. In this section, we will implement all three methods and explore the their results.

4.3.1 Direct Measurement Method

For the direct measurement method, we need the value of $K'(s)$ (or $\sin \psi(s)$), and $T(s)$. Since these observables are all functions of arc length s , we need a set of data

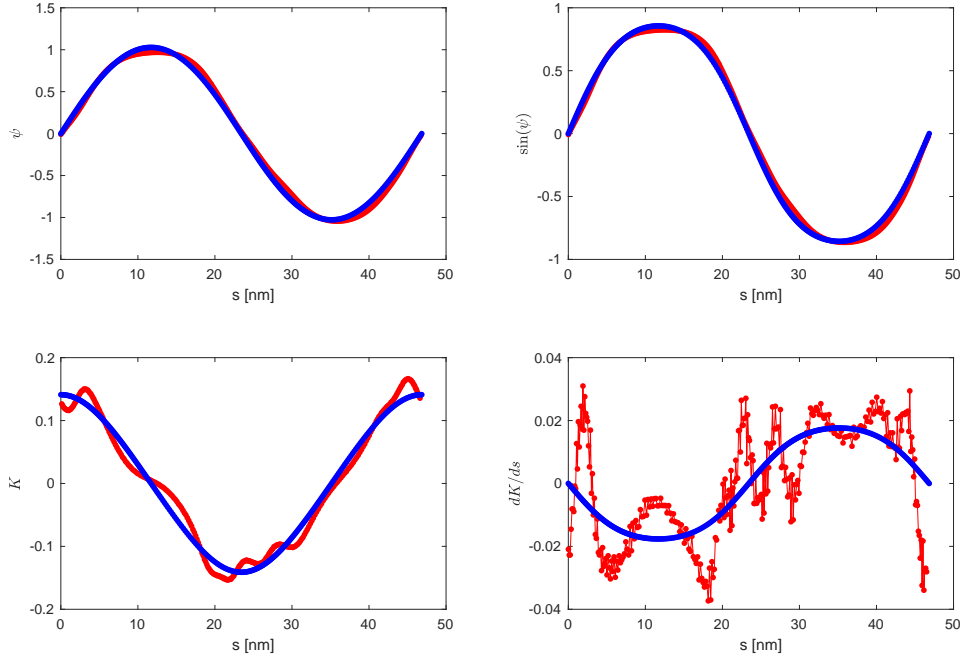


Figure 4.2: A typical example of the buckle simulation result. This example corresponds to a snapshot from a $\gamma = 0.25$ system using MARTINI DMPC, and all blue lines are the theoretical prediction on an ideal symmetrical Euler buckle, while the red lines are the actual simulation results. All horizontal axes are arc length s .

points for each individual variable.

Based on the shape analysis in Chapter 3, we know the angle $\psi(s)$, both the expression for an ideal Euler buckle, and the actual simulation situation. It is in principle easy to get $K' = d^2\psi/d^2s$, the second derivative of ψ , and $\sin\psi$, the sine function of ψ . A typical result is shown in Figure 4.2: all blue lines are theoretical predictions of an Euler buckle, while all red lines are the actual simulation results. As we can see, both ψ and $\sin\psi$ agree with the prediction very well. For the slope K and K' , due to the inherent deficit of numerical derivation, we suffer more wiggling structure and discontinuities.

So far, even though K' is not a good variable to estimate, $\sin\psi$ still remains a promising candidate. After measuring the tilt field T , Equation (4.18) will permit us to determine the tilt modulus.

The tilt field $T(s)$ in simulation, however, has a lot of noises. Figure 4.3 illustrates

one such example. In the left figure, the red dots are the local normal vector direction from fitting the curve shape, and each blue dot represents one lipid’s direction. The whole system follows the periodic boundary condition in both x and z direction. We can see that the lipids’ directions fluctuate around the normal vector. (Actually, the whole point is that they fluctuate around some direction close to the local normal vector.) In order to better evaluate the tilt field, we divide the arc length into 10 evenly spaced bins, $[s_{\min}, s_{\min} + d], \dots, [s_{\max} - d, s_{\max}]$, where $d = (s_{\max} - s_{\min})/10$. We assume lipids within the same bin have the same tilt field, and by binning, we can check the rough shape of the function $T(s)$, which is the red line in the right figure. Besides the red error bar plot, the blue dots are the distribution of $T(s)$ and the blue curve is the theoretical prediction of $T(s)$. The error bar for each bin is at the order of 20, and is *much* larger than the actual value (of order 1), or the theoretical prediction (around 1).

An obvious choice to reduce the error bar is averaging, and this is also why we do the binning in the first place. One might suggest averaging over different snap shots of the same system as it evolves. However, this is equivalent to averaging the shape of the buckle, which is a tricky and questionable thing to do, considering the buckle moves freely in the water instead of fluctuating from a fixed shape.

Another factor worth mentioning is the strategy of deciding the lipid direction. The tilt field itself is directly related to the lipid direction, but as we have mentioned in Section 3.4, there is no obvious (let alone unique) way to define a lipid’s direction. Previous publications show no agreement of a standard routine determining the director \mathbf{n} , and most of the time, even the reason behind choosing one method over another is not illustrated. May *et al.* apply four different strategies based on the idea of a two point determination: one point represents the head part, and another point represents the tail part [87]. Levine *et al.* [71] also apply three different strategies when measuring the tilt modulus, and the details of which we will revisit in the discussion section.

Among all these choices, one simple way to verify if certain choices are reliable is to compare the final results of various methods. This is precisely what we have done when we estimated the value of z_0 . It turns out that with respect to the pivotal plane location calculation, all methods agreed with each other very well. This showed that our results are hardly affected by such choices.

For the tilt field situation, however, the problem is not the bias, but the variance of our estimator of \mathbf{n} , or $T(s)$. In other words, unless a certain choice can significantly reduce the error of the tilt field $T(s)$, no choice is a “good” choice here. In fact, this large variance emerges from the disorder of the lipid matrix itself, rather than the analysis techniques, hence it is hard to get around the problem by a clever lipid di-

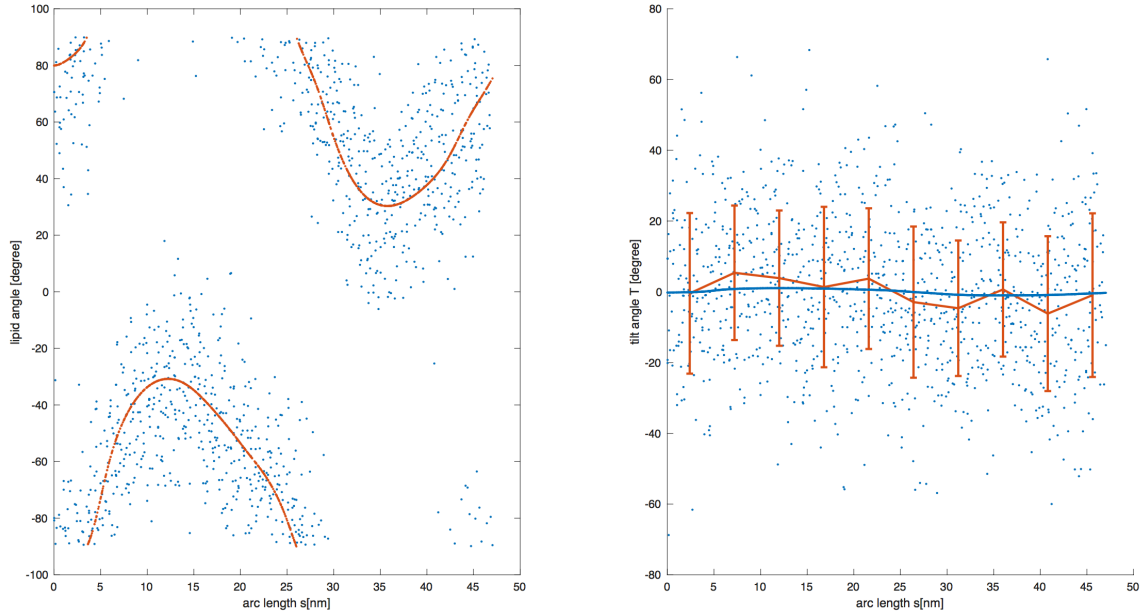


Figure 4.3: Left figure: the red lines represent the local normal vector as the angle from the horizontal direction, while the blue dots represent the angle of each lipid. Right figure: the blue dots are the tilt angle (angle between lipids and local normal) for each lipid. The blue line is the theoretical prediction for an ideal Euler buckle, which the red data points together with the error bars, result from binning the blue dots into 10 evenly spaced bins along the arc length s .

rection calculation method. It turns out that this is the case: we tried five strategies, including four strategies from Kopelevich’s group [87] and another one from glycerol backbone to the center of mass of the whole lipid. All of them give a similarly large variance.

From the above analysis, we have shown that the direct measurement might not be a feasible option for calculating the tilt modulus, because the tilt field’s inherent noise is too large compared to its actual value. The other method, however, only requires the analysis of the shape, and no investigation of the tilt field is needed.

4.3.2 Geometrical Analysis Method

To calculate the monolayer tilt modulus from Equation (4.33), we need to know (a) the monolayer bending modulus κ_m and (b) the slope of the line $z_0(\xi)$. For all three models we have previously calculated the bilayer bending modulus κ via the buckling protocol [57]. For the monolayer, $\kappa_m = \kappa/2$. The slope of $z_0(\xi)$ can be extracted from the $z_0(\xi)$ against ξ plot, which has been done in the last chapter.

Model	$\kappa_m [k_B T]$	$\ell [\text{nm}]$	$\left(\frac{2\pi\ell}{L}\right)^2$	$\theta_{\max}(\gamma = \frac{1}{4})$	$\kappa_{t,m} [\frac{\text{pN}}{\text{nm}}]$
Cooke	6.4(2)*	1.32(22)	0.0156(51)	0.85(28)°	14.4±4.6
MARTINI	14.5(5)*	1.008(34)	0.0184(12)	1.008(66)°	57.4±3.0
Berger	12.4(5)*	1.609(43)	0.0665(36)	3.64(20)°	19.4±1.0

Table 4.2: Results for all simulations analyzed in this work. To ease notation, we choose the Cooke-model generic parameters to be $\sigma = 1 \text{ nm}$ and $k_B T = 1.1 \epsilon = 4.1 \text{ pN nm}$. Values with an asterisk have been previously determined in Ref. [57],

Before we discuss the specifics of all three models, the whole results are summarized in Table 4.2.

Cooke model

The Cooke model only has three beads per lipid, and hence the function $z_0(\xi)$ only has three points for any value of γ . (Figure 3.12) Moreover, as we have discussed in Section 3.5.1, since the $z_0(\xi)$ value corresponding to the head bead is significantly lower than for the other two beads, a linear fit is generally a statistically implausible description of these three points. However, a line drawn through the two points belonging to the two tail beads yields consistent values for the slope. This might sound trivial, since one can always draw a line through two points, but “consistency” here means that the slope is consistent for all values of the strain γ , a finding that would not have to hold, and which in fact does *not* hold if we were to fit a line through all three points.

Figure 4.4 shows the value of the tilt modulus $\kappa_{t,m}$ inferred via Equation (4.33), plotted against all simulated strains γ . The result averaged over all simulations gives $\kappa_{t,m} = (3.5 \pm 1.1) k_B T / \sigma^2$. With the mapping $\sigma = 1 \text{ nm}$ and $k_B T = 1.1 \epsilon = 4.1 \text{ pN nm}$, this gives $\kappa_{t,m} = (14.4 \pm 4.6) \text{ pN/nm}$. The error is fairly large, since the two available points do not constrain the slope of $z_0(\xi)$ very precisely. The tilt decay length is found to be $\ell \approx 1.3 \text{ nm}$ and is hence clearly microscopic. For a strain of 25% the inferred maximum tilt angle is 0.85° and thus very small.

MARTINI model

The MARTINI model for DMPC contains 10 CG beads, and this offers a broader basis for estimating the slope of $z_0(\xi)$. Moreover, unlike in the Cooke model case, all points lie plausibly on a single line (Figure 3.15). There are still small system-

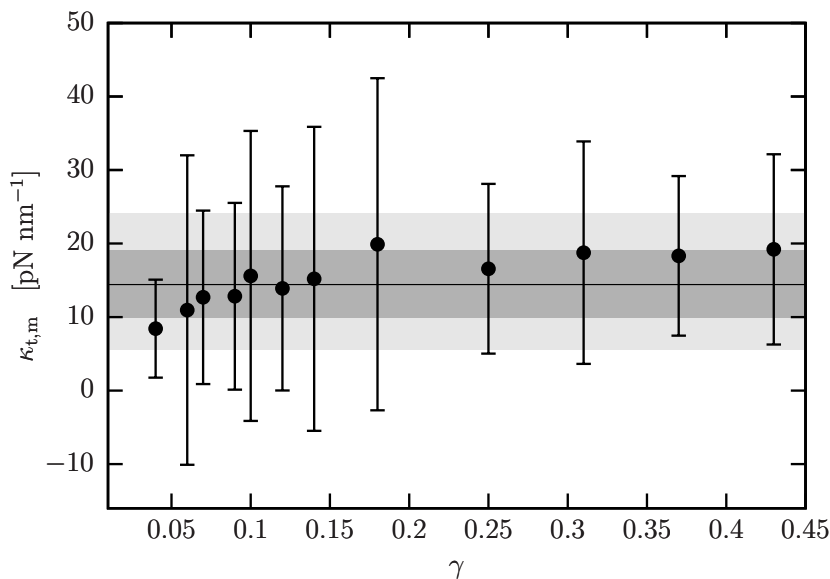


Figure 4.4: Value of the tilt modulus $\kappa_{t,m}$ for the Cooke model against strain γ . The shaded regions are the 1σ and 2σ confidence bands when fitting to a constant.

atic effects, this time related to the fact that the inferred z_0 values belonging to the beads of the *sn1*-chain are slightly smaller (by about 0.01 nm) than those inferred from the *sn2*-chain. Figure 4.5 shows the values of the tilt modulus inferred from the slope in such graphs for all values of γ studied. Averaging the data, we find $\kappa_{t,m} = (57.4 \pm 3.0)\text{pN/nm}$, and a tilt decay length of $\ell \approx 1.0\text{ nm}$. The maximum inferred tilt angle at $\gamma = 25\%$ is found to be 1° , again very small.

Unlike for the Cooke data, the MARTINI results for $\kappa_{t,m}(\gamma)$ are precise enough to see that the γ -dependent correction in Equation (4.33) is crucial in order to get strain-independent values of the tilt modulus. This nontrivial correction illustrates that our theory describes the data well, despite several approximations, of which the two most important ones were the use of a simplified Euler Lagrange equation (4.23) for connecting tilt and shape and the replacement $\sin \psi \rightarrow \psi$ in Equation (4.29) to ease including tilt in the lipid-imbalance equation.

Berger model

For the Berger model, Figure 3.17 shows that the function $z_0(\langle \xi_i \rangle)$ is no longer a simple line. The slope of this plot is now an ill-defined quantity. In the Discussion section we will reflect on some further implications of this result. For now, a pragmatic but plausible way forward is to observe that *within the tail-region of the lipid* the relation

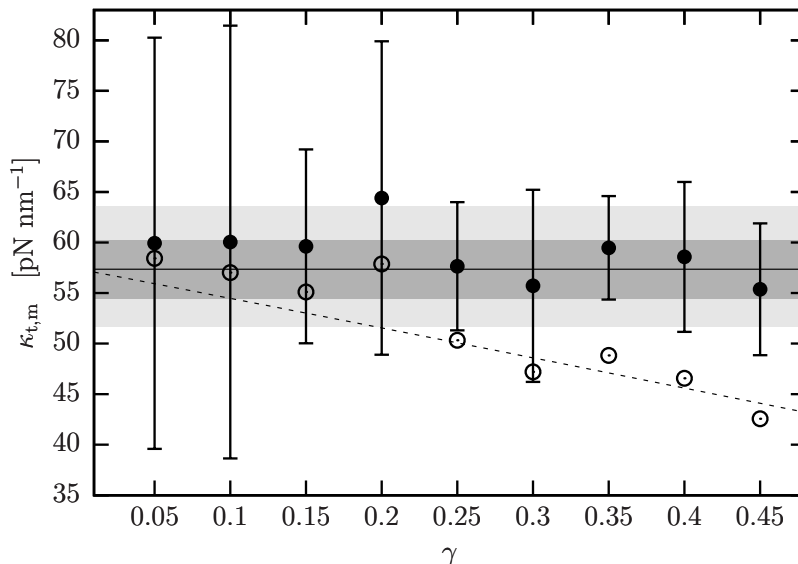


Figure 4.5: Value of the tilt modulus $\kappa_{t,m}$ for the MARTINI model against strain γ . The filled symbols are determined from Equation (4.33); the open symbols are calculated without the strain correction factor of $1 + \frac{1}{2}\gamma + \frac{9}{32}\gamma^2 + \dots$, showing that the latter is needed to arrive at a result that is no longer strain dependent. The shaded regions are the 1σ and 2σ confidence bands when fitting the filled data points to a constant.

between z_0 and the distance $\langle \xi_i \rangle$ of a reference atom away from the bilayer’s midplane is still linear, and so we will define the slope of $z_0(\xi)$ only with this subset of atoms. This means that, as far as tilt is concerned, *we restrict our analysis to the tails*.

Figure 4.6 shows the values of the thus-inferred tilt modulus against all investigated values of the strain γ . Averaging over all strains, we get $\kappa_{t,m} = (19.4 \pm 1.0)$ pN/nm, which is about three times smaller than the value inferred from the CG MARTINI version of DMPC. In contrast, the tilt decay length is fairly similar, $\ell \approx 1.3$ nm. Notice that the small value of the modulus also renders the maximum tilt angle bigger: we find $\theta_{\max}(\gamma = \frac{1}{4}) = 3.67^\circ$, almost 4 times the maximum value for MARTINI under the same conditions.

4.4 Discussion

4.4.1 Comparison with previous work

The tilt moduli of several different atomistic lipid models have recently been determined in simulations, relying on a spectral analysis of lipid orientation in a (possibly

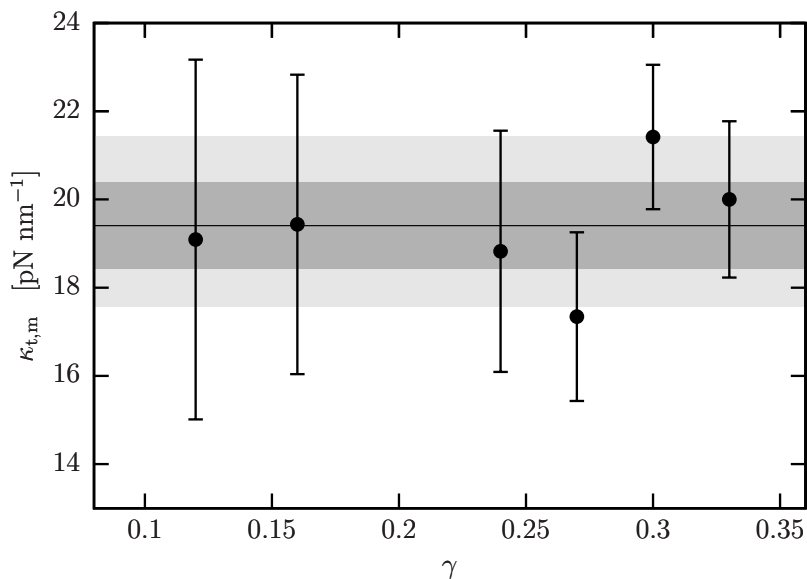


Figure 4.6: Value of the tilt modulus $\kappa_{t,m}$ for the Berger DMPC model against strain γ . The shaded regions are the 1σ and 2σ confidence bands when fitting to a constant.

quite small) flat bilayer [71, 140]. Also, a first experimental measurement has been presented, which analyzed membrane undulations at large wave vectors [59]. We are going to compare our result with these values.

The only experimentally available tilt modulus before our initial publication was published by Jablin et al. [59], who found (95 ± 7) pN/nm—albeit for the lipid DOPC. As far as simulations are concerned, Watson et al. have determined the tilt modulus of Berger-DMPC at 303K by measuring transverse lipid orientation fluctuations, finding $\kappa_t = 56$ pN/nm [143]. Using the same technique, but the CHARMM 36 force field for DMPC, Venable et al. have found $\kappa_t = 40.2$ pN/nm [140]. Our own value of $\kappa_t = (38.8 \pm 2)$ pN/nm is of quite comparable magnitude. In fact, Venable et al. studied twelve common lipids and found values in the range $40 \dots 85$ pN/nm. The fact that our value is slightly smaller than Venables might be attributable to the slight difference in temperature, according to the temperature dependence of the DMPC tilt modulus as recently published in Ref. [96]. In fact, this publication also explicitly measured the DMPC tilt modulus and found (44 ± 2) pN/nm, which agrees excellently with our value determined from the Berger force field.

Previous measurements of the tilt modulus of MARTINI DMPC do not yet appear to exist, but Watson *et al.* have measured the tilt modulus of MARTINI DPPC [81], which differs by having one extra CG bead per chain. They find $\kappa_t = 110$ pN/nm, about a factor of 2 larger than their Berger DMPC value. Our own value for MAR-

TINI DMPC, $\kappa_t = (115 \pm 6)$ pN/nm is about a factor 3 larger than the united atom Berger value. Both measurements suggest that MARTINI lipids tilt less easily than the more highly resolved united atom models.

In their investigation of bending and tilt moduli through lipid orientation fluctuations, Levine *et al.* point out that the value for the tilt modulus may shift by up to $\pm 20\%$ depending on how they define the lipid director [71]. In the supplementary material to their publication they compare three different definitions. While they all use the midpoint between the terminal methyls of the two tails as one anchor point, they differ in the choice of the other anchor point: either the phosphate atom, or the glycerol C₂ atom, or the midpoint between those two (the latter is the authors' preferred choice). They find that the inferred tilt modulus increases as one moves the upper reference point further out. Our own studies suggest an explanation of this finding. Recall from Fig. 3.17 that $z_0(\xi)$ is not simply a straight line, the shape which our theory predicts under the assumption that the lipids tilt uniformly. Instead, the slope decreases beyond the glycerol backbone and even becomes negative. This clearly shows that the head of the lipid does not participate in tilting to the same extent as the tails do. Had we described the lipid by a simple line between two reference points, then the resulting slope in $z_0(\xi)$ would be smaller the higher up the head-group choice is taken. But from Equation (4.33), smaller slopes result in bigger moduli, and so we recover the same trend as Levine *et al.* do.

4.4.2 Physical meaning behind the non-linearity of the Berger model

The non-uniform tilting of lipids is more than a nuisance for defining the orientation. It reminds us that the notion of lipid tilt is more subtle than simply a rotation of the lipid without a change of its shape. Interestingly, our own analysis never requires us to define an orientation vector, and so we can empirically test whether or not lipids tilt uniformly—concluding that they do not. Moreover, the data suggest that the tail region of lipids shows a clean linear trend in $z_0(\xi)$, suggesting that the tails *do* tilt uniformly, while the head group shows a more complex behavior. One might be tempted to define a *local* tilt modulus along the height of the lipid, via the local slope of $z_0(\xi)$, but notice that this would give an infinite modulus at the point where $z_0(\xi)$ has its maximum (roughly at $\xi = 1.6$ nm, where the C₃ atom of the glycerol backbone sits). We instead prefer to define a tilt modulus for the tail region alone (since it is well-defined). This also means that our effective lipid orientation is more tilted than the one which Levine *et al.* infer from their preferred choice [71], which is one possible reason for why our tilt modulus is slightly smaller than theirs.

4.5 Summary

In this chapter, we have shown that the buckling configuration and an analysis process similar to Chapter 3, can not only provide the pivotal plane information, but also give us access to another important elastic property, the tilt modulus. Just as in the last chapter, we applied our method to three coarse-grained models with different resolutions. For MARTINI DMPC and Berger DMPC we find values for the moduli which are compatible (within the scatter still common for simulations of moduli) with other simulations that use very different techniques relying on a fluctuation analysis. For the highly coarse-grained Cooke model no numbers for comparison existed, but the results for maximum tilt angle and tilt decay length are very similar to the other two models, especially MARTINI.

We find that MARTINI DMPC resists titling more strongly than a more finely resolved united atom model of DMPC. Moreover, analysis of the latter model suggests that these lipids do not tilt uniformly, only the tails do. Hence, the definition of tilt becomes less obvious, as previously noted [71], but our analysis strategy does not have to commit to a specific definition of the tilt direction, since it instead backs out the extent of local tilt from the data.

Bibliography

- [1] Echelon Incproduct details for 1,2-dimyristoyl-sn-glycero-3-phosphocholine. <http://www.echelon-inc.com/content/EBI/product/images/762.gif>.
- [2] Introduction to life science. <http://csls-text2.c.u-tokyo.ac.jp>.
- [3] Wikipedia:poisson's ratio. <https://en.wikipedia.org/wiki/Poisson>
- [4] Milton Abramowitz and Irene A. Stegun. *Handbook of Mathematical Functions: With Formulas, Graphs, and Mathematical Tables*. Dover, New York, 9 edition, 1972.
- [5] H. J. C Berendsen, J. P. M Postma, W. F van Gunsteren, A. DiNola, and J. R Haak. Molecular dynamics with coupling to an external bath. *J. Chem. Phys.*, 81(8):3684–3690, 1984.
- [6] Oliver Berger, Olle Edholm, and Fritz Jähnig. Molecular dynamics simulations of a fluid bilayer of dipalmitoylphosphatidylcholine at full hydration, constant pressure, and constant temperature. *Biophysical journal*, 72(5):2002, 1997.
- [7] Eva Bianconi, Allison Piovesan, Federica Facchin, Alina Beraudi, Raffaella Casadei, Flavia Frabetti, Lorenza Vitale, Maria Chiara Pelleri, Simone Tasani, Francesco Piva, et al. An estimation of the number of cells in the human body. *Annals of human biology*, 40(6):463–471, 2013.
- [8] B Bozic, Sasa Svetina, Bostjan Zeks, and RE Waugh. Role of lamellar membrane structure in tether formation from bilayer vesicles. *Biophysical journal*, 61(4):963, 1992.
- [9] Erik G. Brandt, Anthony R. Braun, Jonathan N. Sachs, John F. Nagle, and Olle Edholm. Interpretation of fluctuation spectra in lipid bilayer simulations. *Biophys. J.*, 100(9):2104–2111, 2011.
- [10] F Brochard and JF Lennon. Frequency spectrum of the flicker phenomenon in erythrocytes. *Journal de Physique*, 36(11):1035–1047, 1975.
- [11] Dirk Jan Bukman, Jian Hua Yao, and Michael Wortis. Stability of cylindrical vesicles under axial tension. *Phys. Rev. E*, 54:5463–5468, 1996.

- [12] Felix Campelo, Clement Arnarez, Siewert J Marrink, and Michael M Kozlov. Helfrich model of membrane bending: from gibbs theory of liquid interfaces to membranes as thick anisotropic elastic layers. *Advances in colloid and interface science*, 208:25–33, 2014.
- [13] Peter B Canham. The minimum energy of bending as a possible explanation of the biconcave shape of the human red blood cell. *Journal of theoretical biology*, 26(1):61–81, 1970.
- [14] Riccardo Capovilla, Jemal Guven, and Jose’Antonio Santiago. Deformations of the geometry of lipid vesicles. *Journal of Physics A: Mathematical and General*, 36(23):6281, 2003.
- [15] Z. Chen and R. P. Rand. The influence of cholesterol on phospholipid membrane curvature and bending elasticity. *Biophys. J.*, 73(1):267–276, 1997.
- [16] Z. Chen and R. P. Rand. Comparative Study of the Effects of Several n -Alkanes on Phospholipid Hexagonal Phases. *Biophys. J.*, 74(2):944–952, 1998.
- [17] Shiing-shen Chern. A simple intrinsic proof of the gauss-bonnet formula for closed riemannian manifolds. *Annals of mathematics*, pages 747–752, 1944.
- [18] LV Chernomordik, MM Kozlov, GB Melikyan, IG Abidor, VS Markin, and Yu A Chizmadzhev. The shape of lipid molecules and monolayer membrane fusion. *Biochimica et Biophysica Acta (BBA)-Biomembranes*, 812(3):643–655, 1985.
- [19] Ira R. Cooke and Markus Deserno. Solvent-free model for self-assembling fluid bilayer membranes: Stabilization of the fluid phase based on broad attractive tail potentials. *J. Chem. Phys.*, 123(22):224710, 2005.
- [20] Ira R. Cooke and Markus Deserno. Coupling between lipid shape and membrane curvature. *Biophys. J.*, 91(2):487–495, 2006.
- [21] Ira R. Cooke, Kurt Kremer, and Markus Deserno. Tunable generic model for fluid bilayer membranes. *Phys. Rev. E*, 72(1):011506, 2005.
- [22] N Dan and SA Safran. Effect of lipid characteristics on the structure of trans-membrane proteins. *Biophysical Journal*, 75(3):1410–1414, 1998.
- [23] William HE Day and Herbert Edelsbrunner. Efficient algorithms for agglomerative hierarchical clustering methods. *Journal of classification*, 1(1):7–24, 1984.
- [24] Carl De Boor, Carl De Boor, Etats-Unis Mathématicien, Carl De Boor, and Carl De Boor. *A practical guide to splines*, volume 27. Springer-Verlag New York, 1978.

- [25] Laura Dean. Blood groups and red cell antigens, chapter 1, blood and the cells it contains, 2005.
- [26] Markus Deserno. Fluid lipid membranes—a primer. http://www.cmu.edu/biolphys/deserno/pdf/membrane_theory.pdf, 2007.
- [27] Markus Deserno. Fluid lipid membranes: From differential geometry to curvature stresses. *Chemistry and physics of lipids*, 185:11–45, 2015.
- [28] Manfredo do Carmo. *Differential Geometry of Curves and Surfaces*. Prentice Hall, Englewood Cliffs, NJ, 1976.
- [29] Manfredo Perdigao Do Carmo and Manfredo Perdigao Do Carmo. *Differential geometry of curves and surfaces*, volume 2. Prentice-hall Englewood Cliffs, 1976.
- [30] Michael Edidin. Lipids on the frontier: a century of cell-membrane bilayers. *Nature Reviews Molecular Cell Biology*, 4(5):414–418, 2003.
- [31] E Evans and A Yeung. Mechanics of cell deformation: Relation to cell division. In *Biomechanics of cell division*, pages 161–185. Springer, 1987.
- [32] Evan Evans and David Needham. Physical properties of surfactant bilayer membranes: thermal transitions, elasticity, rigidity, cohesion and colloidal interactions. *Journal of Physical Chemistry*, 91(16):4219–4228, 1987.
- [33] Evan A Evans. Bending resistance and chemically induced moments in membrane bilayers. *Biophysical journal*, 14(12):923, 1974.
- [34] Evan A Evans. Minimum energy analysis of membrane deformation applied to pipet aspiration and surface adhesion of red blood cells. *Biophysical journal*, 30(2):265, 1980.
- [35] Evan A Evans, Richard Skalak, and S Weinbaum. Mechanics and thermodynamics of biomembranes, 1980.
- [36] JF Faucon, MD Mitov, P Méléard, I Bivas, and P Bothorel. Bending elasticity and thermal fluctuations of lipid membranes. theoretical and experimental requirements. *Journal de physique*, 50(17):2389–2414, 1989.
- [37] Henrik Flyvbjerg and Henrik Gordon Petersen. Error estimates on averages of correlated data. *The Journal of Chemical Physics*, 91(1):461–466, 1989.
- [38] Toshizumi Fukui and Masaru Hasegawa. Singularities of parallel surfaces. *Tohoku Math. J.*, 64(3):387–408, 2012.
- [39] N. Fuller and R. P. Rand. The Influence of Lysolipids on the Spontaneous Curvature and Bending Elasticity of Phospholipid Membranes. *Biophys. J.*, 81(1):243–254, 2001.

- [40] Jordi Gómez-Llobregat, Federico Elías-Wolff, and Martin Lindén. Anisotropic membrane curvature sensing by antibacterial peptides. *arXiv preprint arXiv:1412.2371*, 2014.
- [41] Gerhard Gompper and Stefan Klein. Ginzburg-landau theory of aqueous surfactant solutions. *J. Phys. II (France)*, 2:1725–1744, 1992.
- [42] James Edward Gordon. *Structures, or, Why things don't fall down*. Da Capo Press, 2003.
- [43] Gary S Grest and Kurt Kremer. Molecular dynamics simulation for polymers in the presence of a heat bath. *Phys. Rev. A*, 33(5):3628, 1986.
- [44] M Hamm and MM Kozlov. Tilt model of inverted amphiphilic mesophases. *The European Physical Journal B-Condensed Matter and Complex Systems*, 6(4):519–528, 1998.
- [45] M Hamm and MM Kozlov. Elastic energy of tilt and bending of fluid membranes. *The European Physical Journal E*, 3(4):323–335, 2000.
- [46] Vagelis A. Harmandaris and Markus Deserno. A novel method for measuring the bending rigidity of model lipid membranes by simulating tethers. *J. Chem. Phys.*, 125(20):204905, 2006.
- [47] W Helfrich. Blocked lipid exchange in bilayers and its possible influence on the shape of vesicles. *Zeitschrift für Naturforschung C*, 29(9-10):510–515, 1974.
- [48] Wolfgang Helfrich. Elastic properties of lipid bilayers: theory and possible experiments. *Zeitschrift für Naturforschung C*, 28(11-12):693–703, 1973.
- [49] Wolfgang Helfrich. Amphiphilic mesophases made of defects. In R. Balian, M. Kléman, and J. P. Poirier, editors, *Physics of Defects*, pages 715–755. North-Holland, Amsterdam, 1981.
- [50] Wolfgang Helfrich. Lyotropic lamellar phases. *J. Phys. Condens. Matt.*, 6:A79–A92, 1994.
- [51] Berk Hess, Carsten Kutzner, David Van Der Spoel, and Erik Lindahl. GRO-MACS 4: algorithms for highly efficient, load-balanced, and scalable molecular simulation. *J. Chem. Theory Comput.*, 4(3):435–447, 2008.
- [52] F. M. Hochmuth, J. Y. Shao, J. Dai, and M. P. Sheetz. Deformation and flow of membrane into tethers extracted from neuronal growth cones. *Biophys. J.*, 70(1):358–369, 1996.
- [53] William G. Hoover. Canonical dynamics: Equilibrium phase-space distributions. *Phys. Rev. A*, 31(3):1695–1697, 1985.

- [54] Mingyang Hu. *Designing polymer-tethered membrane-nanoparticle composites*. PhD thesis, Carnegie Mellon University, 2013.
- [55] Mingyang Hu, John J. Briguglio, and Markus Deserno. Determining the Gaussian curvature modulus of lipid membranes in simulations. *Biophys. J.*, 102(6):1403–1410, 2012.
- [56] Mingyang Hu, Djurre H. de Jong, Siewert J. Marrink, and Markus Deserno. Gaussian curvature elasticity determined from global shape transformations and local stress distributions: a comparative study using the MARTINI model. *Faraday Discuss.*, 161:365–382, 2013.
- [57] Mingyang Hu, Patrick Diggins IV, and Markus Deserno. Determining the bending modulus of a lipid membrane by simulating buckling. *The Journal of chemical physics*, 138(21):214110, 2013.
- [58] Jacob N Israelachvili, D John Mitchell, and Barry W Ninham. Theory of self-assembly of hydrocarbon amphiphiles into micelles and bilayers. *Journal of the Chemical Society, Faraday Transactions 2: Molecular and Chemical Physics*, 72:1525–1568, 1976.
- [59] M. S. Jablin, K. Akabori, and J. F. Nagle. Experimental support for tilt-dependent theory of biomembrane mechanics. *Phys. Rev. Lett.*, 113:248102, 2014.
- [60] Martin Karplus and J Andrew McCammon. Molecular dynamics simulations of biomolecules. *Nature Structural & Molecular Biology*, 9(9):646–652, 2002.
- [61] Dr. Richard Kessel. Red blood cells.
- [62] MM Kozlov, SL Leikin, and VS Markin. Elastic properties of interfaces. elasticity moduli and spontaneous geometric characteristics. *Journal of the Chemical Society, Faraday Transactions 2: Molecular and Chemical Physics*, 85(4):277–292, 1989.
- [63] MM Kozlov and M Winterhalter. Elastic moduli for strongly curved monolayers. position of the neutral surface. *Journal de Physique II*, 1(9):1077–1084, 1991.
- [64] Yonathan Kozlovsky and Michael M Kozlov. Stalk model of membrane fusion: solution of energy crisis. *Biophysical Journal*, 82(2):882–895, 2002.
- [65] Yonathan Kozlovsky and Michael M Kozlov. Membrane fission: model for intermediate structures. *Biophysical journal*, 85(1):85–96, 2003.

- [66] Yonathan Kozlovsky, Joshua Zimmerberg, and Michael M Kozlov. Orientation and interaction of oblique cylindrical inclusions embedded in a lipid monolayer: a theoretical model for viral fusion peptides. *Biophysical journal*, 87(2):999–1012, 2004.
- [67] Vera Kralj-Iglič, Saša Svetina, and Boštjan Žekš. The existence of non-axisymmetric bilayer vesicle shapes predicted by the bilayer couple model. *European biophysics journal*, 22(2):97–103, 1993.
- [68] Peter I Kuzmin, Sergey A Akimov, Yuri A Chizmadzhev, Joshua Zimmerberg, and Fredric S Cohen. Line tension and interaction energies of membrane rafts calculated from lipid splay and tilt. *Biophysical journal*, 88(2):1120–1133, 2005.
- [69] LD Landau and EM Lifshitz. *Theory of elasticity*, Butterworth-Heinemann, 1999.
- [70] S Leikin, M M Kozlov, N L Fuller, and R P Rand. Measured effects of diacylglycerol on structural and elastic properties of phospholipid membranes. *Biophysical Journal*, 71(5):2623–2632, November 1996.
- [71] Zachary A. Levine, Richard M. Venable, Max C. Watson, Michael G. Lerner, Joan-Emma Shea, Richard W. Pastor, and Frank L. H. Brown. Determination of biomembrane bending moduli in fully atomistic simulations. *J. Am. Chem. Soc.*, 136(39):13582–13585, 2014.
- [72] Zachary A Levine, Richard M Venable, Max C Watson, Michael G Lerner, Joan-Emma Shea, Richard W Pastor, and Frank LH Brown. Determination of biomembrane bending moduli in fully atomistic simulations. *Journal of the American Chemical Society*, 136(39):13582–13585, 2014.
- [73] Hans-Jörg Limbach, Axel Arnold, Bernward A. Mann, and Christian Holm. ESPRESSO – an extensible simulation package for research on soft matter systems. *Comput. Phys. Commun.*, 174(9):704–727, 2006.
- [74] Reinhard Lipowsky. The conformation of membranes. *Nature*, 349(6309):475–481, 1991.
- [75] Bin Liu, Matthew I Hoopes, and Mikko Karttunen. Molecular Dynamics Simulations of DPPC/CTAB Monolayers at the Air/Water Interface. *J. Phys. Chem. B*, 118(40):11723–11737, 2014.
- [76] H Lodish, A Berk, P Matsudaira, CA Kaiser, M Krieger, et al. *Molecular cell biology* wh freeman & company. 2003.
- [77] Harvey Lodish, Arnold Berk, S Lawrence Zipursky, Paul Matsudaira, David Baltimore, and James Darnell. *Neurotransmitters, synapses, and impulse transmission*. 2000.

- [78] TC Lubensky and FC MacKintosh. Theory of ripple phases of lipid bilayers. *Physical review letters*, 71(10):1565, 1993.
- [79] Siewert J Marrink, Alex H De Vries, and Alan E Mark. Coarse grained model for semiquantitative lipid simulations. *The Journal of Physical Chemistry B*, 108(2):750–760, 2004.
- [80] Siewert J Marrink, H Jelger Risselada, Serge Yefimov, D Peter Tieleman, and Alex H De Vries. The martini force field: coarse grained model for biomolecular simulations. *The Journal of Physical Chemistry B*, 111(27):7812–7824, 2007.
- [81] Siewert J. Marrink, H. Jelger Risselada, Serge Yefimov, D. Peter Tieleman, and Alex H. De Vries. The MARTINI force field: coarse grained model for biomolecular simulations. *J. Phys. Chem. B*, 111(27):7812–7824, 2007.
- [82] Siewert J Marrink and D Peter Tieleman. Perspective on the martini model. *Chemical Society Reviews*, 42(16):6801–6822, 2013.
- [83] Derek Marsh. Elastic curvature constants of lipid monolayers and bilayers. *Chem. Phys. Lipids*, 144(2):146–159, 2006.
- [84] Derek Marsh. Lateral pressure profile, spontaneous curvature frustration, and the incorporation and conformation of proteins in membranes. *Biophys. J.*, 93(11):3884–3899, 2007.
- [85] M Marsh and HT McMahon. The structural era of endocytosis. *Science*, 285(5425):215–220, 1999.
- [86] ER May, A Narang, and DI Kopelevich. Molecular modeling of key elastic properties for inhomogeneous lipid bilayers. *Molecular Simulation*, 33(9-10):787–797, 2007.
- [87] Eric R May, Atul Narang, and Dmitry I Kopelevich. Role of molecular tilt in thermal fluctuations of lipid membranes. *Physical Review E*, 76(2):021913, 2007.
- [88] S May. A molecular model for the line tension of lipid membranes. *The European Physical Journal E: Soft Matter and Biological Physics*, 3(1):37–44, 2000.
- [89] Sylvio May. Protein-induced bilayer deformations: the lipid tilt degree of freedom. *European Biophysics Journal*, 29(1):17–28, 2000.
- [90] Sylvio May and Avinoam Ben-Shaul. Molecular theory of lipid-protein interaction and the I α -h ii transition. *Biophysical journal*, 76(2):751–767, 1999.

- [91] Ling Miao, Udo Seifert, Michael Wortis, and Hans-Günther Döbereiner. Budding transitions of fluid-bilayer vesicles: the effect of area-difference elasticity. *Physical Review E*, 49(6):5389, 1994.
- [92] Kakoli Mitra, Iban Ubarretxena-Belandia, Tomohiko Taguchi, Graham Warren, and Donald M Engelman. Modulation of the bilayer thickness of exocytic pathway membranes by membrane proteins rather than cholesterol. *Proceedings of the National Academy of Sciences*, 101(12):4083–4088, 2004.
- [93] Martin Michael Müller, Markus Deserno, and Jemal Guven. Interface-mediated interactions between particles: a geometrical approach. *Physical Review E*, 72(6):061407, 2005.
- [94] Barbara M Mullock and J Paul Luzio. Theory of organelle biogenesis: a historical perspective. 2000.
- [95] Sureshbabu Nagarajan, Erin E. Schuler, Kevin Ma, James T Kindt, and R. Brian Dyer. Dynamics of the gel to fluid phase transformation in unilamellar DPPC vesicles. *J. Phys. Chem. B*, 116(46):13749–13756, 2012.
- [96] John F Nagle. X-ray scattering reveals molecular tilt is an order parameter for the main phase transition in a model biomembrane. *in print*.
- [97] John F Nagle. Experimentally determined tilt and bending moduli of single-component lipid bilayers. *Chemistry and Physics of Lipids*, 2017.
- [98] John F Nagle and Stephanie Tristram-Nagle. Structure of lipid bilayers. *Biochimica et Biophysica Acta (BBA)-Reviews on Biomembranes*, 1469(3):159–195, 2000.
- [99] Hiroshi Noguchi. Anisotropic surface tension of buckled fluid membranes. *Phys. Rev. E*, 83:061919, 2011.
- [100] WG Noid. Perspective: Coarse-grained models for biomolecular systems. *The Journal of chemical physics*, 139(9):090901, 2013.
- [101] S. Nosé. A molecular dynamics method for simulations in the canonical ensemble. *Mol. Phys.*, 52(2):255–268, 1984.
- [102] Shuichi Nosé and M. L. Klein. Constant pressure molecular dynamics for molecular systems. *Mol. Phys.*, 50(5):1055–1076, 1983.
- [103] O. H. Samuli Ollila. *Lateral Pressure in Lipid Membranes and Its Role in Function of Membrane Proteins*. PhD thesis, Tampere University of Technology (TUT), 2010. <http://dspace.cc.tut.fi/dpub/handle/123456789/6813>.

- [104] O. H. Samuli Ollila and Ilpo Vattulainen. Lateral pressure profiles in lipid membranes: Dependence on molecular composition. *Molecular simulations and biomembranes: from biophysics to function*, (20):26, 2010.
- [105] Samuli Ollila, Marja T. Hyvönen, and Ilpo Vattulainen. Polyunsaturation in lipid membranes: dynamic properties and lateral pressure profiles. *J. Phys. Chem. B*, 111(12):3139–3150, 2007.
- [106] Mario Orsi and Jonathan W. Essex. The ELBA Force Field for Coarse-Grain Modeling of Lipid Membranes. *Plos One*, 6(12):e28637, 2011.
- [107] Mario Orsi, David Y. Haubertin, Wendy E. Sanderson, and Jonathan W. Essex. A quantitative coarse-grain model for lipid bilayers. *J. Phys. Chem. B*, 112(3):802–815, 2008.
- [108] Mario Orsi, Julien Michel, and Jonathan W Essex. Coarse-grain modelling of DMPC and DOPC lipid bilayers. *J. Phys.: Condensed. Matt.*, 22(15):155106, 2010.
- [109] M. Parrinello and A. Rahman. Polymorphic transitions in single crystals: A new molecular dynamics method. *J. Appl. Phys.*, 52(12):7182–7190, 1981.
- [110] JR Philip. Osmosis and diffusion in tissue: Half-times and internal gradients. *Plant Physiology*, 33(4):275, 1958.
- [111] Rob Phillips, Jane Kondev, Julie Theriot, and Hernan Garcia. *Physical biology of the cell*. Garland Science, 2012.
- [112] Siméon Denis Poisson and Jean-Guillaume Garnier. *Traité de mécanique*. Société belge de librairie, 1838.
- [113] Thomas Powers and Philip Nelson. Fluctuating membranes with tilt order. *Journal de Physique II*, 5(11):1671–1678, 1995.
- [114] William A Prinz. Lipid trafficking sans vesicles: where, why, how? *Cell*, 143(6):870–874, 2010.
- [115] R. P. Rand, N. L. Fuller, S. M. Gruner, and V. A. Parsegian. Membrane curvature, lipid segregation, and structural transitions for phospholipids under dual-solvent stress. *Biochem.*, 29(1):76–87, 1990.
- [116] RP Rand and NL Fuller. Structural dimensions and their changes in a reentrant hexagonal-lamellar transition of phospholipids. *Biophysical journal*, 66(6):2127–2138, 1994.

- [117] W Rawicz, KC Olbrich, T McIntosh, D Needham, and E Evans. Effect of chain length and unsaturation on elasticity of lipid bilayers. *Biophysical journal*, 79(1):328–339, 2000.
- [118] Robert Rosen. *Optimality principles in biology*. Springer, 2013.
- [119] Th Rosenberg. On accumulation and active transport in biological systems. 1. thermodynamic considerations. *Acta Chemica Scandinavica*, 2(1):14–33, 1948.
- [120] Andrzej J. Rzepiela, Lars V. Schäfer, Nicolae Goga, H. Jelger Risselada, Alex H. De Vries, and Siewert J. Marrink. Reconstruction of atomistic details from coarse-grained structures. *J. Comput. Chem.*, 31(6):1333–1343, 2010.
- [121] O H Samuli Ollila, Tomasz Róg, Mikko Karttunen, and Ilpo Vattulainen. Role of sterol type on lateral pressure profiles of lipid membranes affecting membrane protein functionality: Comparison between cholesterol, desmosterol, 7-dehydrocholesterol and ketosterol. *J. Struct. Biol.*, 159(2):311–323, 2007.
- [122] MB Schneider, JT Jenkins, and WW Webb. Thermal fluctuations of large quasi-spherical bimolecular phospholipid vesicles. *Journal de Physique*, 45(9):1457–1472, 1984.
- [123] U Seifert and R Lipowsky. Morphology of vesicles. *Handbook of biological physics*, 1:403–464, 1995.
- [124] Udo Seifert. Configurations of fluid membranes and vesicles. *Advances in physics*, 46(1):13–137, 1997.
- [125] Udo Seifert, Ling Miao, H-G Döbereiner, and Michael Wortis. Budding transition for bilayer fluid vesicles with area-difference elasticity. In *The structure and conformation of amphiphilic membranes*, pages 93–96. Springer, 1992.
- [126] Udo Seifert, Julian Shillcock, and Philip Nelson. Role of bilayer tilt difference in equilibrium membrane shapes. *Physical review letters*, 77(26):5237, 1996.
- [127] Ron Sender, Shai Fuchs, and Ron Milo. Revised estimates for the number of human and bacteria cells in the body. *BioRxiv*, page 036103, 2016.
- [128] David P Siegel. Energetics of intermediates in membrane fusion: comparison of stalk and inverted micellar intermediate mechanisms. *Biophysical Journal*, 65(5):2124–2140, 1993.
- [129] Lloyd Silverman and David Glick. Measurement of protein concentration by quantitative electron microscopy. *The Journal of cell biology*, 40(3):773–778, 1969.

- [130] SJ Singer and Garth L Nicolson. The fluid mosaic model of the structure of cell membranes. *Membranes and Viruses in Immunopathology; Day, SB, Good, RA, Eds*, pages 7–47, 1972.
- [131] Alexander J Sodt and Richard W Pastor. Bending Free Energy from Simulation: Correspondence of Planar and Inverse Hexagonal Lipid Phases. *Biophysj*, 104(10):2202–2211, May 2013.
- [132] Michael Spivak. *A Comprehensive Introduction to Differential Geometry*, volume 3. Publish or Perish, Boston, MA, 1975.
- [133] RP Stephenson. A modification of receptor theory. *British journal of pharmacology and chemotherapy*, 11(4):379–393, 1956.
- [134] Walther Stoeckenius and Donald M Engelman. Current models for the structure of biological membranes. *The Journal of cell biology*, 42(3):613–646, 1969.
- [135] Saša Svetina and Boštjan Žekš. Membrane bending energy and shape determination of phospholipid vesicles and red blood cells. *European biophysics journal*, 17(2):101–111, 1989.
- [136] Igal Szleifer, Diego Kramer, Avinoam Ben-Shaul, William M. Gelbart, and Sam A. Safran. Molecular theory of curvature elasticity in surfactant films. *J. Chem. Phys.*, 92:6800–6817, 1990.
- [137] Charles Tanford. The hydrophobic effect and the organization of living matter. *Science*, 200(4345):1012–1018, 1978.
- [138] R. H. Templer, B. J. Khoo, and J. M. Seddon. Gaussian curvature modulus of an amphiphile monolayer. *Langmuir*, 14(26):7427–7434, 1998.
- [139] ZC Tu and U Seifert. Concise theory of chiral lipid membranes. *Physical Review E*, 76(3):031603, 2007.
- [140] Richard M. Venable, Frank L.H. Brown, and Richard W. Pastor. Mechanical properties of lipid bilayers from molecular dynamics simulation. *Chem. Phys. Lipids*, 192:60–74, 2015.
- [141] Xin Wang and Markus Deserno. Determining the pivotal plane of fluid lipid membranes in simulations. *The Journal of chemical physics*, 143(16):164109, 2015.
- [142] Xin Wang and Markus Deserno. Determining the lipid tilt modulus by simulating membrane buckles. *The Journal of Physical Chemistry B*, 120(26):6061–6073, 2016.

- [143] Max C. Watson, Erik G. Brandt, Paul M. Welch, and Frank L. H. Brown. Determining Biomembrane Bending Rigidities from Simulations of Modest Size. *Phys. Rev. Lett.*, 109(2):028102, 2012.
- [144] Max C Watson and Frank LH Brown. Interpreting membrane scattering experiments at the mesoscale: the contribution of dissipation within the bilayer. *Biophysical journal*, 98(6):L9–L11, 2010.
- [145] Max C Watson, Evgeni S Penev, Paul M Welch, and Frank LH Brown. Thermal fluctuations in shape, thickness, and molecular orientation in lipid bilayers. *The Journal of chemical physics*, 135(24):244701, 2011.
- [146] W Wiese, W Harbich, and W Helfrich. Budding of lipid bilayer vesicles and flat membranes. *Journal of Physics: Condensed Matter*, 4(7):1647, 1992.
- [147] Martin Willensdorfer. Organism size promotes the evolution of specialized cells in multicellular digital organisms. *Journal of evolutionary biology*, 21(1):104–110, 2008.
- [148] Thomas J. Willmore. *An Introduction to Differential Geometry*. Dover, New York, 2012.
- [149] Ou-Yang Zhong-Can, Liu Ji-Xing, and Xie Yu-Zhang. *Geometric methods in the elastic theory of membranes in liquid crystal phases*, volume 2. World Scientific, 1999.